# VECTOR DEFORMATION TIME-SERIES FROM SPACEBORNE MOTION COMPENSATION INSAR PROCESSORS

A DISSERTATION
SUBMITTED TO THE DEPARTMENT OF ELECTRICAL ENGINEERING
AND THE COMMITTEE ON GRADUATE STUDIES
OF STANFORD UNIVERSITY
IN PARTIAL FULFILLMENT OF THE REQUIREMENTS
FOR THE DEGREE OF
DOCTOR OF PHILOSOPHY

Cody Blair Wortham

June 2014

# Abstract

Interferometric synthetic aperture radar (InSAR) is a common remote sensing technique that uses the phase difference between repeat-pass radar images to analyze crustal deformation of the Earth's surface. InSAR provides dense spatial sampling, but is limited by sparse temporal measurements, which represent the projection of three-dimensional deformation onto the sensor's line of sight (LOS). As geophysical events lead to deformation in all directions and at a different of temporal scales, the limitations of InSAR make it difficult to fully characterize and understand the sources of deformation. Time-series approaches are designed to improve the temporal resolution by combining several InSAR measurements to estimate time-dependent deformation, however, since these approaches are derived from InSAR, they are also one-dimensional in the LOS direction. Multidimensional techniques use LOS observations from several different InSAR geometries to resolve vector deformation, but for spaceborne sensors the available geometries are limited, making it difficult to resolve the complete vector deformation field. Multidimensional studies have been extended to use along-track interferometry, which measures an additional orthogonal component. These observations are typically noisier than InSAR, and thus limit where multidimensional techniques can be applied.

We have developed an algorithm, which we call V-SBAS, that extends existing time-series techniques to estimate the temporal evolution of the full three-dimensional vector deformation field. Our approach uses several LOS-InSAR geometries and an along-track technique called multiple aperture interferometry (MAI) to increase the temporal sampling and dimensionality over time-series in a single radar geometry. By combing multiple observations, we reduce the effect of noise, allowing us to estimate

deformation in regions where other multidimensional approaches might typically fail. V-SBAS can be implemented at the backend of any InSAR data processor, but since we use hundreds of interferograms, we develop the processing chain in the context of efficient motion compensation processors. Motion compensation uses the satellite orbit information to shift the position and phase of the receive signal to that of an ideal noninertial circular reference orbit where the focusing equations are simplified and SAR scenes are produced in a common coordinate system. This approach reduces the computational complexity of interferogram formation and is well suited to produce stacks of InSAR data for time-series analysis.

We first present our approach to motion compensation and develop the equations to produce stacks of interferograms in a single radar geometry. We find that processing to a common reference orbit introduces spectral shifts, which can reduce coherence for large motion compensation baselines. We derive expressions for these shifts and propose processor modifications to restore coherence. We also introduce an efficient approach to geolocate products from motion compensation processors. This step is necessary to align the measurements on a common geodetic grid before combining each geometry in the V-SBAS system of equations.

We then develop the V-SBAS algorithm and define a set of constraints that are based on the concept of space-time separability. We present an algorithm to verify the existence of this property through a principal component analysis of existing GPS data, which we use to determine whether or not the constraints should be applied. The separability constraints are nonlinear in the time-series components, thus we also propose a linear approximation to maintain the efficiency of our approach. The linear solution involves an initial unconstrained estimate, followed by a constrained re-estimate of the northward component. We choose this approach because the north is defined primarily by the noisy MAI measurements, while the east and up are defined by InSAR. Finally, we present results of the 2007 Father's Day eruption and intrusion at Kilauea Volcano, Hawaii, where we see agreement with GPS on the order of 2 cm in the east and up directions and 6 cm in the north. The separability constraints reduce the overall average errors to approximately 4 cm, however, some individual stations saw a reduction in error by as much as 10-20 cm.

# Acknowledgements

First and foremost, I would like to thank my advisor Howard Zebker for his guidance, generous support, and patience throughout my tenure at Stanford. Howard has been instrumental in my development as a student and he has taught me many skills that I will carry with me throughout the course of my career. I also thank Paul Segall for his insights into the mechanisms of crustal deformation and for his enlightening suggestions in the area of geophysical inverse theory. I am grateful to the remaining members of my oral defense and thesis reading committee: Sigrid Close, Ivan Linscott, and Tony Fraser-Smith, who were gracious enough to take time out of their busy schedules to offer valuable comments that helped improve this thesis. I would also like to thank Aaron Lanterman, who first introduced me to radar as an undergraduate at the Georgia Institute of Technology.

I have been honored to be part of the Radar Interferometry Group at Stanford, and I am indebted to all of my fellow students for their insights, friendship, and advice throughout the years. In particular, I thank Piyush Shanker Agram who, in many ways, has served as my second advisor. It was during one of our frequent discussions over coffee that the idea behind this thesis was conceived. I thank Noa Bechor for our discussions and her enthusiastic support on the topic of multiple aperture interferometry. I am also thankful to my fellow group members: Lauren Wye, Jaime Lien, Qiuhua Lin, Will Woods, Hrefna Marin Gunnarsdottir, Albert Chen, Tao Chu, Ann Chen, Jessica Reeves, and Leif Harcke, who were always available for discussion and procrastination.

Finally, I dedicate this work to my parents, Bart and Nancy, for their understanding, encouragement, and unconditional support in all my endeavors, with a

special dedication to the memory of my father Bart. I will always remember him as my biggest advocate and principle source of inspiration. I owe thanks to my sister, Samantha, who is obnoxious in the best way possible. And lastly, I am grateful to my partner in crime, Jennifer, who continually challenges me and makes me a better person.

This work was supported by the NASA Earth and Space Science Fellowship. Data were acquired by the Japanese Aerospace and Exploration Agency (JAXA) and made available through the Alaska Satellite Facility's User Remote Sensing Access (URSA) data portal.

# Contents

# List of Tables

# List of Figures

# List of Abbreviations

ALOS ..... Advanced Land Observing Satellite

AZO ..... AZimuth Offsets

DEM ..... Digital Elevation Model

ERS ..... ESA Remote Sensing satellite

ERZ ..... East Rift Zone

FBD ..... Full Bandwidth Dual-polarization

FBS ..... Full Bandwidth Single-polarization

GPS ..... Global Positioning System

IMU ..... Inertial Measurement Unit

InSAR ..... Interferometric Synthetic Aperture Radar

JAXA ..... Japanese Aerospace and Exploration Agency

JPL ..... NASA's Jet Propulsion Laboratory

LFM ..... Linear Frequeny-Modulated

LOS ..... Line of Sight

LOS-SBAS ..... LOS Small BAseline Subset

MAI ..... Multiple-Aperture Interferometry

NASA ..... National Aeronautics and Space Administration

PALSAR ..... Phased Array type L-band Synthetic Aperture Radar

PC ..... Principal Component

PCA ..... Principal Component Analysis

PRF ..... Pulse Repetition Frequency

PS-InSAR ..... Persistent Scatterer InSAR

RCMC ..... Range Cell Migration Correction

RMS ..... Root Mean Square

SAF ..... San Andreas Fault

SAR ..... Synthetic Aperture Radar

SBAS ..... Small BAseline Subset

SLC ..... Single Look Complex image

SNR ..... Signal-to-Noise Ratio

SRTM ..... Shuttle Radar Topography Mission

SVD ..... Singular Value Decomposition

UTM ..... Universal Transverse Mercator

V-SBAS ..... Vector Small BAseline Subset

WGS84 ..... World Geodetic System 1984

# Chapter 1

# Introduction

Surface displacement measurements are an important means of monitoring and understanding the crustal deformation associated with a variety of geophysical phenomenon. These measurements have been widely used to study both natural and mad-made processes, such as earthquakes, magmatic flow in volcanic systems, landslides, glacial flow, and subsidence from ground water extraction. These processes typically cause deformation on the scale of kilometers; therefore, large portions of the Earth's surface must be monitored to accurately characterize the underlying causes of deformation. Interferometric synthetic aperture radar (InSAR) is one approach that is commonly used to measure surface displacements. InSAR measures deformation over large areas (typically 100-km scales) by computing the phase difference between repeat passes of synthetic aperture radar (SAR) acquisitions. This technique is utilized in airborne and spaceborne sensors, with ground resolutions of 1-15 m and displacement accuracies on the order of centimeters.

Compared to other geodetic measurement techniques, such as GPS, the major advantage of InSAR is global coverage with dense spatial sampling. Unlike GPS, which sparsely measures deformation at the locations of ground receivers, InSAR provides a means to observe deformation patterns across wide swaths without the use of ground surveys. Consequently, InSAR gives a better representation of the deformation field and allows researchers to remotely study regions where GPS receivers cannot be installed. On the other hand, InSAR only measures displacements between two points

in time, representing the one-dimensional projection of the east, north, and up (ENU) displacements onto the sensor's line of sight (LOS) vector. Compared to GPS, which gives nearly continuous time positioning, with ENU vector measurements, InSAR is limited in the temporal sampling period and in the dimensionality of the measurements. Ideally, we would like our observations to possess the temporal sampling and vector properties of GPS, but with the spatial density of InSAR.

The current literature attempts to overcome these limitations by extending InSAR to multitemporal and multidimensional analysis. The Small BAseline Subset (SBAS) algorithm is one technique that combines multiple InSAR scenes to estimate the temporal evolution of deformation. This approach improves the temporal sampling of the InSAR deformation fields; however, the SBAS time-series are still one-dimensional in the LOS direction. Multidimensional techniques combine InSAR from several LOS geometries to estimate vector deformation fields. The available geometries are limited for satellites in a polar orbit; therefore, these measurements are typically restricted to two dimensions. Additional work has extended multidimensional InSAR by using along-track interferometry to measure an additional orthogonal component, but these measurements are noisier than InSAR, which limits their application only to areas with large deformation signals.

There are a wide variety of deformation sources, each producing surface displacements in different directions. The observed deformation depends on the type and orientation of the source and varies with the topographic landscape. Furthermore, the deformation signature changes across the scene and evolves in time. In order to unambiguously characterize the source, we need InSAR measurements with the following properties: dense spatial sampling, increased temporal sampling, high signal-to-noise ratio (SNR), and full dimensionality. Approaches combing InSAR and GPS attempt to meet these criteria, but they are limited in comparison to a full vector time-series InSAR solution. Combing multidimensional and multitemporal InSAR is an obvious extension. There are difficulties, however, since the temporal sampling of a single satellite geometry is limited by the 1-2 month repeat pass times of current sensors and since the number of viable along-track interferograms is limited by low SNRs. In order to estimate vector time-series, we need a large number of LOS and

along-track interferograms with high interferometric coherence. Large sets of data will help reduce noise in the time-series estimate, which will allow application to regions with smaller deformation signals.

This thesis bridges the gap between multitemporal and multidimensional InSAR by extending SBAS to a vector formulation. We incorporate multiple LOS geometries and their corresponding along-track measurements. Our technique increases the temporal sampling over that of a single satellite geometry and extends the time-series to three dimensions. We call our algorithm vector-SBAS (V-SBAS) and develop it in the context of a new approach for motion-compensated processing of spaceborne InSAR data. Our processor uses the satellite orbits to propagate echoes from their actual received positions to that of a ideal circular reference track, which greatly reduces the computational complexity of the SAR focusing equations and produces images in a well-known, common geometry. Our discussion of motion compensation is motivated by the need for high quality measurements, efficient processing of large sets of interferograms, and geodetic accuracy. V-SBAS can be applied to data from traditional InSAR processors; however, the motion compensation geometry facilitates efficient formation of interferometric images and increases the reliability of automated processing.

In this work, we develop the equations for SAR focusing in the motion compensation geometry and outline the procedure of interferogram formation. We find that when processing to a common reference orbit, such as in time-series analysis, the motion compensation baseline causes spectral shifts, which reduce interferometric coherence. We derive theoretical expressions for these shifts and introduce processor modifications that restore coherence. Measurements from each InSAR geometry must be combined in a uniform geodetic grid, therefore we also develop a unique approach to geolocation that capitalizes on the simplified motion compensation geometry to resample the InSAR images into the desired map projection. We review the existing SBAS technique and develop the extension to V-SBAS. In our approach, we use multiple LOS geometries from ascending and descending satellite headings and along-track measurements from a relatively new approach called multiple aperture interferometry (MAI). We show that the MAI measurements are noisier than InSAR and that they

limit the accuracy of the northward time-series component. To reduce the effects of MAI noise, we derive a set of constraints that enforce a constant direction of deformation. These constraints represent a new way to condition the SBAS equations, which is only applicable to vector time-series. We show that these constraints are appropriate if the time-series exhibits space-time separability and we outline a procedure to test for this condition through a principal component analysis (PCA) of existing GPS data. The constrained equations are nonlinear, thus we propose a linear approximation that constrains only the noisy, northward time-series component. Finally, we present results for the 2007 Father's Day eruption and intrusion at Kilauea Volcano, Hawaii, where we see that the constrained time-series estimates have overall average errors on the order of 2 cm in the up and east directions and 4 cm in the north. Our results verify that V-SBAS can effectively increase the temporal sampling and dimensionality of SBAS, while reducing the effects of individually noisy along-track interferograms.

## 1.1 Contributions

The contributions of this thesis are divided into two main areas: motion compensation processing of spaceborne InSAR data and vector deformation time-series. Our discussion of motion compensation develops the equations for processing spaceborne data to an ideal circular reference orbit and highlights processor modifications needed to maintain interferometric coherence. For vector deformation time-series, we introduce a new approach to combine several, one-dimensional radar observations to estimate three-dimensional vector time-series and develop constraints on the direction of deformation that reduce the effects of phase errors. The principle contributions of this work are summarized below:

- Development of a geodetically accurate motion compensation radar processor that improves computational efficiency over traditional range-Doppler processors and produces interferograms in a common, well-known coordinate system.

- Identification of processor-induced spectral shifts that reduce coherence for large

motion compensation baselines and formulation of processor modifications to preserve coherence at arbitrary imaging geometries.

- Development of a new approach to geolocation that utilizes the simplified spherical geometry of our motion compensation processor to efficiently and accurately resample radar images to an orthonormal map projection.

- Extension of existing one-dimensional time-series techniques to incorporate measurements from multiple radar geometries to estimate three-dimensional vector deformation time-series.

- Formulation of the concept of space-time separability to constrain the relative motion of orthogonal components in vector time-series. Our approach outlines a new method to verify separability through a PCA of GPS data and presents an efficient linear approach to approximately enforce these constraints.

- Application of our vector time-series algorithm to the 2007 Father's Day eruption and intrusion at the Kilauea Volcano, Hawaii, where results show errors on the order of 2-4 cm.

## 1.2 Thesis Roadmap

We begin in Chapter 2 with a brief overview of InSAR and describe the limitations of the traditional approach. We discuss the extension to multitemporal and multidimensional analysis and review existing techniques in the literature. This discussion includes an introduction to MAI and gives an overview of MAI and InSAR processing.

In Chapter 3, we derive the mathematical framework for a spacecraft in a circular orbit and describe how the processing equations are simplified in this ideal geometry. We describe the process of motion compensation and show that we can correct the position and phase of the received echoes to mimic those of echoes in the ideal circular orbit. Following motion compensation, we can use the simplified focusing equations, which reduce the computational complexity of the processor and facilitate efficient

focusing, coregistration, topographic phase removal, and formation of InSAR stacks for time-series analysis.

In Chapter 4, we show that the motion compensation phase correction introduces shifts in the range and azimuth spectra that reduce coherence for large motion compensation baselines. We develop theoretical expressions for the shifts, which are functions of the actual and reference geometries, and we describe processor modifications that account for the range and azimuth carriers. We apply our approach to interferograms at the Kilauea Volcano in Hawaii and show that coherence is almost entirely restored for large motion compensation baselines.

In Chapter 5, we develop a new approach to geolocation that takes advantage of the simplified geometry in the motion compensated orbit for efficient resampling from radar coordinates to a geodetic grid. We present a closed-form algorithm for spaceborne sensors, where the Doppler centroid is assumed to be constant across the swath and an iterative approach that is suitable for airborne sensors with significant Doppler centroid range dependence. We verify our algorithm by comparison with an array of corner reflectors and also by registration with a digital elevation model (DEM).

In Chapter 6, we review the SBAS equations for a single radar geometry and develop the extension to the vector time-series. We describe how multiple radar geometries can be combined to estimate three-dimensional displacement fields, and we discuss the limitations of our technique. We introduce space-time separability and show how this property can be used to constrain the direct of deformation, thereby reducing the effects of phase noise and processing artifacts. In Chapter 7, we process interferograms at the Kilauea Volcano, Hawaii, according to Chapters 3-5, and apply our vector time-series algorithm. Results are given for observations during the 2007 Father's Day eruption and intrusion and errors are computed relative to GPS.

Finally, in Chapter 8 we provide a summary and suggestions for future work.

# Chapter 2

# InSAR Background

The use of InSAR time-series is a relatively new approach to resolve the temporal evolution of deformation at the Earth's surface (Ferretti et al., 2001; Berardino et al., 2002). As this area of research develops, authors have proposed several variants of multitemporal analysis, all of which, rely on basic SAR and InSAR processing (Casu et al., 2011; Hetland et al., 2012). In this chapter, we give a broad overview of these areas, we discuss the extension to multidimensional and multitemporal analysis, and we highlight the limitations of these techniques.

## 2.1 History

Radar interferometry found its first uses in the 1970s with earth-based interferometers used to measure lunar topography (Zisk, 1972; Bills & Ferrari, 1977). In the 1980s, researchers adapted these interferometric techniques to airborne SAR, which quickly become a valuable remote sensing technique for a variety of geophysical applications. Early InSAR examples include Zebker and Goldstein (1986), who used aircraft equipped with multiple antennae for terrestrial topographic mapping and Goldstein et al. (1989) who extended these techniques to measure surface ocean currents.

New advances accompanied the launch of the European Space Agency's ERS-1 satellite in 1991, where satellite repeat pass interferometry allowed for sustained coverage on a global scale. The first applications of ERS-1 were in the measurement of

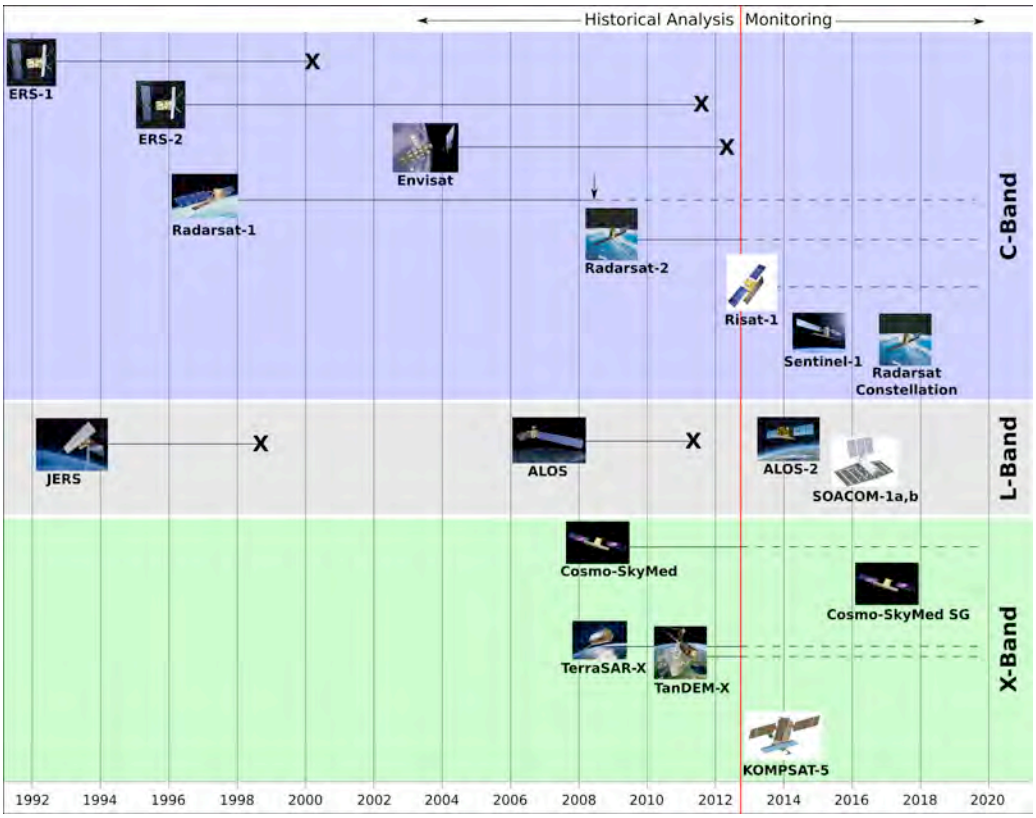


Figure 2.1: Modern and historical SAR satellites (courtesy of Lin Liu, Stanford University).

surface deformation due to the 1992 earthquake in Landers, California (Massonnet et al., 1993; Zebker et al., 1994), with subsequent studies including volcanic deformation (Massonnet et al., 1995), ice motion (Joughin et al., 1995), and hydrologic modeling (Galloway et al., 1998).

The success of ERS-1 spawned the launch of several other InSAR-capable satellites from both national space agencies and commercial organizations. Figure 2.1 summarizes the past, current, and future satellite missions providing publicly available remote sensing data. Since 1991, the coverage of satellites, spanning a range of resolutions, wavelengths, and polarizations, has given scientists the ability to study the Earth and its deformation in new ways. Some example applications include

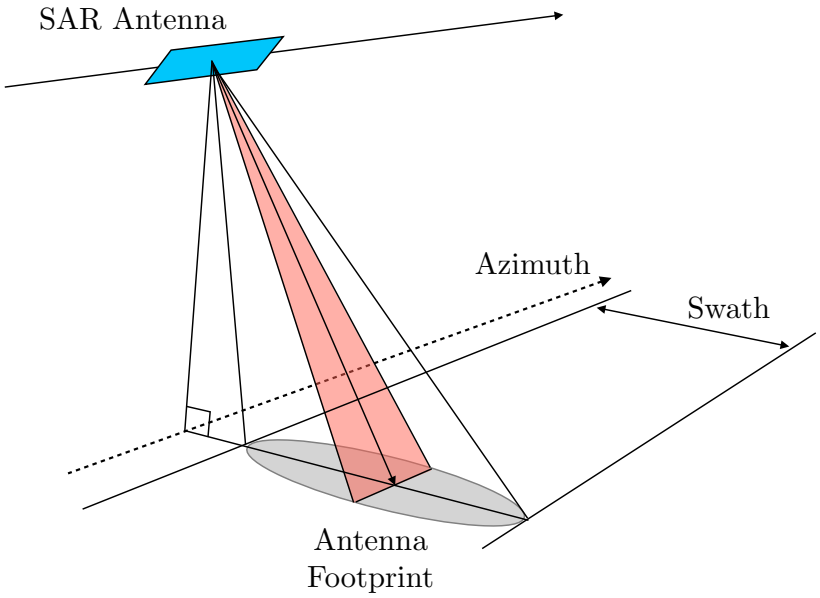


Figure 2.2: Flat Earth SAR imaging geometry.

rapid repeat satellite interferometry (Rufino et al., 1998; Krieger et al., 2007), high-resolution imaging (Schwerdt et al., 2005), and radar polarimetry (McNairn et al., 2009). As these only touch on the capabilities of modern SAR satellite constellations, we refer the reader to the literature reviewing recent advances for a more comprehensive overview (Bürgmann et al., 2000; Pottier & Ferro-Famil, 2008; Rott, 2009; Prati et al., 2010; Eineder et al., 2013).

## 2.2 Synthetic Aperture Radar

SAR is an advanced form of radar that exploits the motion of the sensor platform for high-resolution microwave imaging. Figure 2.2 shows a simplified example of the geometry for a typical side-looking SAR system. The antenna is mounted on an aircraft or satellite, which travels in the azimuth direction and views targets at a range, which we define as the distance between the phase center of the antenna and a target. The combination of range and azimuth characterize the native coordinates of SAR imagery and denote points in the slant-plane.

The main lobe of the radar antenna illuminates some finite area on the ground, and within this region, cross-track component defines the swath (Figure 2.2). The Fraunhofer far-field approximation defines the angular beam pattern as the Fourier Transform of the physical aperture, thus the shape of the antenna determines the swath and the azimuthal widths of the antenna footprint. For SAR imaging, the antenna is usually rectangular and a two-dimensional sinc function approximates the transmit beam pattern, which is inversely proportional to the aperture size (Bracewell, 2003).

For a real aperture system, the beamwidth of the antenna determines the azimuth resolution. Figure 2.3a shows an example, where individual targets can only be resolved if their along-track separation is greater than the width of the beam. If the beam is too wide, then the reflected energy from multiple targets appears at the same azimuth position, and we images the targets as a single point. Given the Fourier transform relationship between aperture size and beamwidth, a real aperture system must have a longer physical aperture to increase the azimuth resolution.

SAR processing alleviates the antenna length constraint by using a matched filter to compress echoes in the azimuth dimension. Figure 2.3b shows a SAR system with a short antenna and very wide beam. On each pulse, multiple targets are illuminated, but since they appear in different portions of the beam, their ranges, and consequently their Doppler phase shifts, vary. As the sensor travels in azimuth, the range variations define a quadratic phase for each target, therefore the overall signal is a superposition of unique, linear frequency-modulated (LFM) chirps. Using matched filtering (Skolnik, 1990), we suppress the sidelobes from each target, and the effective resolution of the system is increased (Figure 2.3c).

A SAR processor focuses raw data by applying range and azimuth matched filtering to compress the complex two-dimensional echoes into a single resolution element. Chapter 3 gives a detailed overview of one implementation (Zebker et al., 2010), but in general, there are numerous approaches to processing SAR data (Curlander & McDonough, 1991; Soumekh, 1999; Cumming & Wong, 2004). These algorithms all reduce the smearing caused by the large beamwidth, but each approach varies in the dimensionality of the matched filters and in the domain that filtering is implemented.

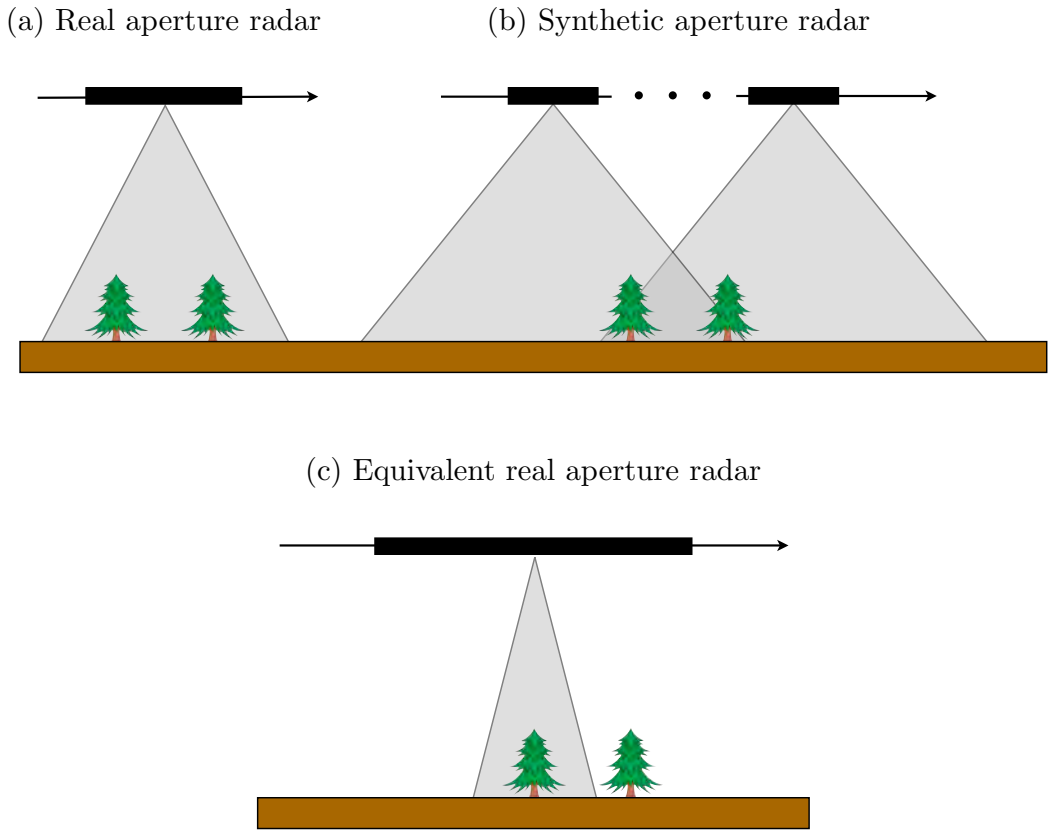


Figure 2.3: (a) Real aperture antenna, (b) synthetic aperture antenna, and (c) a real aperture with equivalent beam pattern to the full synthetic aperture.

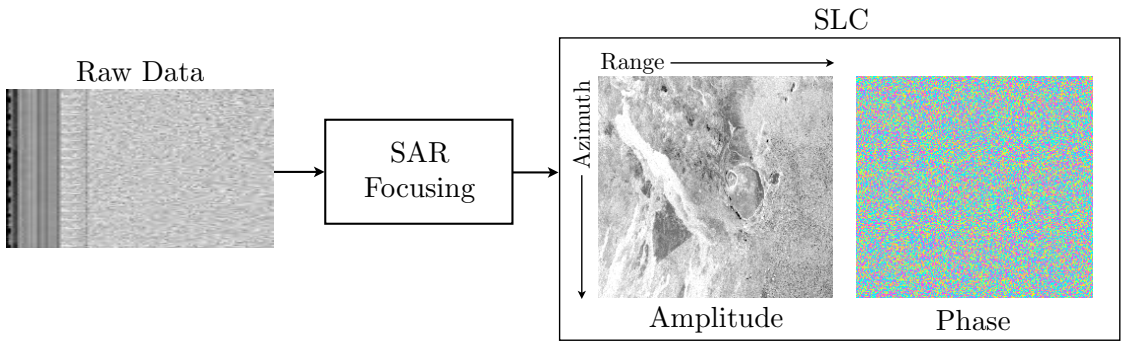


Figure 2.4: Simplified SAR processing chain. Raw data are received as I and Q samples. After focusing, the SLC is a two-dimensional complex image, with amplitude representing the ground reflectivity and random phase between each pixel.

Figure 2.4 shows a simplified diagram of the SAR processing chain, where we refer to the output as a single look complex image (SLC), with pixels denoting complex reflectivities in the slant-plane. Due to the geometric and physical properties of electromagnetic scattering, the amplitude of an SLC resembles a photograph, although, the underlying mechanism behind SAR image formation is fundamentally different than optical imagery.

## 2.3 SAR Interferometry

The SAR phase in Figure 2.4 contains components from surface scattering and path delay. The scattering component is random between pixels, but the path delay is a deterministic function of the radar geometry. The basis of InSAR is that by taking the phase difference of two SAR scenes, the scattering components cancel and the resulting phase is proportional to the difference in range. Each SLC is acquired in a slightly different geometry, therefore, in order to ensure that the scattering phases cancel and that the correct pixels are interfered, the second SLC must be resampled to the coordinates of the first. This process is known as coregistration, and if the images are not registered with sub-pixel accuracy then the inteferometric signal will contain unwanted phase noise (Lu et al., 2005; Sansosti et al., 2006). Following coregistration, the phase difference is computed by a pixel-by-pixel conjugate multiplication between

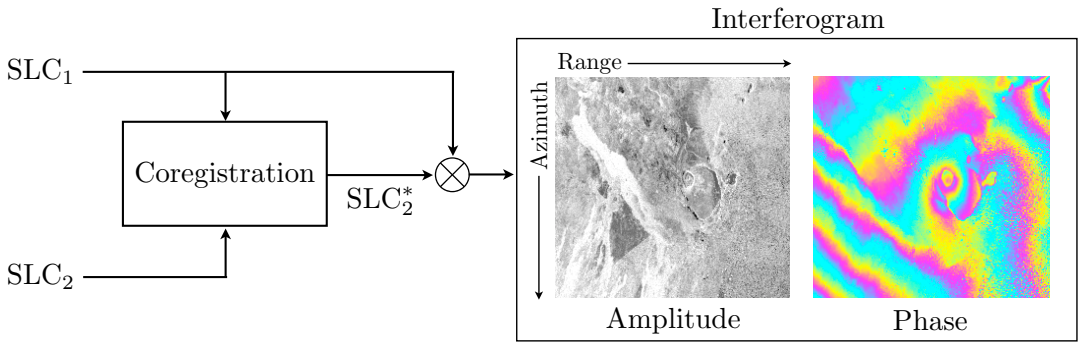


Figure 2.5: Simplified InSAR processing chain. SLC$_2$ is coregistered to SLC$_1$ and then the two complex images are conjugate multiplied to form an interferogram.

the first and second SLC. An example InSAR processing chain is shown in Figure 2.5, where the resulting complex image is an interferogram that represents the scattering power and the phase delay due to range differences.

Figure 2.6 illustrates the InSAR geometry for either a repeat pass or two antenna configuration. At a wavelength $\lambda$, we write the interferometric phase as

$$\phi = -\frac{4\pi}{\lambda}(\rho_1 - \rho_2) = -\frac{4\pi}{\lambda}\Delta\rho\,, \tag{2.1}$$

where $\rho$ is the range and $\Delta\rho$ is the range difference. There are several causes for path delay and it is useful to decompose the phase into its respective components

$$\phi = \phi_{\text{earth}} + \phi_{\text{topo}} + \phi_{\text{defo}} + \phi_{\text{atm}} + \phi_{\text{noise}}\,. \tag{2.2}$$

The geometric terms, $\phi_{\text{earth}}$ and $\phi_{\text{topo}}$, represent a parallax effect from imaging the ellipsoidal Earth and its topography with a spatial baseline $B$. The deformation term $\phi_{\text{defo}}$, represents phase due to surface change occurring between the two acquisitions. $\phi_{\text{atm}}$ is a phase screen resulting from varying atmospheric delays and $\phi_{\text{noise}}$ is a noise term that includes system noise, decorrelation, or processing artifacts. Depending on the application, any of these terms may be considered noise. For example, topographic studies are only concerned with $\phi_{\text{topo}}$. On the other hand, deformation studies focus on $\phi_{\text{defo}}$ and make efforts to remove the topographic and atmospheric phases.

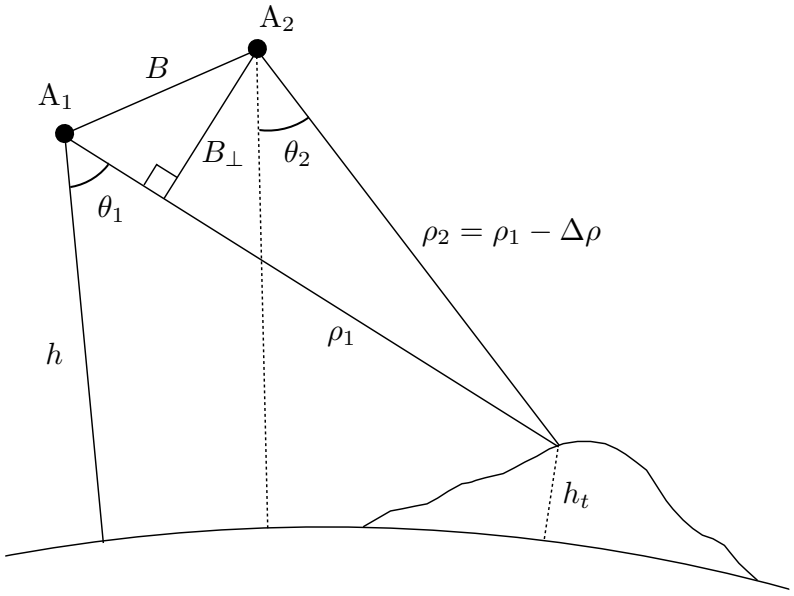


Figure 2.6: InSAR imaging geometry for two sensors located at positions $A_1$ and $A_2$.

Figure 2.7a shows an example interferogram covering an eruption and intrusion at the East Rift Zone (ERZ) of Kilauea Volcano, Hawaii (Chapter 7). This interferogram contains phase contributions from topography, atmosphere, deformation, and noise. We produced this interferogram using a motion compensation InSAR processor (Zebker et al., 2010) and as a result, the image does not contain the $\phi_{\text{earth}}$ term. Automatic removal of the curved-Earth phase is one of the benefits of motion compensation processing, which we discuss further in Chapter 3.

The topographic phase is a function of the radar geometry and includes terms for the look angle $\theta$, perpendicular baseline $B_\perp$, and terrain height $h_t$ (Figure 2.6). Zebker and Goldstein (1986) give the theoretical expression as

$$\phi_{\text{topo}} = -\frac{4\pi}{\lambda}\frac{B_\perp}{\rho_1 \sin\theta_1} h_t \,, \tag{2.3}$$

relating the geometry to the measured phase. Since $\phi_{\text{topo}}$ is proportional to elevation, the interferogram in Figure 2.7a shows contours or fringes representing changes in topographic height. The phase is cyclical in the complex domain, therefore the colors

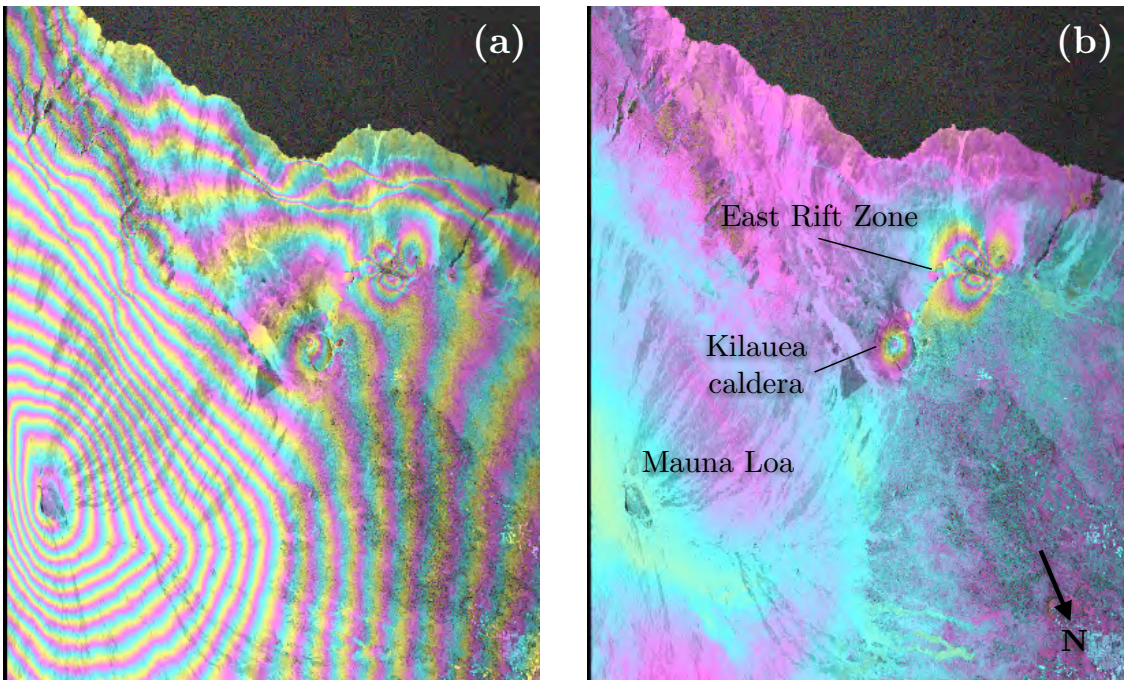


Figure 2.7: ALOS PALSAR interferograms over the island of Hawaii (a) containing topography and deformation phases and (b) flattened with topographic phase removed. Phases are displayed modulo $2\pi$, with a single cycle corresponding to approximately 11.5 cm for the L-Band radar.

repeat every $2\pi$ radians. Using Equation 2.1, a single cycle corresponds to $\lambda/2$ meters of elevation, and in the absence of deformation, we can use Equation 2.3 to create a digital elevation model (DEM), such as those produced during NASA's Shuttle Radar Topography Mission (SRTM) (Farr et al., 2007).

The interferogram in Figure 2.7a contains phase contributions from both topography and deformation. In order to observe the deformation phase, we remove $\phi_{\text{topo}}$ using precise orbit information, existing DEMs, and Equation 2.3. The resulting flattened interferogram is shown in Figure 2.7b, where fringes are revealed at the Kilauea caldera and along the ERZ. Since the resulting deformation has magnitude greater than $\lambda/2$, we see repeated fringes corresponding to multiple cycles of displacement.

Finally, for use in most geophysical applications, it is necessary to measure a continuous deformation map, so we must integrate the phases between neighboring pixels

(Costantini, 1998; Chen & Zebker, 2002). We call this process phase unwrapping and for most applications it is required before further analysis. In addition, since the InSAR observations are in slant-plane coordinates, we must also rectify or geolocate the measurements onto a uniform geodetic grid, such as UTM or WGS-84. Geolocation is an important step to relate the slant-range measurements to ground coordinates, which we discuss more in Chapter 5.

## 2.4 InSAR Coherence

The SLCs must be interfered coherently to produce viable interferometric phases, which depend on precise alignment and similarity of the underlying scattering mechanisms. Zebker and Villasenor (1992) define one measure of coherence or correlation as

$$\zeta = \frac{|\langle a_1 a_2^* \rangle|}{\sqrt{\langle a_1 a_1^* \rangle \langle a_2 a_2^* \rangle}} \approx \frac{\left| \sum_{k=1}^{n} a_{1,k} a_{2,k}^* \right|}{\sqrt{\sum_{k=1}^{n} \left( a_{1,k} a_{1,k}^* \right) \sum_{k=1}^{n} \left( a_{2,k} a_{2,k}^* \right)}}, \tag{2.4}$$

where $a_1$ and $a_2$ are the SLCs, $^*$ denotes the complex conjugate, and $\langle \cdot \rangle$ is the ensemble average. Assuming the statistics are stationary, we approximate the ensemble average by a spatial average of $n$ points surrounding the pixel of interest, with subscripts denoting the $k^{th}$ pixel in the surrounding neighborhood. For convenience, we normalize coherence such that $\zeta \in [0, 1]$, with $\zeta = 1$ representing perfect correlation.

There are several factors that affect interferometric coherence and put limits on the reliability of the measurements. Change in surface scattering with time is known as temporal decorrelation. This arises when surface conditions such as vegetation, soil moisture, or snow fall change from one observation to the next. If the surface is changing and the temporal separation is too great, then coherence can be completely lost.

Spatial decorrelation is another source of degradation. This occurs when the viewing geometry varies significantly between observations. When the incidence angle changes, the scatterers have different properties, and coherence is lost. We can

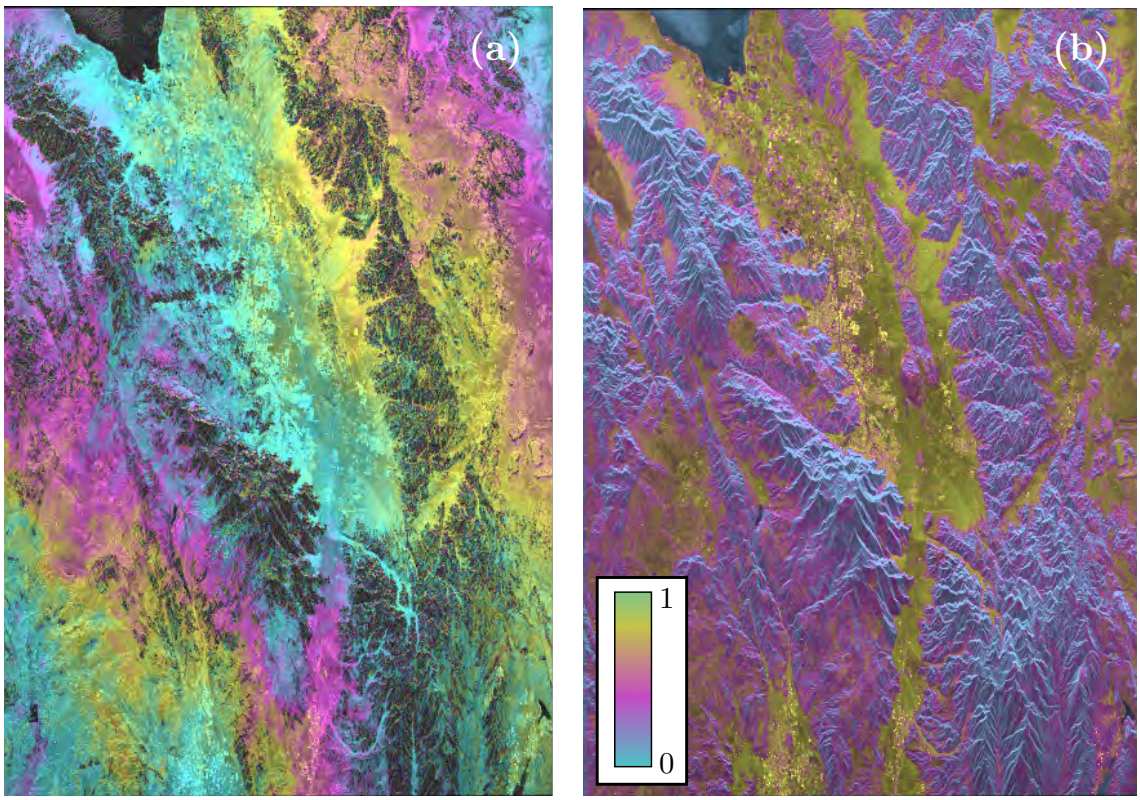


Figure 2.8: (a) ERS-1/2 interferogram of the Piñon Flat area in southern California. (b) Coherence map. Phases are displayed modulo $2\pi$, with a single cycle corresponding to approximately 2.8 cm for the C-Band radar.

also view this phenomena in the Fourier domain, where a change in incidence angle results in different bands of the ground reflectivity spectrum being measured (Gatelli et al., 1994). As the spatial baseline or topographic slope increases, less of the range reflectivity spectra overlap, and coherence is degraded. Efforts have been made to reduce these effects with common band filtering (Gatelli et al., 1994; Prati & Rocca, 1993), but there is a limit, known as the critical baseline, that defines a maximal separation between sensors for coherent imaging. Although common band filtering does reduce phase noise, the critical baseline determines a limitation of InSAR geometries. We discuss common band filtering and the range spectral shifts further in Chapter 4 for both traditional and motion compensation InSAR processors.

An example of coherence is shown in Figure 2.8 at the Piñon flat area in southern

California. The interferogram (Figure 2.8a) has a baseline of $B_\perp = 320$ m and a temporal separation of 1 day. This baseline is well below the critical value for a C-Band radar with no topography and we can assume the temporal separation is negligible. Coherence is high in the flat regions (Figure 2.8b), but low in the mountainous terrain. Even with small spatial and temporal baselines, high topographic slopes change the incidence angle and reduce correlation. A reduction in $B_\perp$ would minimize these effects, which serves as a motivation for baseline thresholds in selecting interferometric pairs.

## 2.5 Multidimensional InSAR

The range measurements of InSAR are inherently one-dimensional, recording the slant-range change in the direction from the target to the sensor (Figure 2.2 and Figure 2.6). This line of sight (LOS) measurement is enough to resolve topographic height, but in the case of deformation, InSAR measures the projection of the full three-dimensional ground displacement onto the LOS vector. A limitation of both spaceborne and airborne sensors, traditional InSAR only reveals one component of deformation. The following sections further outline this limitation and introduce current approaches to estimating three-dimensional displacements using satellite-based InSAR.

### 2.5.1 The Missing Component of Satellite InSAR

Current remote sensing satellites operate in a nearly-polar orbit. This is true of all historical and planned future missions (Figure 2.1), where the rotation of the Earth allows the satellite to image the entire planet without wasting additional resources to steer the sensor. We show the imaging geometry of a polar orbit in Figure 2.9. This configuration gives two observations of a single target: one when the satellite travels from the South pole to the North pole (ascending orbit), and a second when traveling from the north to the south (descending orbit). In both cases, the heading is primarily in the north or south, with the LOS oriented in a plane perpendicular

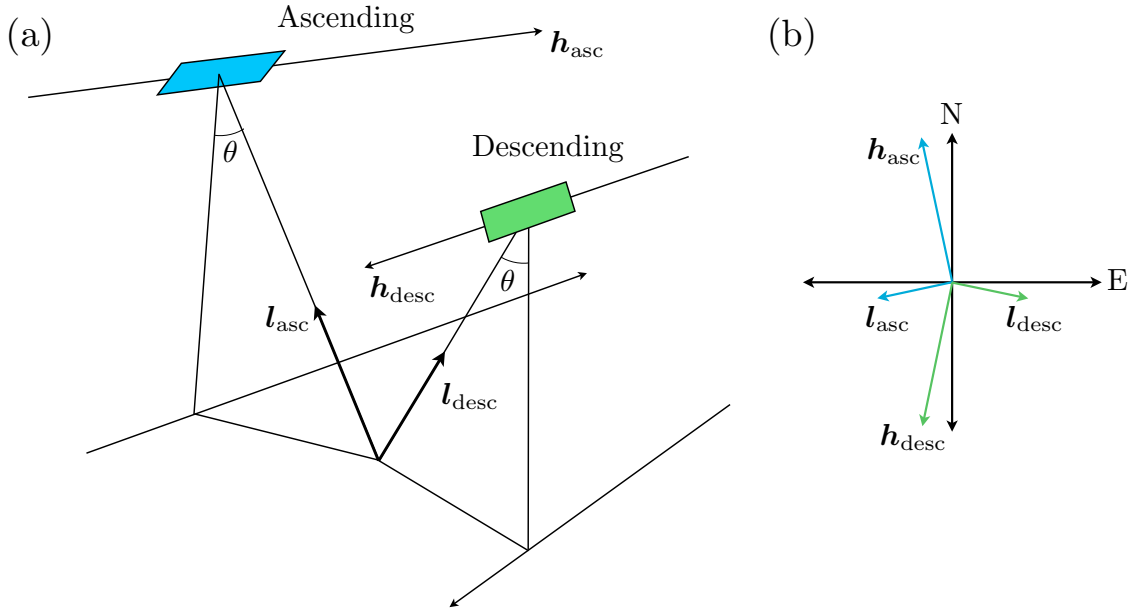


Figure 2.9: (a) Geometry for ascending and descending polar satellite orbits. (b) Projection of heading and LOS vectors onto the ground plane. LOS is denoted by $\boldsymbol{l}$ and heading by $\boldsymbol{h}$, where the subscripts indicate orbit direction.

to the along-track direction. Since the projection of the north dimension onto the LOS is essentially zero (Figure 2.9b), the primary components of the ascending and descending looks vectors are east and up. As a result, the polar orbit geometry is highly insensitive to deformation in the north direction, which defines a missing component that cannot be observed with traditional satellite-base InSAR.

The obvious consequence of this limitation is the inability of InSAR to observe events with deformation oriented entirely in the northward direction. Even when the displacement is not completely orthogonal to the LOS, the insensitivity of the InSAR geometry can make it difficult to measure small deformation signals without substantial north components. An example is given in Figure 2.10 at the Parkfield section of the San Andreas Fault (SAF), where the deformation is largely perpendicular to the ascending and descending LOS vectors. In this section of the SAF, creep rates are small, on the order of 30 mm/yr (Murray et al., 2001), and the projection of these displacements onto the LOS will give observations of less than a few mm/yr.

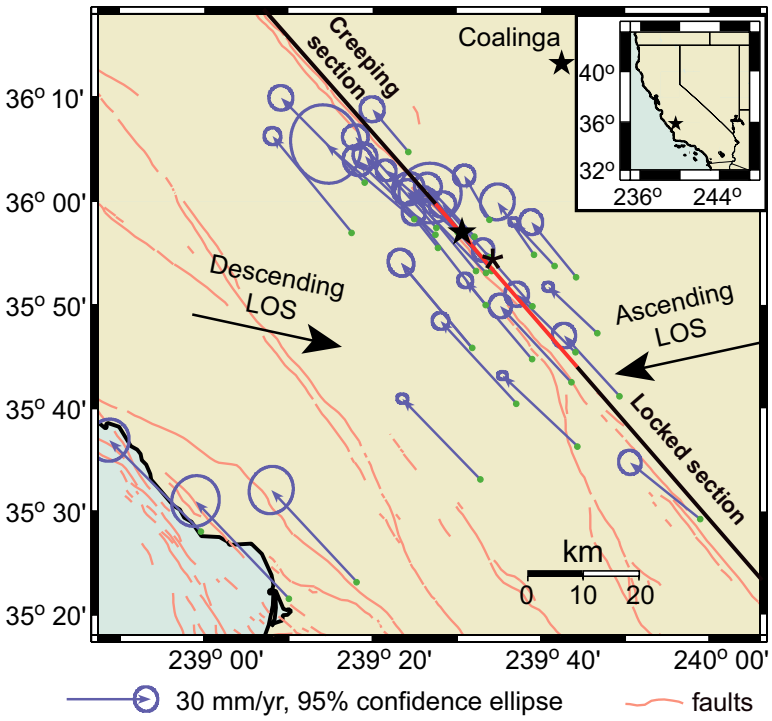


Figure 2.10: Interseismic GPS velocities at the Parkfield section of the San Andreas Fault with InSAR LOS vectors for ascending and descending headings (Bechor, 2006).

Considering the high decorrelation rates at Parkfield, if the temporal baseline is large, then measured signal can easily fall below the noise level of the interferometric phase.

### 2.5.2 Along-Track InSAR

For polar orbits, the along-track direction is highly perpendicular to northward deformation and measurements along this direction will reveal the missing component. Azimuth offsets (AZO) is a common approach, where the along-track component is measured by cross-correlating SLC amplitudes (Peltzer et al., 2001; Sandwell et al., 2002; Fialko, 2004; Fielding et al., 2005). This approach is best suited for large deformation, as the accuracy is typically 15 cm, on the order of 1/20th-1/30th of a pixel (Casu et al., 2011). Bechor (2006) gives an example in Figure 2.11a for the 1999

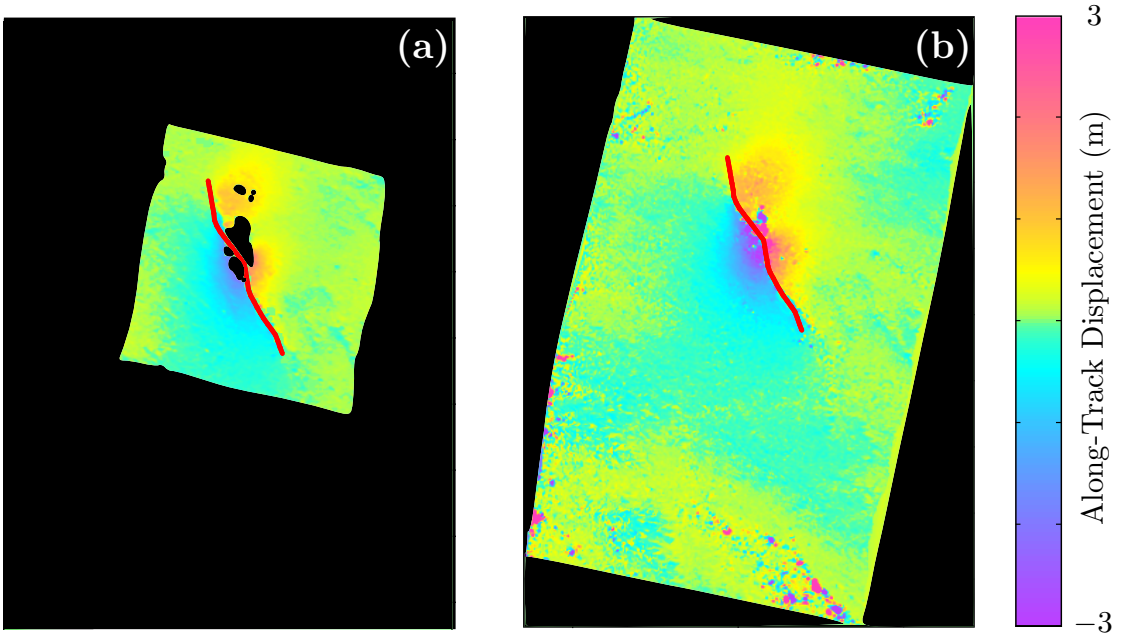


Figure 2.11: Geocoded ERS interferograms of the 1999 Hector Mine earthquake using (a) AZO and (b) MAI processing techniques (Bechor, 2006). Along-track displacements are given in meters and the fault trace is represented by the red line.

Hector Mine earthquake. The large magnitude of deformation and north-south orientation make this event a good candidate for AZO analysis. AZO has been widely used, but the drawbacks are the computational complexity involved with repeated cross-correlations and the limited accuracy for detecting small deformation signals.

A newer approach for measuring along-track deformation, multiple-aperture interferometry (MAI), achieves higher precision, with significantly lower computational cost (Bechor & Zebker, 2006; Jung et al., 2009, 2013). MAI uses aperture splitting to generate forward- and backward-looking interferograms, whose phase difference is proportional to the along-track deformation. Aperture splitting is a novel method for sensing deformation in the northward direction, however, the reduced beamwidth results in less integration time and a lower signal-to-noise ratio (SNR). This SNR decreases causes MAI to have more phase noise than LOS-InSAR, but for high coherence pixels, the accuracy is superior to that of AZO. Typical MAI errors are on the order of 8-10 cm (Bechor & Zebker, 2006).

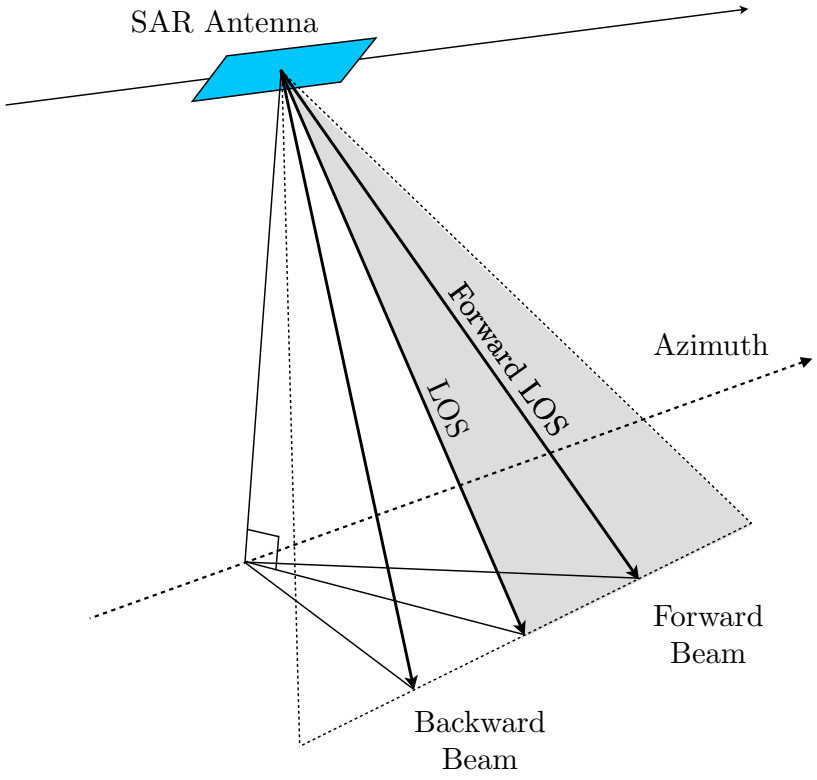


Figure 2.12: Geometry of forward- and backward-looking MAI beams. The aperture is split to make observations along the forward and backward LOS vectors.

Figure 2.12 shows the geometry for MAI and Figure 2.13 gives a block diagram for processing. We split the aperture by bandpass filtering in the Doppler domain, producing forward and backward SLCs. We interfere the corresponding split-aperture images between repeat passes and produce interferograms that are proportional to deformation along the forward and backward LOS. The vector difference of these look directions cancels the cross-track component, thus the along-track deformation can be measured by computing the phase difference between forward and backward interferograms. Letting $\phi_{\text{foward}}$ and $\phi_{\text{backward}}$ represent the forward and backward LOS phases, Bechor and Zebker (2006) define the MAI phase as

$$\phi_{\text{MAI}} = \phi_{\text{foward}} - \phi_{\text{backward}} = -\frac{4\pi}{l} n \, \Delta x \, , \tag{2.5}$$

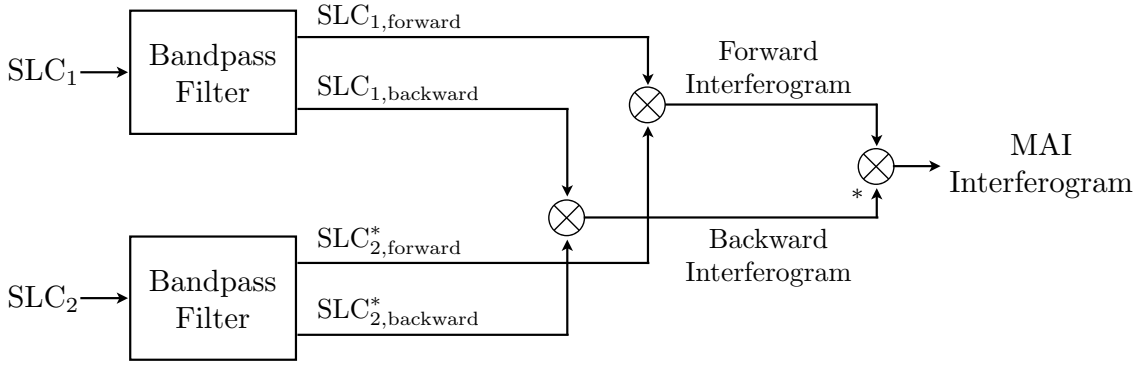


Figure 2.13: Simplified MAI processing chain.

where $n \in (0, 1)$ is the fractional beamwidth, $l$ is the physically aperture length, and $\Delta x$ is the along-track deformation. For the example in Figure 2.11b, MAI retains greater coherence in the region adjacent to the fault and has overall lower phase noise than AZO. In addition, the cost of computing MAI interferograms is minimal, since the bandpass filters are applied after SAR focusing. We discuss details of the MAI phase statistics and give exact expressions for the geometrical relationships to LOS-InSAR in Chapter 6.

### 2.5.3 Multidimensional InSAR

Initial studies in multidimensional InSAR combined interferograms from ascending and descending headings (Figure 2.9) to overcome the inherint LOS limitation (Fujiwara et al., 2000; Ng et al., 2011, 2012). This technique is successful in resolving a two-dimensional deformation field, but since each observation is from a polar orbit, the along-track component is still undefined. Although limited, the use of two-dimensional analysis is important in constraining deformation source models. Specifically, without geometric diversity of the measurements, there may be ambiguities in the parameters estimated from geophysical inversions (Wright et al., 2004; Sudhaus & Jónsson, 2009). Ideally, however, we want measurements spanning the entire three-dimensional space. This configuration is better suited to characterize

general source orientations and multi-source scenarios (Bürgmann et al., 2006; Sudhaus & Jónsson, 2009). A common solution is combining InSAR with other geodetic measurements. For example, GPS can constrain the model in the north direction, although this data lacks the spatial density of InSAR.

With the introduction of along-track methods, several studies have combined these techniques with ascending and descending InSAR. The along-track measurements constrain deformation in the north, while InSAR defines the east and upward directions. In this approach, the measurements from separate look directions can be combined to estimate three-dimensional deformation (Wright et al., 2004) or used directly as the input to a source model inversion (Barbot et al., 2008). There are several examples of both AZO (Sandwell et al., 2008; Fialko et al., 2005, 2001) and MAI (Jung et al., 2011; Sun et al., 2004; Erten et al., 2010; Gourmelen et al., 2011; Jónsson, 2012; Hu et al., 2012) being used in conjunction with InSAR to successfully estimate the full three-dimensional deformation field. However, due to the increased measurement uncertainties, these studies tend to focus on areas with larger co-seismic deformation. That being said, despite the restriction of along-track accuracy, these approaches have full dimensionality and retain the spatial density of InSAR.

## 2.6 Multitemporal InSAR

Multitemporal techniques are an extension of InSAR that use large sets of SAR scenes to investigate the temporal evolution of deformation and mitigate errors found in single interferograms. At the most basic level, joint processing increases the temporal sampling and reduces noise due to atmospheric phase screens, decorrelation, and other error sources. Stacking or averaging of interferograms is the most simple form of multitemporal processing (Sandwell & Price, 1998). This approach assumes that the deformation is linear, and uses the stack average to estimate a constant deformation rate. If the errors are uncorrelated between interferograms, they tend to cancel, giving an estimate of average LOS phase velocity.

Persistent Scatter InSAR (PS-InSAR) is another more advanced approach that does not assume a constant velocity, but relies on the dominant scatters in a resolution

element to estimate a LOS time-series directly from a set of interferometric phases (Ferretti et al., 2001). PS-InSAR uses a statistical approach to identify pixels with a single dominant scatterer that are less affected by decorrelation. This technique is best applied to urban areas where manmade structures, such as buildings, act as phase-stable corner reflectors. The primary advantage of PS-InSAR is that the analysis is performed at the full SLC resolution, giving it the ability to form time-series in regions that are only sparsely coherent.

In the common event that all the scatters within a resolution element are of nearly equal strength, it is more appropriate to exploit redundancy in the measurements to reduce phase errors. The Small BAseline Subset (SBAS) algorithm (Berardino et al., 2002) is one technique based on this concept. Unlike PS-InSAR, SBAS assumes longer spatial wavelengths and uses averaging to reduce phase errors by forming the time-series at the multi-looked resolution of the interferogram. In addition, SBAS time-series are not derived directly from the interferometric phases, but as the solution to system of equations involving the differential phases from all possible interferometric pairs that meet a predetermined threshold on spatial and temporal baselines. This approach reduces noise from decorrelation and provides temporal filtering, which is inherent in the minimum norm least-squares solution. A detailed overview of SBAS processing and the associated equations are covered in Chapter 6.

## 2.7 Summary

InSAR is a valuable technique for measuring deformation of the Earth's surface, however, there are limitations that dictate how and where it can be used effectively. Reduction of coherence loss from spatial and temporal baselines is one the goals of new-satellite and instrument designs, where efforts are being made to reduce the repeat pass times and variability of the satellite orbits. On the other hand, LOS sensing and temporal resolutions are inherent limitations of spaceborne InSAR, which have been partially addressed by novel processing schemes, although more work is needed to fully exploit the capabilities of InSAR.

# Chapter 3

# Motion Compensation Processing

## 3.1 Introduction

The utility of SAR and InSAR measurements depend on precise processing of the raw satellite data to form well focused images with accurate phase. The theory of InSAR and radar signal processing is well understood (Curlander & McDonough, 1991; Soumekh, 1999; Hanssen, 2001; Cumming & Wong, 2004), but there is often a disconnect between theory and the actual implementation of these equations. This disconnect stems from the limited accuracy of satellite orbit tracking in historical sensors, which leads to heuristic approaches for focusing and aligning data in undefined geometries. Traditional InSAR processors assume that the orbit information is imprecise and depend on methods such as autofocus and low-resolution cross correlation to refine processing parameters and to align images in a common coordinate system (Kampes & Usai, 1999; Werner et al., 2000; Rosen et al., 2004). These solutions are computationally inefficient, and in many instances, fail to produce high quality and geodetically accurate imagery.

Recent developments in satellite tracking now allow for highly accurate orbit information, with errors on the order of tens of centimeters or less (Tapley et al., 1994; Scharroo & Visser, 1998; Yamamoto, 2008). Given this level of precision, modern SAR and InSAR processors can rely on the satellite state vectors to define the radar

geometry and to facilitate direct implementation of the theoretical processing equations. As a result, newer InSAR processors avoid autofocus modules and use the orbits directly for geometry-based routines, such as baseline estimation and identification of Doppler ambiguities (Sandwell et al., 2011). The advances in orbit tracking enable faster and more accurate processing, however, due to the nature of ellipsoidal Earth models, complicated equations are often approximated or solved iteratively using brute force methods (Kampes & Usai, 1999).

In this chapter, we describe our approach to processing satellite imagery, which exploits the precision of modern orbit tracking in order to produce data that are motion compensated onto a circular noninertial virtual orbit (Zebker et al., 2010). With this technique, echoes are phase corrected and then resampled from their positions in the actual orbit onto that of an ideal circular reference track. Motion compensation is critical for processing SAR data from airborne platforms, where interactions with the atmosphere lead to turbulent flight trajectories and InSAR phase errors, but is typically unnecessary for the relatively smooth orbits of satellite-base radars (Stevens et al., 1995; Jakowatz et al., 1996; Ulander & Frolind, 1998). Although these short-period orbit errors are less significant for spaceborne platforms, the circular reference track lends itself to the use a spherical coordinate system that greatly simplifies the focusing and positioning equations. In using the precise orbit information along with motion compensation, the output is geodetically accurate and interferograms are produced in a common, well known, coordinate system that facilitates the often complicated tasks of image registration, parameter estimation, and topographic phase removal (Zebker et al., 2010). As it pertains to this thesis, our approach is particularly well suited to efficiently produce stacks of geolocated images (Chapter 5), which we use as the starting point to our multidimensional time-series algorithm presented in Chapter 6.

## 3.2 Spacecraft in a Perfect Circular Orbit

We begin by defining the geometry of a spacecraft traveling in a perfect circular orbit above a nonrotating planet. The path of the satellite lies along a circular arc

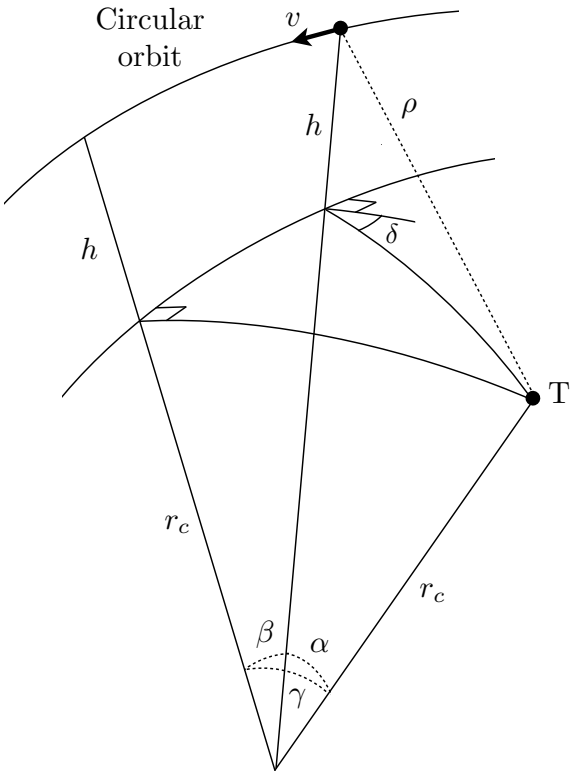


Figure 3.1: Geometry of a spacecraft in a perfect circular orbit, imaging a target at point T. All angles are relative to a sphere approximating the local Earth curvature, with radius $r_c$.

at distance $h$ above a locally spherical Earth (Figure 3.1). The radius of curvature, defined by $r_c$, does not coincide with the distance to the center of the Earth, but defines a sphere approximating the local curvature. The satellite velocity $v$ is constant, such that its position along the arc at time $t$ is given by $vt$. The target position at T is defined by the angle $\gamma$, which is orthogonal to the circular orbit, and by the angle $\beta$, which is along-track from the location of the sensor. Depending on the satellite's position, the LOS is squinted by $\delta$, where the target lies at an angle of $\alpha$ in the boresight plane. We note that this orbit is nonintertial, thus it cannot exist in a physical sense without continuous accelerations applied to the spacecraft. However, this ideal geometry does define the reference orbit to which radar echoes are propagated in our motion compensation processor.

As the sensor traverses the orbit, the target range $\rho$ varies as a function of time $t$, resulting in a time dependent phase

$$\phi(t) = -\frac{4\pi}{\lambda}\rho(t) \tag{3.1}$$

with instantaneous frequency

$$2\pi f(t) = -\frac{4\pi}{\lambda}\dot{\rho}(t)\,, \tag{3.2}$$

where the dot notation of $\dot{\rho}(t)$ represents the time derivative of range. In subsequent expressions, we drop the explicit dependence on $t$, and further note that with the exception of $\gamma$, all angular quantities in Figure 3.1 are also time dependent. Using standard SAR relationships (Cumming & Wong, 2004; Curlander & McDonough, 1991), we define the Doppler centroid and the Doppler rate as

$$f_d = -\frac{2}{\lambda}\dot{\rho} \tag{3.3}$$

and

$$f_{\text{rate}} = \frac{2}{\lambda}\ddot{\rho}\,. \tag{3.4}$$

We now relate these general expressions to the ideal geometry in Figure 3.1. From the law of cosines

$$\rho^2 = (h + r_c)^2 + r_c - 2r_c(h + r_c)\cos\alpha \tag{3.5}$$

and from the spherical law of cosines

$$\cos\alpha = \cos\beta\cos\gamma\,, \tag{3.6}$$

which allows us to write range as

$$\rho^2 = (h + r_c)^2 + r_c^2 - 2r_c(h + r_c)\cos\beta\cos\gamma\,. \tag{3.7}$$

Noting that $\beta = \frac{vt}{(h+r_c)}$ and $\dot{\beta} = \frac{v}{(h+r_c)}$, the derivative of Equation 3.7 with respect to

time is

$$2\rho\dot{\rho} = -2r_c(h + r_c)\cos\gamma(-\sin\beta)\dot{\beta}\ . \tag{3.8}$$

Thus

$$\dot{\rho} = \frac{r_c(h + r_c)\cos\gamma\,(\sin\beta)\,\dot{\beta}}{\rho} \tag{3.9}$$

and the Doppler centroid, from Equation 3.3, is

$$\begin{aligned} f_d &= -\frac{2}{\rho\lambda} r_c(h + r_c)\cos\gamma\,(\sin\beta)\,\dot{\beta} \\ &= -\frac{2v}{\rho\lambda} r_c\cos\gamma\sin\beta\ . \end{aligned} \tag{3.10}$$

In order to define the Doppler rate, we start with Equation 3.8 and differentiate, yielding

$$\begin{aligned} \rho\ddot{\rho} + \dot{\rho}^2 &= r_c(h + r_c)\cos\gamma\cdot\dot{\beta}\cos\beta\dot{\beta} \\ &= r_c(h + r_c)\cos\gamma\sin\beta\dot{\beta}\cdot\frac{\cos\beta}{\sin\beta}\dot{\beta} \\ &= \rho\dot{\rho}\frac{\cos\beta}{\sin\beta}\dot{\beta}\ . \end{aligned} \tag{3.11}$$

Then

$$\rho\ddot{\rho} = \rho\dot{\rho}\frac{\cos\beta}{\sin\beta}\dot{\beta} - \dot{\rho}^2 \tag{3.12}$$

$$\ddot{\rho} = \dot{\rho}\frac{\cos\beta}{\sin\beta}\dot{\beta} - \frac{\dot{\rho}^2}{\rho} \tag{3.13}$$

and finally,

$$f_{\text{rate}} = \frac{2}{\lambda}\left[\frac{\dot{\rho}^2}{\rho} - \dot{\rho}\frac{\cos\beta}{\sin\beta}\dot{\beta}\right]\ . \tag{3.14}$$

In range-Doppler processing, $f_{\text{rate}}$ and $f_d$ are the primary parameters that we need to form the optimal azimuth reference function and focus the image. Compared to a sensor in an arbitrary inertial orbit, these equations are simplified and can be related to the geometry in Figure 3.1. Furthermore, defining the geometry from the precise orbits, we can use the Doppler centroid to determine the location of a target directly from the orbital parameters.

## 3.3 The Motion Compensation Algorithm

A spacecraft in a circular orbit leads to simplified expressions for the positioning and focusing equations. If satellites traveled in this ideal trajectory, then we could form the azimuth matched filter using the derived expressions for $f_d$ and $f_{\text{rate}}$. In reality, however, satellites save fuel by operating in an inertial orbit, which constrains the trajectory to be noncircular. In this section, we describe motion compensation, which is the process of propagating the received radar echoes to a position that is similar to what the sensor would have recorded if it had flown along an ideal circular reference track. In essence, we achieve this by using precise orbit information to resample the position of each pixel and to correct the range-depending phase such that it matches that of a signal measured along the reference orbit. With this approach, we reduce uncertainty in the focusing parameters and produce imagery that is in a well known and geodetically accurate coordinate system.

### 3.3.1 SCH Coordinates

Considering the circular reference orbit of a spaceborne motion compensated trajectory (Figure 3.1), we derive expressions in a right-handed spherical coordinate system, referred to as *sch*. NASA developed this coordinate system for the Shuttle Radar Topography Mission (SRTM) at the Jet Propulsion Laboratory and it is used to simplify the positioning equations on an ellipsoidal Earth. (Hensley et al., 2000a, 2002). Defined in Figure 3.2, the *sch* location of a point gives its position relative to a sphere, with radius $r_c$, approximating the local Earth curvature. In this coordinate system, $s$ is the along-track distance of the satellite path projected onto the *sch* sphere, $c$ is the cross-track distance, and $h$ is the height above the sphere.

We note here that use of *sch* coordinates does not imply a spherical Earth approximation, but merely references points relative to the sphere, rather than the surface of the Earth ellipsoid or geoid. Precise locations in standard datums, such as WGS84 or UTM, are readily converted to *sch* through affine transformations. For more details, Buckley (2000) gives a thorough description of the *sch* coordinate system and the datum transformation matrices.

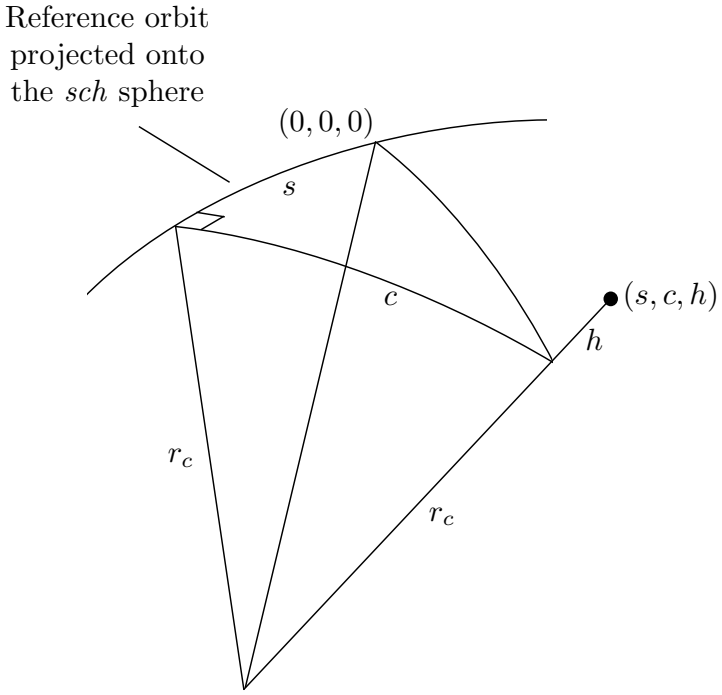


Figure 3.2: Definition of the *sch* coordinate system.

### 3.3.2 Along-Track Position in the Reference Orbit

Following the treatment in Zebker et al. (2010), Figure 3.3 shows a top-down view of the motion compensation reference orbit (Figure 3.1) and the actual ground track of the satellite projected onto the *sch* sphere. Here, we represent the actual location of the satellite in prime notation with position $(s', c', h')$ and the desired position in the reference orbit as $(s, 0, h)$. In the desired position, the cross-track component $c = 0$, because we want the motion compensated signal to appear as if it were imaged precisely along the reference orbit.

Starting with the spherical law of cosines, we see that

$$\cos\frac{d}{r_c} = \cos\frac{s'-s}{r_c}\cos\frac{c'}{r_c}\,, \tag{3.15}$$

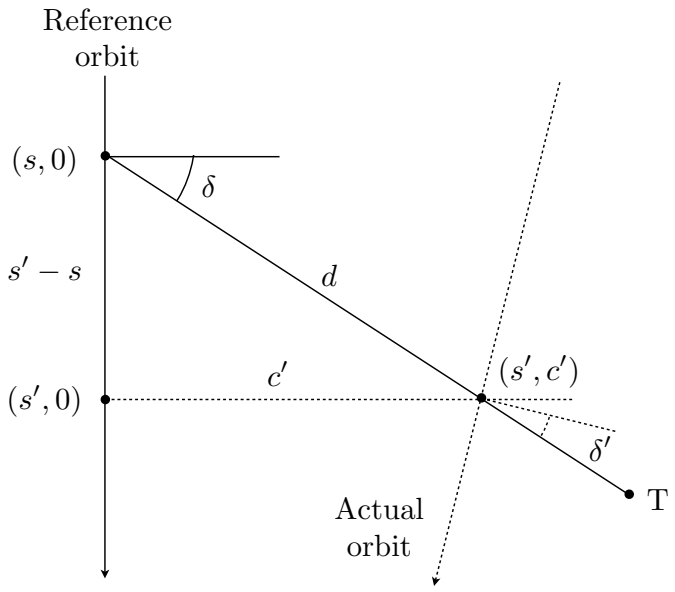


Figure 3.3: Top-down view of the satellite orbits, projected onto the *sch* sphere. The position in the actual obit is represented in primed notation as $(s', c', h')$ and the desired position in the reference orbit as $(s, c, h)$.

while the law of sines yields

$$\frac{\sin(\pi/2 - \delta)}{\sin(c'/r_c)} = \frac{\pi/2}{\sin(d/r_c)} \,. \tag{3.16}$$

In addition, we also write

$$\cos(\pi/2 - \delta) \sin\frac{s' - s}{r_c} \sin\frac{d}{r_c} + \cos\frac{s' - s}{r_c} \cos\frac{d}{r_c} = \cos\frac{c'}{r_c} \,. \tag{3.17}$$

By using Equation 3.15,

$$\cos(\pi/2 - \delta) \sin\frac{s' - s}{r_c} \sin\frac{d}{r_c} + \cos^2\frac{s' - s}{r_c} \cos\frac{c'}{r_c} = \cos\frac{c'}{r_c} \tag{3.18}$$

or

$$\cos(\pi/2 - \delta) \sin\frac{s' - s}{r_c} \sin\frac{d}{r_c} = \cos\frac{c'}{r_c} \sin^2\frac{s' - s}{r_c} \,, \tag{3.19}$$

and thus

$$\cos(\pi/2 - \delta) \sin \frac{d}{r_c} = \cos \frac{c'}{r_c} \sin \frac{s' - s}{r_c} \, . \tag{3.20}$$

Moreover, from Equation 3.16,

$$\cos(\pi/2 - \delta) \frac{\sin (c'/r_c)}{\sin(\pi/2 - \delta)} = \cos \frac{c'}{r_c} \sin \frac{s' - s}{r_c} \, , \tag{3.21}$$

from which

$$\tan \delta \sin \frac{c'}{r_c} = \cos \frac{c'}{r_c} \sin \frac{s' - s}{r_c} \, , \tag{3.22}$$

and

$$\tan \delta \tan \frac{c'}{r_c} = \sin \frac{s' - s}{r_c} \, . \tag{3.23}$$

Relating the squint angle $\delta$ to the reference orbit,

$$\delta = \sin^{-1} \left( \frac{(\cos \gamma - \cos \beta \cos \alpha)}{\sin \beta \sin \alpha} \right) \, . \tag{3.24}$$

Finally, solving for $s$

$$s = s' - r_c \sin^{-1} \left( \tan \delta \tan \frac{c'}{r_c} \right) \, , \tag{3.25}$$

we have the along-track position in the reference orbit as a function of the actual sensor coordinates and the reference geometry. Since the cross-track position $c = 0$ and the height $h$ is defined by the reference orbit, we have the desired position $(s, 0, h)$ in the motion compensated orbit.

### 3.3.3 Range from the Reference Orbit

Besides a shift in the along-track position, the range to a target also varies between the actual and reference orbits. This difference is a consequence of the motion compensation baseline, which is the distance between the actual and reference positions in the plane defined by the antenna boresight. The boresight plane is illustrated in Figure 3.4, where we again denote the position and angles of the actual orbit with primed coordinates. When we image a target position T, it is clear that the ranges $\rho$ and $\rho'$ will differ if the actual orbit does not coincide with the desired reference track.

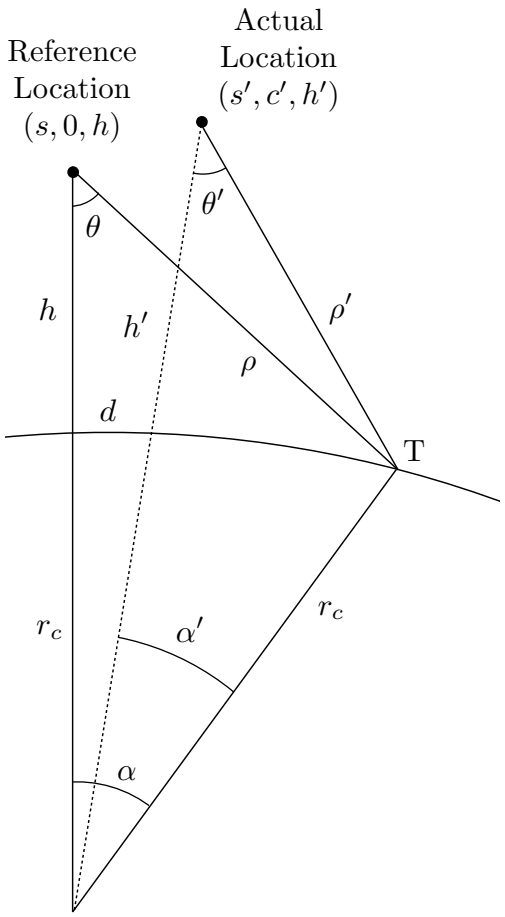


Figure 3.4: Actual and reference slant-ranges in the motion compensation geometry.

We determine the origin-centered angle $\alpha'$ for the actual orbit by

$$\cos\alpha' = \frac{(r_c + h')^2 + r_c^2 - (\rho')^2}{2r_c(h' + r_c)}\,, \tag{3.26}$$

where $\rho'$ is know from the coordinates of the original SAR image. Using the difference $\alpha - \alpha'$ , we find that the cosine of the angle $\alpha$ for the reference location is

$$\cos\alpha = \cos\alpha' \cos\frac{d}{r_c} - \sin\alpha' \sin\frac{d}{r_c}\,, \tag{3.27}$$

where, from Equation 3.15,

$$\sin\frac{d}{r_c} = \sqrt{1-\cos^2\frac{d}{r_c}} = \sqrt{1-\cos^2\frac{s'-s}{r_c}\cos^2\frac{c'}{r_c}}\,. \tag{3.28}$$

Finally, using $\cos\alpha$, we can solve for the range of the target in the reference orbit, such that

$$\rho = \sqrt{(r_c+h)^2 + r_c^2 - 2(r_c+h)r_c\cos\alpha}\,. \tag{3.29}$$

The coordinate pair $(s,\rho)$ from Equations 3.25 and 3.29 defines the target position in the motion compensated image. We need this position to resample the received radar echoes into the geometry of the reference orbit and to cancel the phase difference induced by a non-zero motion compensation baseline. Furthermore, we need the precise locations in both the reference and actual orbits in order to modify the azimuth matched filter our motion compensated range-Doppler processor.

## 3.4 SAR Processing

Expanding the SAR focusing block in Figure 2.4, Figure 3.5 outlines a range-Doppler processor that has been modified to include motion compensation (Zebker et al., 2010). After range compression (Cumming & Wong, 2004), we motion compensate the received signal by resampling to the reference coordinate frame and by correcting the phase for the new slant-range position. Following motion compensation, we compute second order focus corrections, and then apply the range cell migration correction (RCMC) and azimuth matched filters using the simplified expressions from Section 3.2.

Starting with range resampling, the range-compressed signal $x'(\rho')$ is in radar coordinates relative to the actual orbit, which we need to represent in terms of the circular reference track. We write the actual range as a function of the reference range

$$\rho'(\rho) = \sqrt{(r_c+h')^2 + r_c^2 - 2(r_c+h')r_c\cos\alpha'(\rho)}\,, \tag{3.30}$$

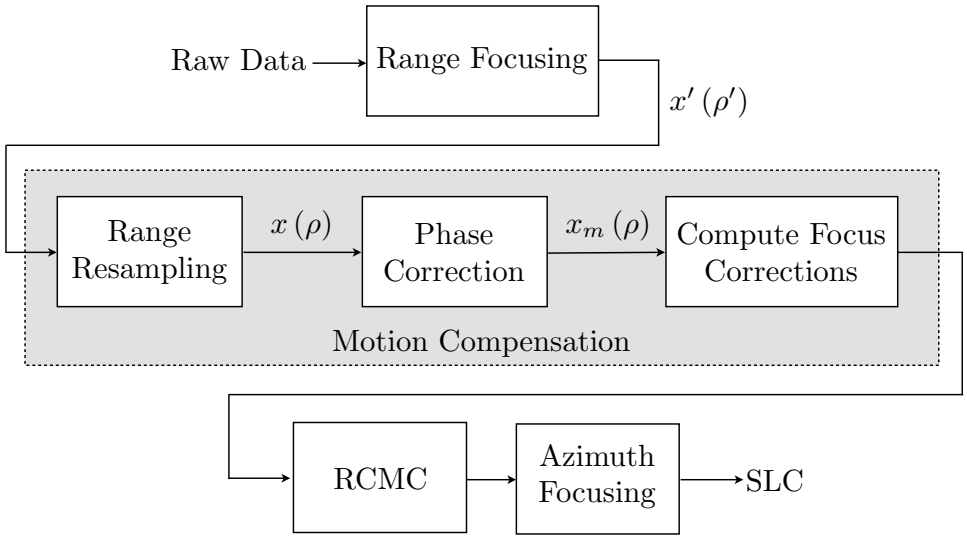


Figure 3.5: Block diagram for motion compensation in range-Doppler processor.

where

$$\alpha'(\rho) = \cos^{-1}\left[\cos\alpha(\rho)\cos\frac{d}{r_c} + \sin\alpha(\rho)\sin\frac{d}{r_c}\right] \tag{3.31}$$

and

$$\alpha(\rho) = \cos^{-1}\left[\frac{(r_c+h)^2 + r_c^2 - (\rho)^2}{2r_c(h+r_c)}\right] , \tag{3.32}$$

which allows us to write the resampled range signal as

$$x(\rho) = x'(\rho'(\rho)) . \tag{3.33}$$

Equation 3.33 represents the propagation of the received echoes from their positions in the actual orbit to their corresponding ranges from the reference track. However, since the phases of the received echoes are proportional to the actual slant-range $\rho'$, we must apply a phase correction to the resampled signal in order to match the expected phase at the new position from the reference orbit.

Using Equation 3.1, the resampled signal $x(\rho)$ has a range-dependent phase of

$$\phi(\rho) = -\frac{4\pi}{\lambda}\rho'(\rho) . \tag{3.34}$$

If we define the motion compensation correction phase as

$$\phi_m(\rho) = \frac{4\pi}{\lambda}\left(\rho'(\rho) - \rho\right) , \tag{3.35}$$

and apply this term as

$$x_m(\rho) = x(\rho) \cdot e^{j\phi_m(\rho)} , \tag{3.36}$$

then the motion compensated signal $x_m(\rho)$ has a range phase that is proportional to the slant-range distance from the circular reference track.

The complex exponential in Equation 3.36 induces a spatial frequency shift, and it cancels the geometric phase dependency on $\rho'$. Along with range resampling, the motion compensation phase correction allows us to use the simplified equations in Section 3.2, but it does not affect any of the other non-geometric sources of path delay at the original position of the echo. For example, topographic and atmospheric phase contributions are preserved, and we can still use these terms for interferometric analysis.

We resampled Equation 3.33 in the range dimension, therefore it exists in the $(s', \rho)$ space. We can compute the transformation from $s'$ to $s$ using Equation 3.25, which relies on the unknown along-track angle $\beta$. The along-track angle is not part of the reference orbit definition, but we can compute it from the data- or attitude-derived Doppler centroid (Madsen, 1989) and Equation 3.10. We note, however, that the data-derived Doppler centroid will differ when estimated from either the range compressed or motion compensated data. During motion compensation, the Doppler centroid shifts by an approximately constant value, which we derive in Section 4.4. If we estimate $f_d$ from the range compressed data, it is important to use a corrected value in Equation 3.10. Once the Doppler centroid is computed, we solve for $\beta$, which leads to the $s$-coordinate and complete knowledge of the motion compensation geometry in Figures 3.1 and 3.4.

At this stage of the processor, we could extend our treatment of range resampling to include a two-dimensional transformation to the $(s, \rho)$ space. Additional interpolation would produce an image in the full reference orbit geometry, but since the focusing equations will not vary based on a shift in the along-track position, we

remain in the $(s', \rho)$ space and account for the $s$-coordinate during coregistration and geolocation. Aside from increasing computational efficiency, this approach reduces phase artifacts by avoiding unnecessary interpolation.

### 3.4.1 Focus Corrections

Our current application of the motion compensation phase correction adequately corrects the first order phase differences between echoes in the actual and reference geometries, however, there are two additional secondary corrections that we need to apply in order to precisely focus the SAR image. The first correction is a scaling of the Doppler frequency rate $f_{\text{rate}}$, which is a result of the target's phase history changing as a function of the actual range, and the second is an additional phase term needed to account for the range dependence of the motion compensation phase shift.

#### Doppler Frequency Rate Correction

During motion compensation, targets are propagated from their actual imaged locations to their corresponding position from the reference orbit. Since the echo's phase history varies as a function of the actual radar geometry (Soumekh, 1999), the motion-compensated phase history will differ from what is expected for a scatterer in the reference orbit. The motion compensation phase correction in Equation 3.35 accounts for the constant and first order differences, but the second order term will vary with the ratio of the motion compensation baseline and the reference range. Therefore, since the second order term determines the Doppler frequency rate, we must apply a correction to Equation 3.14 in order to properly compute the frequency rate for the azimuth matched filter.

To illustrate, consider the simplified geometry in Figure 3.6, where the reference orbit, the actual orbit, and the scatterer are coplanar, and we are processing point P to a zero Doppler geometry. We define $b(t)$ as the the motion compensation baseline, which is the distance between the actual and reference ranges, and $\rho_c$ as the range of closest approach. Following the derivation in Zebker et al. (2010), the range history,

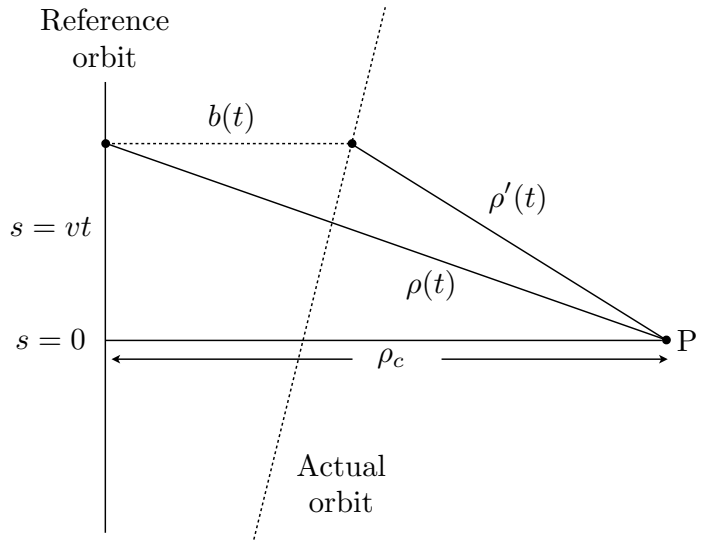


Figure 3.6: Simplified motion compensation geometry to illustrate the secondary correction to the Doppler frequency rate, where the reference orbit, the actual orbit, and the target all lie in the plane of the page and the point P is processed at zero Doppler.

with respect to the reference orbit, is

$$\rho^2(t) = \rho_c^2 + v^2 t^2 \,, \tag{3.37}$$

which can be approximated by a Taylor series expansion as

$$\rho(t) \approx \rho_c + \frac{1}{2}\frac{v^2 t^2}{\rho_c} \,, \tag{3.38}$$

leading to a Doppler rate of

$$f_{\text{rate}} = -\frac{2v^2}{\lambda \rho_c} \,. \tag{3.39}$$

Using the same Taylor series expansion, we write the range history of the actual

return as

$$\begin{aligned}\rho'(t) &\approx \rho_c - b(t) + \frac{1}{2}\frac{v^2t^2}{(\rho_c - b(t))} \\ &\approx \rho_c - b(t) + \frac{1}{2}\frac{v^2t^2}{\rho_c}\left(1 - \frac{b(t)}{\rho_c}\right) .\end{aligned} \tag{3.40}$$

Next, noting that we add the motion compensation baseline to the phase history in Equation 3.36, we write the motion-compensated range history as

$$\rho_m(t) = \rho_c + \frac{1}{2}\frac{v^2t^2}{\rho_c}\left(1 - \frac{b(t)}{\rho_c}\right) . \tag{3.41}$$

Comparing Equations 3.38 and 3.41, we see that the reference and motion-compensated range histories vary by a factor that depends on the ratio of the reference range and the motion compensation baseline. Since the Doppler rate depends on the range history, we apply a correction to $f_{\text{rate}}$ to match the range history of the echo in the actual imaging geometry. This correction does depend on the time-varying baseline, but due to the fact that the reference orbit is chosen to be highly parallel to the actual orbit, we find that a locally constant approximation of the baseline is sufficiently accurate for many radar satellites. In practice, we set $b(t) \approx b$ on a patch-by-patch basis and write the actual Doppler frequency rate as

$$f'_{\text{rate}} = f_{\text{rate}}\left(1 - \frac{b}{\rho_c}\right) . \tag{3.42}$$

The geometric construct in Figure 3.6 is merely a simplification to understand how the Doppler frequency rate can change between the actual and reference orbits. To compute the change in an arbitrary geometry, we use Equation 3.14 and write

$$\begin{aligned}f_{\text{rate}} &= \frac{2}{\lambda}\left[\frac{\dot{\rho}^2}{\rho} - \dot{\rho}\frac{\cos\beta}{\sin\beta}\dot{\beta}\right] \\ &= \frac{2}{\lambda}\left[\frac{\lambda^2 f_d^2}{4\rho} + \frac{\lambda}{2}\frac{f_d}{\tan\beta}\dot{\beta}\right] \\ &= \frac{\lambda f_d^2}{2\rho} - \frac{2v^2}{\lambda\rho}\frac{r_c}{(h + r_c)}\cos\alpha .\end{aligned} \tag{3.43}$$

Thus, the difference in $f_{\text{rate}}$ between the scatter at its actual position and its motion-compensated position is

$$\begin{aligned} f_{\text{rate}} - f'_{\text{rate}} &= \frac{\lambda f_d^2}{2}\left(\frac{1}{\rho} - \frac{1}{\rho'}\right) - \frac{2v^2}{\lambda}\frac{r_c}{(h+r_c)}\left(\frac{\cos\alpha}{\rho - \frac{\cos\alpha'}{\rho'}}\right) \\ &= \frac{\lambda f_d^2}{2}\left(\frac{\rho' - \rho}{\rho\rho'}\right) - \frac{2v^2}{\lambda}\frac{r_c}{(h+r_c)}\left(\frac{\rho'\cos\alpha - \rho\cos\alpha'}{\rho\rho'}\right) \\ &\approx \frac{\lambda f_d^2}{2\rho}\frac{b(t)}{\rho} - \frac{2v^2}{\lambda\rho}\frac{r_c}{(h+r_c)}\cos\alpha\frac{b(t)}{\rho} \\ &= f_{\text{rate}}\frac{b(t)}{\rho}\,, \end{aligned} \tag{3.44}$$

which holds under the assumption that $h' \approx h$. Comparing Equations 3.42 and 3.44, the general correction is equivalent to the simplified case when $b(t)$ is slowly changing and when $\rho_c = \rho$. Therefore, we initially compute $f_{\text{rate}}$ from Equation 3.14, correct it to match the range history in the actual geometry as in Equation 3.42, and use $f'_{\text{rate}}$ to focus the motion compensated data.

### Range Migration Phase History Correction

The goal of the motion compensation phase correction is to advance the phase of each echo by an amount that corresponds to the difference between the actual and reference ranges at the boresight location of the scatterer. We apply this correction in the form of Equation 3.35, but due to range migration, the distance of the echo changes across the phase history, and motion compensation incorrectly adds an additional phase term that is proportional to the range migration distance. Since we can compute this distance from known SAR relationships, we remove the extra phase by applying a phase correction factor to each echo before azimuth focusing.

For a single echo, the degree of range migration depends on the boresight position of the scatterer and the time within the range history. Since a SAR scene consists of the the superposition of phase histories from several echoes at difference azimuth positions, a single point in the time-domain image would require an independent correction for each contributing scatterer. This scenario is analogous to the range cell

migration correction (RCMC) problem, where we apply a Fourier transform in the azimuth direction to align the echoes in the Doppler domain (Curlander & McDonough, 1991). After this transformation, we can apply a single correction to all echoes at the same reference range, which greatly increases the efficiency of the correction. From Cumming and Wong (2004), we write the Doppler-domain range migration as

$$\rho_{\text{migration}} = \frac{\lambda}{4\pi} \cdot \pi \cdot \frac{1}{f'_{\text{rate}}} f^2 \,, \tag{3.45}$$

where $f$ is the Doppler frequency and $f'_{\text{rate}}$ is the corrected Doppler frequency rate. It follows that the phase correction is proportional to the migration distance by the gradient of the motion compensation correction phase, evaluated at the boresight range

$$\begin{aligned} \phi_{\text{correction}} &= \rho_{\text{migration}} \cdot \frac{\partial}{\partial \rho} \left( \frac{4\pi}{\lambda} (\rho'(\rho) - \rho) \right) \Bigg|_{\rho=\rho_c} \\ &= \frac{\lambda}{4 f_{\text{rate}}} \cdot f^2 \cdot \frac{\partial}{\partial \rho} \left( \frac{4\pi}{\lambda} (\rho'(\rho) - \rho) \right) \Bigg|_{\rho=\rho_c} , \end{aligned} \tag{3.46}$$

which gives us the addition phase added by the motion compensation correction. We subtract this phase term to adjust the Doppler-domain data before applying the azimuth matched filter.

### 3.4.2 Processing Summary

The overall signal flow of our motion compensation range-Doppler processor is not significantly different than traditional range-Doppler processors (Curlander & McDonough, 1991; Cumming & Wong, 2004). Referring to Figure 3.5, we process the received data with a standard match filter to focus in the range dimension. Motion compensation consists of range resampling by Equation 3.33 and phase correction by Equation 3.36. In our implementation, we compute the focus correction factors in the motion compensation module and save those with other parameters that describe the reference geometry.

After computing the Fourier transform in the azimuth dimension, we apply the

RCMC resampling in the Doppler-domain to account for range cell migration. At this point, we can apply the phase focus correction from Equation 3.46, or wait and apply it as an addition phase term in the azimuth focusing module. Finally, while still in the Doppler-domain, we calculate the azimuth matched filter, using the corrected Doppler frequency rate in 3.42. Following an inverse Fourier transform in azimuth, we have a focused SAR image in the well defined reference geometry.

### 3.4.3 Limitations

Foremost, our approach to SAR focusing depends on the accuracy of the orbit information to precisely define the relationship between the actual and reference orbits. In historic sensors, we could not rely on the measured trajectories, but with technological advances in inertial measurement units (IMUs) and GPS, modern sensors have standard orbital errors on the order of tens of centimeters or less (Tapley et al., 1994; Scharroo & Visser, 1998; Yamamoto, 2008), which is sufficiently low for accurate motion compensation processing. Aside from orbital accuracy, there are several other conditions that can potentially degrade the image quality of our processor. These are the following.

1. Baseline variation over a patch: In the derivation of the Doppler frequency rate correction we made the assumption of an approximately constant motion compensation baseline, such that $b(t) \approx b$. This approximation lead to a focus correction factor that was constant in azimuth and varied in range. In our implementation, we further assume that a single motion compensation baseline describes the entire two-dimensional patch and we apply a single Doppler rate correction factor. We still use the instantaneous baseline for motion compensation resampling and phase correction, but due to our frequency domain implementation, a single baseline is assumed to correct the Doppler frequency rate of the entire patch at once. In practice, we find that approach is valid for many radar satellites, but if the chirp rate varies over the patch by more than one part in the azimuth time-bandwidth product, some defocusing will occur.

2. Baseline resolution: If the update frequency of the orbit position measurements

is not high enough then errors in the motion compensation baseline can lead to geometric distortions that will result in interferometric phase errors. For spaceborne sensors, which tend to have smooth trajectories, baseline resolution is not a problem. Current satellite systems update orbit positions every 15 seconds or less, and the baseline at each along-track position can be interpolated with sufficient accuracy by hermite polynomials (López & Temme, 1999). However, for airborne sensors, which are prone to turbulent trajectories, short scale fluctuations in the baseline will not be captured by interpolation, and without sufficient sampling, these errors can lead to substantial artifacts in both the SAR and InSAR images.

3. Cross-track and vertical velocities: We construct the reference orbit so that sensor velocity is entirely along the s-axis. If the $c$ and $h$ velocities in the actual orbit are large, then our estimate of the Doppler centroid will vary significantly between the actual and reference geometries. If we process data to an incorrect Doppler centroid, the mismatch of the azimuth filter leads to loss of signal and defocusing. In Section 4.4, we derive an correction to transform the Doppler centroid estimated from the received data to the reference geometry, however, this expression also assumes that the $c$ and $h$ velocities are small. To avoid large velocity discrepancies, we choose the reference orbit so that is it highly parallel to the actual orbit. We discuss orbit selection in the following section.

## 3.5 Interferogram Formation

Following image formation in Section 3.4, we have a well-focused SAR image, motion compensated to the known reference geometry. As described in Section 2.3, the next step in InSAR processing is interferogram formation from a pair of SLCs. If the SLCs are precisely aligned, we can perform a pixel-by-pixel conjugate multiplication to compute the interferometric phase. If the SLCs are misregistered, even by a fraction of a pixel, we must perform coregistration to align the images. The InSAR processing chain is illustrated in Figure 2.5.

Within the limitations described in Section 3.4.3, we are free to choose any reference geometry for the SLCs. Since coregistration is facilitated by similar geometries, we choose the same reference orbit for both the master and slave images so that the coordinate frames are are approximately the same. We want to minimize the motion compensation baseline for both SLCs, and process to the same reference geometry, therefore we choose a reference orbit at the average height and heading of the two scenes, with an along-track spacing set by the average velocity. This approach reduces the vertical and cross-track velocities and lessens the along-track baseline variation, while retaining a common reference track for both images.

We are careful to point out that the coordinates will be similar, but not identical, when processing to the same reference track. This discrepancy comes from the fact that the processing equations were calculated under the assumption of no topography and no propagation delays through the ionosphere and troposphere. Ignoring these factors greatly simplifies the relationship between the reference and actual geometries and typically aligns the images within a few pixels. Before we compute the interferometric phase, we perform a resampling based on amplitude cross correlation to align the images. We refer to this resampling as coregistration, and because the images are in similar coordinates, this process is efficient and can be implemented without prior knowledge of topography or atmospheric conditions.

### 3.5.1 Coregistration

Traditionally, coregistration is one the most time consuming and error-prone steps in the InSAR processing chain. We coregister SLCs by computing an offset field between the two images and resampling the second SLC to the precise coordinates of the first. We can calculate this transformation from the radar geometries and topographic heights, but since the topography is not known a priori in the radar coordinates, an amplitude cross correlation based scheme is used to compute the offsets. Once the offsets are known, we resample the second SLC to the first and proceed with interferogram formation.

The search space for the offsets depends on the size of the cross correlation windows. For example, if we correlate two $N \times N$ pixels windows, the maximum offset that we can measure is $\pm(N-1)$ pixels in either dimension. Since the acquisition start times can vary by seconds, the offsets can be as large as several hundreds of pixels. To avoid large correlation windows, which require extensive calculations, we initially shift the image by a constant coarse offset, before estimating the spatially-varying fine offsets.

In traditional InSAR processors, the coarse offsets were computed by downsampling the images and estimating offset fields at a coarser resolution. Here the window size could remain small, and the correlation results would estimate shifts at the precision of the downsample factor. This scale is not sufficient for coregistration, but it can be useful in estimating the constant offsets between the images. Although this approach was used for many years, it is prone to failure. For example, images consisting mostly of water, or those without prominent features do not produce consistent correlation peaks, resulting in a failure to estimate the coarse offsets, and ultimately the fine offsets.

Coarse offset estimation is substantially easier if we use the motion compensated SLCs. An example is shown in Figure 3.7, where both images exist in nearly the same $(s, \rho)$ space, but are misaligned on a pixel-by-pixel basis. Defining the discrete vectors of s-positions for $\text{SLC}_1$ and $\text{SLC}_2$ as $s_1[m]$ and $s_2[m]$, and the discrete vectors of ranges $\rho_1[n]$ and $\rho_2[n]$, we write the coarse offsets as

$$\begin{aligned} \Delta s_0 =& \frac{s_1[0] - s_2[0]}{s_2[1] - s_2[0]} \\ \Delta \rho_0 =& \frac{2f_s}{c} \left(\rho_1[0] - \rho_2[0]\right) \ , \end{aligned} \tag{3.47}$$

where $c$ is the speed of light and $f_s$ is the range sampling frequency. This simplistic approach is only possible when we motion compensate the SLCs to the same coordinate frame, and it allows us to align the discrete data to a local offset of only a few pixels. In addition, since we do not use the radar amplitudes in our coarse offset calculation, our approach will not fail based on the amplitude characteristics of the

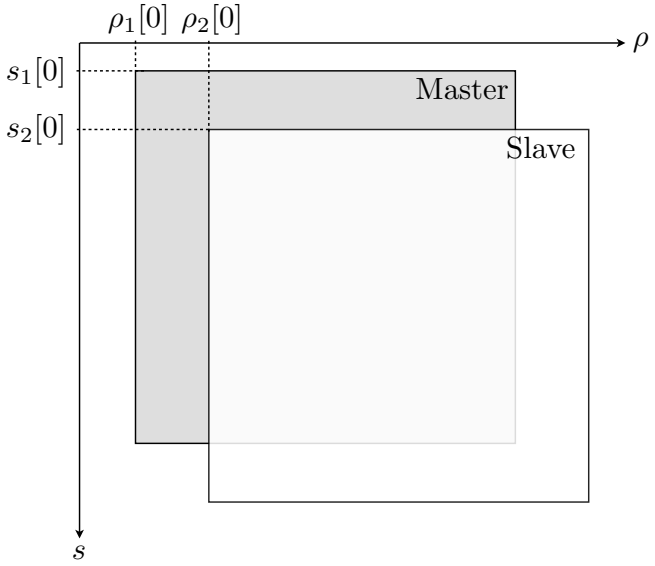


Figure 3.7: Coarse alignment of master and slave SLCs after motion compensation.

scenes.

As previously discussed, the motion compensated SLCs will not be exactly aligned, due to the no-topography assumption in the reference orbit model. Figure 3.8 illustrates the effect of ignoring topography and shows why different positions of the Earth will be imaged when the master and slave SLCs are processed to the same reference track. Using the actual and reference orbit positions, we compute $\rho_1'(\rho)$ and $\rho_2'(\rho)$ to image a point P at a distance $\rho$ from the reference orbit. If there were no topography, both the master and slave echoes at range $\rho$ would correspond to the point P and coregistration would not be necessary. However, as shown in the figure, the master scene images point M, which is still at a distance of $\rho_1'(\rho)$, and the slave scene images point S, which is also at the correct range $\rho_2'(\rho)$. Despite the fact that the computed ranges are correct, it is clear that these points do not coincide, thus we need a spatially-varying fine registration to precisely align the images.

Once the coarse offsets are computed from Equation 3.47, we shift the slave SLC and use a series of amplitude cross correlations to estimate the fine offset field. We omit the details of the correlation calculation, but refer the reader to Li and Bethel

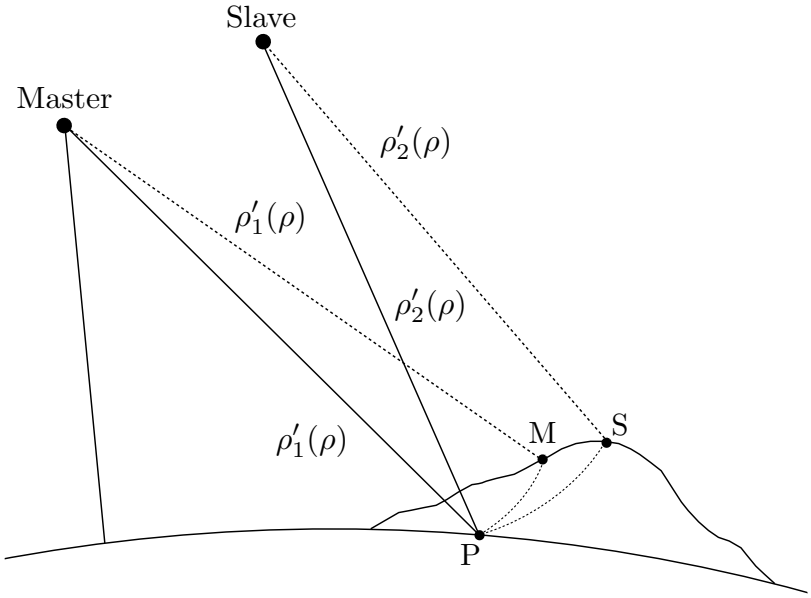


Figure 3.8: Actual imaged locations for master and slave SLCs. Each SLC is motion compensated to the same reference orbit without accounting for topography.

(2008) and Nitti et al. (2011) for implementation details. Our amplitude cross correlation approach is the same as traditional coregistration, with the exception that we use much smaller correlation windows. Small window size is a benefit of motion compensation and is possible because of the nearly identical coordinates of the master and slave SLCs. In practice we use $10 \times 10$ pixels windows, distributed across the scene, to estimate the fine offsets $\Delta s[m]$ and $\Delta\rho[n]$. Defining $I_1$ as the master SLC and $I_2$ as the slave, we write the discrete interferogram as

$$I\left[m,n\right] = I_1\left[m,n\right] \cdot I_2^*\left[m - \Delta s\left[m\right] - \Delta s_0, n - \Delta\rho\left[n\right] - \Delta\rho_0\right] \ , \tag{3.48}$$

where the slave is shifted by the integer coarse offsets and resampled using the decimal fine offsets.

### 3.5.2 Topographic Correction

When forming interferograms, as described in the previous sections, both SLCs have the same geometric phase after motion compensation, therefore the curved-Earth term in Equation 2.2 cancels. However, since topographic phase depends on the actual geometries, the interferograms still have a phase term that is proportional to topography. For deformation applications, such as the time-series estimation in Chapters 6 and 7, we must compensate for this term and "flatten" the interferogram.

To compute the topographic phase term, we need to know the elevation or $h$-coordinate at each pixel in the interferogram. Worldwide DEMs are available from NASA in the SRTM archive, however, these models are given in the WGS84 projections, so we must first transform the DEM to radar coordinates. Once the elevations are known, we compute and subtract the topographic phase associated with each pixel in the interferogram.

Our motion compensation reference geometry is well known, but there is no closed-form solution to convert *sch* coordinates, or any radar coordinates, to the exact latitude, longitude, elevation position in a DEM. As a result, we developed an iterative approach to solve for the corresponding position in the DEM. Our approach converges quickly and uses the simple spherical equations from the reference geometry.

Consider the one-dimensional case in Figure 3.9. This example corresponds to a zero-Doppler imaging geometry, and will serve to illustrate our iterative approach. On the $i^{th}$ iteration, we set the topographic height to $h_i$, and estimate the angle $\alpha_i$ as

$$\cos\alpha_i = \frac{(h_p + r_c)^2 + (r_c + h_i)^2 - \rho^2}{2(h_p + r_c)(r_c + h_i)}\,, \tag{3.49}$$

where $\alpha_i$ is the origin-centered angle in Figure 3.4 and the sensor platform is at a known position $(s_p, 0, h_p)$. With this angle, we calculate the cross-track position $c_i = \alpha_i r_c$, and use the *sch* coordinates $(s_p, c_i, h_i)$ to compute the corresponding latitude and longitude With this position, we then retrieve the elevation of the location from the DEM and set this as our new height estimate $h_{i+1}$. When the new DEM height satisfies Equation 3.49, or $h_i = h_{i+1}$, the algorithm has converged, and we use this value as the topographic height at the current position in the interferogram.

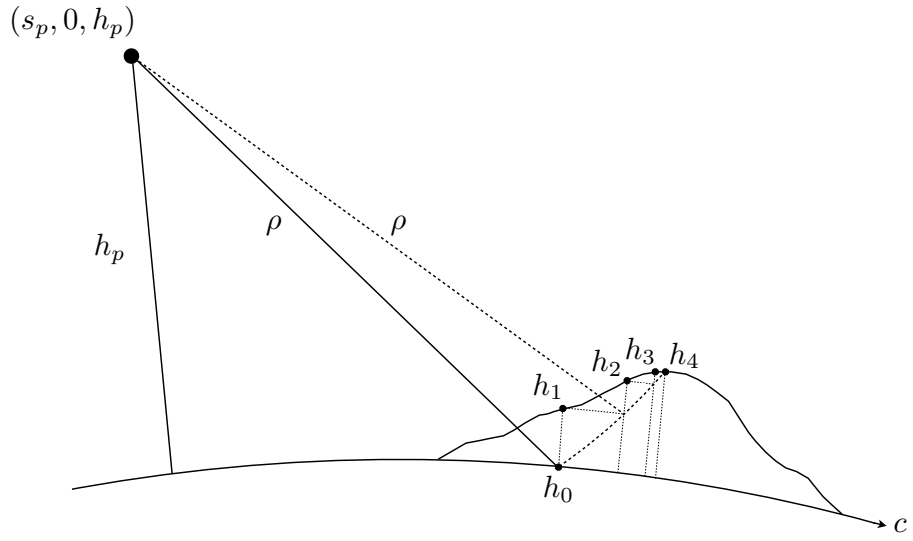


Figure 3.9: Example of the iterative approach for topographic height in *sch* coordinates.

Referring to Figure 3.9, $c_i$ is constrained to lie along a circle of radius $\rho$ from the platform and the estimated height is updated as the corresponding elevation at the current $c$ position. Our algorithm traverses the circle until the DEM elevation intersects, indicating a topographic height that matches the reference geometry. This example uses an initial height of $h_0 = 0$ and converges in four iterations. We note that any initial height may be used, for instance the mean topographic height, and a more accurate initial condition will expedite convergence of the algorithm. In practice, we find that using $h_0 = 0$ leads to convergence in less than five iterations for typical radar satellite geometries.

For most interferograms, the geometry is skewed by the radar squint, as in Figure 3.1, such that $\alpha$ represents an angle in the boresight plane and the $s$ and $c$ coordinates of the topographic point will lie along the intersection of this plane and the *sch* sphere. For the more general squinted geometry, we calculate the along-track angle

$$\tan \beta_i = -\frac{f_d \lambda \rho}{v r_c} \left( \frac{(r_c + h_p)(r_c + h_i)}{(r_c + h_i)^2 + (h + r_c)^2 - \rho^2} \right) \tag{3.50}$$

and use this to compute the along-track position

$$s_i = s_p + r_c \beta_i \, . \tag{3.51}$$

and the cross-track position

$$c_i = r_c \cos^{-1}\left(\frac{\cos\alpha_i}{\cos\beta_i}\right) \tag{3.52}$$

of the topographic point. Following the procedure of the zero Doppler example, we calculate the latitude and longitude of the *sch* point $(s_i, c_i, h_i)$ and extract the corresponding height from the DEM. When the algorithm converges, we save the height $h = h_i$ as corresponding to the position $(s_p, \rho)$ in the interferogram.

Finally, given the elevation of the pixel, we evaluate the topographic contribution as the phase expected from moving a scatter from the reference sphere to the true elevation as

$$\phi_{\text{topo}} = \frac{4\pi}{\lambda}\left(\mathbf{u}_h - \mathbf{u}_0\right) \cdot b(t) \tag{3.53}$$

where $\mathbf{u}_h$ and $\mathbf{u}_0$ are the unit look vectors for a target at elevation and on the reference sphere, respectively, and $b(t)$ is the InSAR baseline vector. We subtract this phase at each point in the interferogram to remove the topographic signature, which leaves only the deformation, atmospheric, and noise terms in the interferometric phase.

We note that errors in the orbit determination, plus unmodeled delays in the propagation medium, can lead to slight distortions in the topographically corrected interferograms. These distortions manifest as uncompensated phase artifacts, which can degrade the accuracy of the interferometric phase. If these errors are significant, we can perform a second registration of the interferogram amplitude with a shaded relief map of the DEM elevations. This step serves to further align the interferogram with the DEM, and following this correction, we subtract $\phi_{\text{topo}}$ from the resampled image. Similar to coregistration, the alignment error will be small, on the order of a few pixels or less, and since the interferogram is typically multilooked, the number required of cross correlations is substantially reduced by comparison.

### 3.5.3 Time-Series Processing

As we discussed in Section 2.6, time-series processing uses many SAR scenes to estimate the temporal evolution of deformation. For a set a $N$ SAR images, there are a total of

$$M = \frac{N-1}{2}N \tag{3.54}$$

possible interferometric combinations, all of which must be coregistered to combine phase measurements. Similar to the formation of a single interferogram, we can use motion compensation to simplify processing and increase computational efficiency.

For time-series processing, we still want to minimize the motion compensation baseline and process all SLCs to the same reference geometry. To select the orbit, we choose the average height and heading across the set of SAR scenes, with an along-track spacing set by the overall average velocity. In dealing with multiple geometries, there may be outlying orbits that bias the calculation and increase the average motion compensation baseline. We find that large motion compensation baselines introduce a spectral shift that, if unaccounted for, will lead to artifacts in the interferograms. Estimation of the spectral shift and removal of these artifacts is the topic of Chapter 4, although we could reduce these effects by removing outlying geometries before calculation of the reference orbit. For the time-series results in Chapter 7, we used the unmodified, average reference orbit and relied on our approach to correct for the effects of large motion compensation baselines.

As with the case of a single InSAR pair, coregistration for time-series applications will be simplified in the motion compensated geometry. Since we process to a the same reference track, we compute the coarse offsets with Equation 3.47 and coregister with small correlation windows. However, instead of individually coregistering all $M$ interferograms, we produce $N$ SLCs, coregister each to a single master geometry, and then form the set of interferograms. Since coregistration is one of the slowest steps in an InSAR processor, this strategy dramatically improves the efficiency of the time-series processor and alleviates the need to individually reregister interferograms before combined analysis.

## 3.6 Summary

We have developed a new approach to spaceborne InSAR processing that takes advantage of the highly accurate orbit determination of modern satellites to increase the efficiency and accuracy of InSAR processing. Using the orbit information, we derived the relationships between the actual received geometry and an ideal circular reference track, which allowed us to use motion compensation to propagate the received echoes to the well defined and simplified reference geometry. Once the echoes were transformed this new coordinate frame, the focusing equations were greatly simplified and the well-defined geometry could be exploited for more efficient processing.

We found that following motion compensation, two focus corrections were needed to adjust the phase history of an echo so that it matched what was expected for a scatterer in the reference geometry. We derived these corrections and discussed efficient methods of implementation in the Doppler frequency domain. These corrections required very few additional calculations and were sufficient to allow direct use of the simplified focusing equations for the circular orbit. Since these equations are well known in the reference geometry, there is no need for ad hoc autofocus routines, which are traditionally used to compensate for poorly defined geometries.

We also described the coregistration and topographic phase removal steps in the InSAR processor. For coregistration, we found that the amplitude cross correlation procedure used to align the SLCs was simplified when processing each SLC to the same reference orbit. In addition, by using the orbit information instead of the SLC amplitude features, the success of coregistration was not dependent on the distribution of large bright features in the image. For topographic phase removal, we developed an iterative algorithm to estimate the topographic relief in radar coordinates. Our approach used the spherical equations from the reference orbit geometry, and was relatively simple when compared to brute force methods that use ellipsoidal Earth models.

# Chapter 4

# Spectral Shifts from Motion Compensation

## 4.1 Introduction

In Section 3.5, we discussed the selection of the reference orbit for both single interferometric pairs and multiple sets of data used for time-series analysis. We saw that by processing each SAR image to a common reference orbit, coregistration was greatly simplified and stacks of interferograms were produced in identical coordinate frames. Our strategy for choosing a common reference track consisted of using the average orbit height and heading across the set of SAR scenes, with an along-track spacing set by the overall average velocity. Our approach results in reduced motion compensation baselines and cross-track velocities for each scene, however, inherent variations in the satellite's repeat pass trajectories can make it difficult to optimize these objectives, while approximating several different orbits. Because the orbits do not repeat exactly, each scene is still processed with some motion compensation baseline.

In this chapter, we examine the effects of large motion compensation baselines and cross-track velocities when processing sets of time-series data to a common global reference track. We find that the motion compensation phase correction induces a range spectral shift that is proportional to the motion compensation baseline and that cross-track velocities lead to a shift in the Doppler spectrum. These shifts,

if unaccounted for in the InSAR processing chain, will cause a loss in coherence commensurate with the amount of motion compensation. We derive the spectral shifts using the geometry shown in Chapter 3 and present the changes in an InSAR processor that are necessary to restore coherence. Finally, we present results using data from the ALOS PALSAR platform, where we show the coherence with both local and global reference orbits. Using the presented techniques, we illustrate that coherence can be restored, even with large motion compensation baselines.

## 4.2 Background

From Section 3.4, the basic premise of motion compensation consists of resampling and applying a time-domain phase correction. The phase correction is a range-varying complex exponential function, which causes a shift of the range spectrum. When processing to a common reference orbit, this shift aligns the range spectra and is the reason why motion compensated interferograms do not contain the curved-Earth phase gradient. Stacy (1997) showed that this shift is analogous to the SAR wavenumber shift, where the ground reflectivity spectrum is translated by an amount proportional to the spatial baseline of the interferometric pair. In the case of motion compensation, the range spectral shift has a similar functional form, but is proportional to the motion compensation baseline. Previously, Prati and Rocca (1993) studied the wavenumber shift to increase SAR resolution and Gatelli et al. (1994) used the shift to define common band filters that improve interferometric coherence.

The wavenumber shift defines an offset in the ground reflectivity spectrum, where this received signal is windowed in the frequency domain by the envelope of the transmitted pulse spectrum. In contrast, the motion compensation phase correction is applied during SAR processing such that it shifts both the ground reflectivity and pulse spectrum. As a result, the range spectrum of the motion compensated signal is centered at a nonzero carrier frequency, and if we do not account for this carrier in the InSAR processing chain, it will distort the single look complex image (SLC) spectrum and cause a loss in coherence. Coherence loss is a consequence of the interpolation and filtering kernels being centered at zero frequency. For a signal on a carrier,

uncompensated interpolation will not properly reconstruct the data, which increases phase noise and causes defocus. For our InSAR processor, the motion compensation spectral shifts affect coregistration, range cell migration correction (RCMC), and any other filtering steps before interferogram formation. For instance, common band filtering (Gatelli et al., 1994; Guillaso et al., 2006; Reigber, 1999; Schwabisch & Geudtner, 1995), which typically improves coherence, must be modified for motion compensation processing, otherwise it will degrade the signal.

Similarly, cross-track velocities result in a shift of the Doppler centroid that must also be considered in the InSAR processor. From Equation 3.3, the Doppler centroid is based on the range history rate of change, which is directly related to the sensor velocity and the orientation of the orbit. If the reference orbit is not parallel to the actual orbit, there will be nonzero velocities in the $c$ and $h$ directions. This condition implies that the squint angle is different relative to the actual and reference orbits, thus the Doppler centroid will be dissimilar in the two coordinate frames. Figure 3.3 illustrates this scenario, where the actual and reference orbits are not parallel, and the squint angles differ such that $\delta \neq \delta'$. In addition to the aforementioned concerns of interpolation and filtering on a carrier, if we use an incorrect value for the Doppler centroid, the center frequency of the azimuth reference function will be offset, and the resulting SAR images will have reduced resolution and lower SNR (Bamler, 1991).

The interpolation and filtering implications of the spectral shifts are generally ignored in the current literature because typical airborne motion compensation applies a small correction based on the deviation of the actual flight track from an ideal local reference path (Ulander & Frolind, 1998). This was also the case for the NASA SRTM topographic data sets where the actual orbit was compensated locally to short idealized segments (Hensley et al., 2000b). Hence, the motion compensation baseline and the corresponding spectral shifts are negligible. In this thesis, we focus on processing multiple spaceborne data sets to a common reference orbit, where the reference track is not local to each scene. In the context of time-series analysis, a set of images is processed to a global average reference orbit that must approximate all of the actual trajectories, therefore large variations across the set of orbit positions and headings can result in significant spectral shifts.

## 4.3 Range Spectral Shift

In Chapter 3, we derive the motion compensation phase correction as the term needed to correct the echoes after they are propagated to their new positions in the reference orbit. We apply this correction as multiplication by a complex exponential in the form of $e^{j\phi_m(\rho)}$, where

$$\phi_m(\rho) = \frac{4\pi}{\lambda}\left(\rho'(\rho) - \rho\right) \ . \tag{4.1}$$

The correction phase is a function of the reference range $\rho$, so that linear variation will result in a uniform shift of the motion compensated range spectrum, while quadratic variation will cause a spatially-varying smearing of the spectral components.

In general, the correction phase is a complex function of the actual and reference orbit geometries. We can express Equation 4.1 in terms of the spherical model from Chapter 3, however, these equations are cumbersome and offer little insight into the first and second-order behavior of $\phi_m(\rho)$. Instead, we use a second-order Taylor expansion about the mid-range and write

$$\phi_m(u) \approx \frac{4\pi}{\lambda}\left(\phi_0 + \phi_1 u + \phi_2 u^2\right) \ , \tag{4.2}$$

where $u = (\rho - \rho_0)$ and $\rho_0$ is the mid-swath range in the reference orbit. We compute the coefficients in Appexdix A, using the flat-Earth model in Figure 4.1. We note that this is a standard approximation, which was used by Prati and Rocca (1993) and Gatelli et al. (1994) in their analysis of the SAR wavenumber shift. Defining $\theta_0$ and $\theta_0'$ in Figure 4.1 and letting $\Delta\theta_0 = \theta_0 - \theta_0'$, the Taylor series coefficients are

$$\phi_0 = (\rho_0' - \rho_0) \tag{4.3}$$

$$\phi_1 = \frac{\sin\theta_0' - \sin\theta_0}{\sin\theta_0} \approx -\frac{\Delta\theta_0}{\tan\theta_0} \approx -\frac{b_{\perp,0}}{\rho_0'\tan\theta_0} \tag{4.4}$$

$$\phi_2 = \frac{1}{2}\left(\frac{1}{\rho_0'}\frac{\cos^2\theta_0'}{\sin^2\theta_0} - \frac{1}{y_0}\frac{\sin\theta_0'}{\tan^2\theta_0}\right) \ , \tag{4.5}$$

where the values of $\theta_0$ and $\theta_0'$ will be marginally smaller if we compute them with a curved-Earth model.

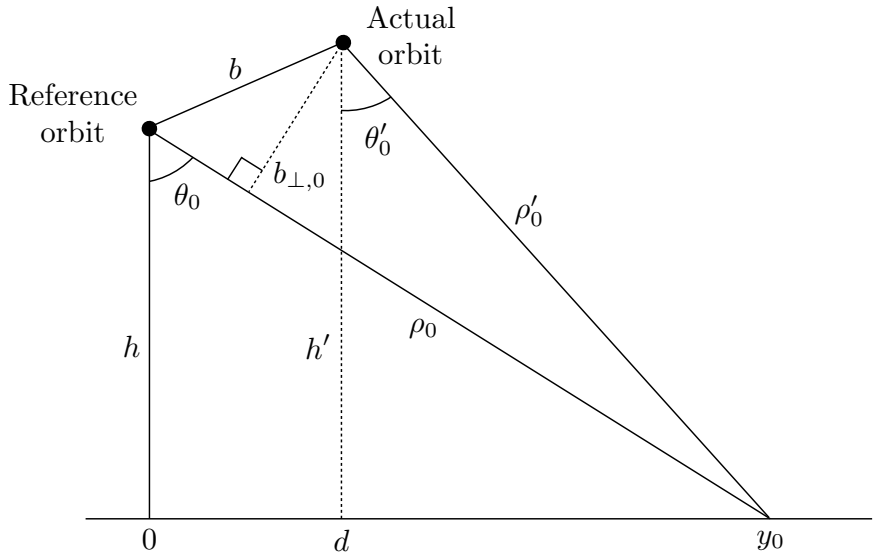


Figure 4.1: Flat-Earth model for the expansion of the motion compensation phase correction. Range-varying values with subscripts are evaluated at mid-range in the reference orbit.

From Equations 4.2 and 4.4, we see that the motion compensation phase consists of a linear term that is proportional to the perpendicular motion compensation baseline. Thus, the range spectral shift will increase with the distance between the actual and reference orbits. The second-order term $\phi_2$ relates to the quadratic variation, which gives the phase correction function a chirp-like characteristic. In particular, the instantaneous frequency will vary as a function of range, which will give rise to a spatially-dependent component of the spectral shift.

Using results from Prati and Rocca (1993), we write the spectrum of the resampled signal, Equation 3.33, as

$$X(f) \approx R\,(f + \Delta f_r)\, W(f), \tag{4.6}$$

where the ground reflectivity spectrum of the reference orbit $R(f)$ is shifted by $\Delta f_r$

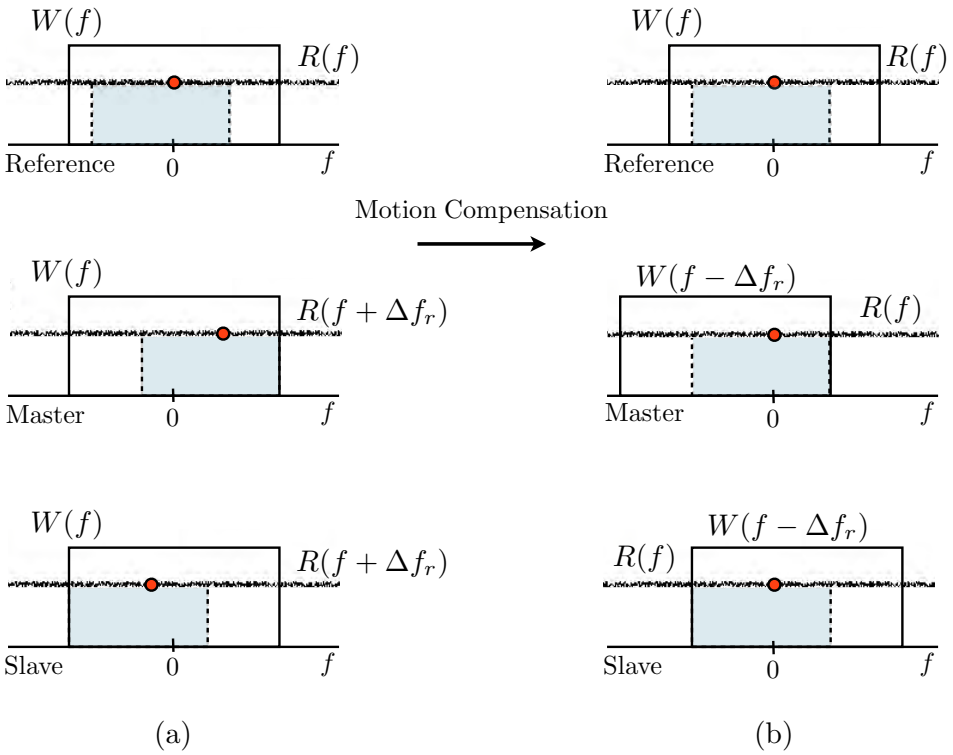


Figure 4.2: Spectral shifts of the ground reflectivity spectrum $R(f)$ and transmitted pulse spectrum $W(f)$ (a) before and (b) after motion compensation. The actual geometry varies in each acquisition, so master and slave scenes have different $\Delta f_r$ shifts. The red dot represents a point of comparison between the different geometries and the shaded regions show the common spectra bands.

and windowed by the transmitted pulse spectrum $W(f)$. $\Delta f_r$ is the constant, first-order shift from the SAR wavenumber analysis, which we can write as

$$\Delta f_r \approx -f_0 \frac{\Delta\theta_0}{\tan\theta_0}\,, \tag{4.7}$$

with $f_0 = c/\lambda$. Regardless of how the data are processed, the SAR wavenumber shift is related to the actual viewing geometries and will always be present. In addition, since $\Delta\theta_0$ will be different for master and slave acquisitions, the shift will vary for each scene. Figure 4.2a shows the spectrum for two acquisitions, compared to the reference geometry. In both cases, the pulse window is centered at zero frequency, with the ground reflectivity spectrum shifted relative to the reference.

Continuing with the first-order analysis, we ignore $\phi_2$ and calculate the instantaneous frequency of Equation 4.2 as

$$\Delta f_r \approx \frac{\lambda f_0}{4\pi}\frac{d\phi_m(u)}{du} \approx -f_0\frac{\Delta\theta_0}{\tan\theta_0} \approx -f_0\frac{b_{\perp,0}}{\rho_0'\tan\theta_0}\,. \tag{4.8}$$

Compared to the SAR wavenumber shift in Equation 4.7, these two terms are equivalent. Next, we write the Fourier transform of the motion compensated signal in Equation 3.36

$$X_m(f) \approx R\,(f)\,W(f-\Delta f_r). \tag{4.9}$$

We see that following motion compensation, the ground reflectivity spectrum is aligned with that of the reference orbit, but the pulse window is shifted to a carrier frequency of $\Delta f_r$. These results are unique to motion compensation, and unlike the standard wavenumber shift, yield a range carrier that must be accounted for during subsequent processing steps. An example is shown in Figure 4.2b, where the master and slave spectra are shifted by different amounts, but the ground reflectivity spectra are aligned with the reference after motion compensation.

Due to the second-order term in Equation 4.2, the spectral shift will vary as a function of range about the mid-swath value $\Delta f_r$. For airborne sensors, this variation is important, since the look angle changes significantly across the swath (Guillaso et al., 2006; Reigber, 1999). For spaceborne sensors, however, a constant, first-order approximation is sufficient. The first-order shift describes the average frequency of the range spectra and is adequate to define the center frequency of the bandpass filters in our InSAR processor. We use the constant approximation for common band filtering in Section 4.5.1 and consider the more accurate range-dependent case for spatial interpolation in Section 4.5.2.

## 4.4 Doppler Centroid Shift

During motion compensation, the velocities of the echoes are constrained to lie entirely in the along-track or $s$-direction. If the actual and reference trajectories are not parallel, the received signal will have velocities in the $c$ and $h$ directions, which leads

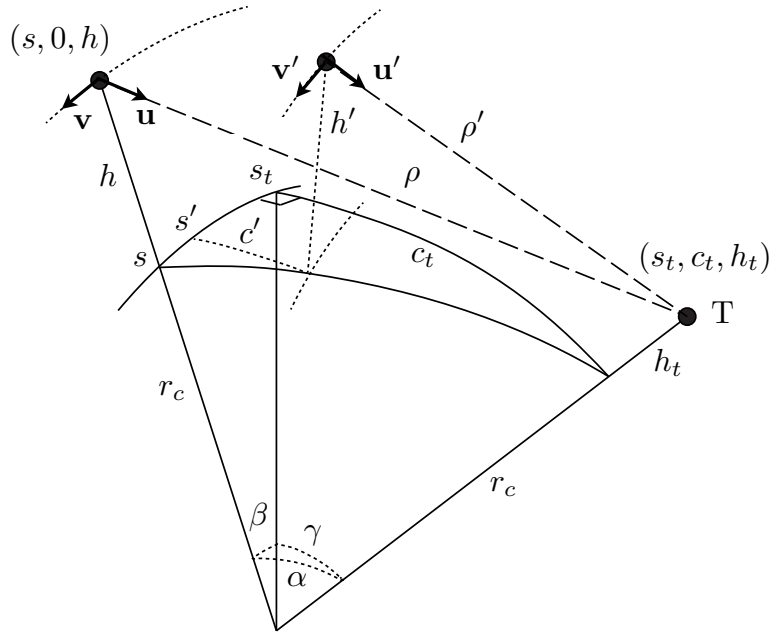


Figure 4.3: Motion compensation geometry relating the velocity and look vectors to the *sch* sphere. Position of the actual orbit is given in primed coordinates.

to a change in the squint angle and the Doppler centroid of the azimuth spectrum. If the Doppler centroid is estimated from the range-compressed data, then we need to update this value to match the new Doppler centroid before forming the azimuth reference function or interpolating during coregistration.

Figure 4.3 illustrates the geometry for a sensor at position $(s, 0, h)$ in the reference orbit imaging a target at position $(s_t, c_t, h_t)$. The reference velocity vector $\mathbf{v}$ is constrained to lie entirely in the along-track direction, such that $\mathbf{v} = [v_s, 0, 0]^T$. From the general definition, used in Kong et al. (2005), we write the Doppler centroid in the reference orbit as

$$f_d = -\frac{2}{\lambda} \langle \mathbf{v}, \mathbf{u} \rangle = -\frac{2}{\lambda} v_s u_s \,, \tag{4.10}$$

where the unit look vector $\mathbf{u} = [u_s, u_c, u_h]^T$ and $\langle \cdot \,, \cdot \rangle$ denotes the inner product.

We select the reference orbit to closely approximate the actual trajectory, however, deviations in the heading and nonzero motion compensation baselines will lead to differences between the velocities and look vectors. Using Equation 4.10, we represent

the actual orbit in a primed coordinate system and write the Doppler centroid as

$$\begin{aligned} f'_d &= -\frac{2}{\lambda}\langle \mathbf{v}', \mathbf{u}' \rangle \\ &= -\frac{2}{\lambda}\langle \mathbf{v}, \mathbf{u}' \rangle - \frac{2}{\lambda}\langle (\mathbf{v}' - \mathbf{v}), \mathbf{u}' \rangle \\ &= -\frac{2}{\lambda}\langle \mathbf{v}, \mathbf{u} \rangle - \frac{2}{\lambda}\langle \mathbf{v}, (\mathbf{u}' - \mathbf{u}) \rangle - \frac{2}{\lambda}\langle \Delta\mathbf{v}, \mathbf{u} \rangle - \frac{2}{\lambda}\langle \Delta\mathbf{v}, (\mathbf{u}' - \mathbf{u}) \rangle \\ &= f_d - \frac{2}{\lambda}\langle \Delta\mathbf{v}, \mathbf{u} \rangle - \frac{2}{\lambda}\langle \mathbf{v}, \Delta\mathbf{u} \rangle - \frac{2}{\lambda}\langle \Delta\mathbf{v}, \Delta\mathbf{u} \rangle \ . \end{aligned} \tag{4.11}$$

The expanded form of Equation 4.11 consists of four terms that depend on the velocities, the look vectors, and variation terms $\Delta\mathbf{u} = \mathbf{u}' - \mathbf{u}$ and $\Delta\mathbf{v} = \mathbf{v}' - \mathbf{v}$. From this equation, the relationship between the actual and reference Doppler centroid is hardly clear, but we can simplify this expression and show that the third and forth terms are negligible.

During motion compensation, we project the actual position onto the reference orbit (Figure 3.3) so that $\Delta\mathbf{u}$ is primarily in the $c$ and $h$ directions and $\Delta u_s \approx 0$. The motion compensation baseline will affect the magnitude of $\Delta u_s$, however, it will remain comparatively small when the squint angle is moderate. Letting $\Delta\mathbf{u} \approx [0, \Delta u_c, \Delta u_h]$, the look vector variation is nearly orthogonal to the reference velocity, thus we can ignore the third term. Furthermore, since the fourth term is the inner product of two variation terms, $\Delta\mathbf{v}$ and $\Delta\mathbf{u}$, and it can also be ignored. Simplifying Equation 4.11, we relate the Doppler centroid in the reference orbit to the actual orbit by

$$f_d \approx f'_d + \frac{2}{\lambda}\langle \Delta\mathbf{v}, \mathbf{u} \rangle = f'_d + \Delta f_d \, . \tag{4.12}$$

Referring to Figure 4.3, we ignore topography and write the look vector as

$$\mathbf{u} = [r_c \cos\gamma \sin\beta, r_c \sin\gamma, (r_c + h) - r_c \cos\alpha]^T \tag{4.13}$$

and the velocity variation as

$$\Delta\mathbf{v} = \mathbf{v}' - \mathbf{v} \approx [0, v'_c, v'_h]^T \ . \tag{4.14}$$

In Equation 4.14, we use the approximation of $\mathbf{v}' \approx [v_s, v_c', v_h']^T$, which comes from our choice of the reference orbit velocity to approximate the along-track component of the actual velocity. Finally, substituting into Equation 4.12, the spectral shift relating the Doppler centroid in the actual and reference orbits is

$$\Delta f_d = \frac{2}{\lambda \rho} \left\{ v_c' r_c \sin\gamma + v_h' \left[ (r_c + h) - r_c \cos\alpha \right] \right\} . \tag{4.15}$$

The Doppler centroid spectral shift depends on the actual $c$ and $h$ velocities, which means that the shift can be minimized by choosing a reference track that is parallel to the actual orbit. It also has a range dependence that is explicit in $1/\rho$ and implicit in $\gamma$ and $\alpha$. The Doppler centroids computed from the range-compressed data can be updated across the swath, although most satellite processors assume a constant, average value for Doppler. In this case, the spectral shift can be evaluated at the mid-range position, and used to update the scene-wide Doppler centroid.

## 4.5 Coherence Improvements

In this section, we develop modifications to the common band filters and interpolation kernels as methods of improving interferometric coherence in motion compensation processors. Our changes take into account the range and Doppler spectral shifts that are often ignored in processing to local, scene-dependent reference tracks. Our goal is to use the results of the previous sections to modify the standard equations so that coherence can be maintained, even with large motion compensation baselines that are commonly seen in processing to global reference orbits.

### 4.5.1 Common Band Filtering

Several authors have presented common band filtering as a means to increase coherence by removing uncommon spectral components (Gatelli et al., 1994; Guillaso et al., 2006; Reigber, 1999; Schwabisch & Geudtner, 1995). The general idea is that when we compute the interferometric phase, cross correlation of the spectra will introduce wideband noise if each contains different bands of the ground reflectivity spectrum.

The standard processing equations are all based on the assumption of a range signal centered at zero frequency and an azimuth signal centered at the original Doppler centroid. The following sections detail the changes in the filters needed to correctly process motion compensated data.

### Range Filtering

If we view the reference and actual orbits as master and slave geometries, Equation 4.6 describes the slave spectum in standard processing. Due to the wavenumber shift, the reflectivity spectrum of the slave is offset from the master by $\Delta f_r$, and since the pulse window is centered at zero frequency, different portions of the reflectivity spectrum will be observed in the two images. The common spectral components are retained by applying separate bandpass filters to the master and slave SLCs that define the regions of overlap. Figure 4.2a shows an example of disjoint common bands, as illustrated by the shaded regions. Gatelli et al. (1994) describe the bandwidths and center frequencies of the common band filters that they used to improve coherence in a standard InSAR processor.

In a motion compensation processor, each reflectivity spectrum is aligned, but the windowing functions are offset. This is shown in Equation 4.9, where $\Delta f_r$ is in the argument of $W(f)$. The master and slave are offset by different amounts, and the common spectral components are isolated by the overlap of the shifted windows. Figure 4.2b shows an example, where the common bands are truncated by the edges of window functions. Letting $\Delta f_{r,1}$ and $\Delta f_{r,2}$ be the motion compensation range spectral shifts for the master and slave scenes, we use a single filter for both SLCs to retain only the coherent parts of the spectra. With rect$(\cdot)$ representing a rectangle function and $B_W$, the bandwidth of $W(f)$, we define the bandpass filter by

$$\begin{aligned} H_r(f) &= \text{rect}\left(\frac{f - f_r}{B_r}\right) \\ f_r &= \left(\Delta f_{r,1} + \Delta f_{r,2}\right)/2 \\ B_r &= B_W - \left|\Delta f_{r,1} - \Delta f_{r,2}\right|. \end{aligned} \tag{4.16}$$

**Azimuth Filtering**

In contrast to range filtering, the azimuth spectra are aligned prior to motion compensation. As a result, standard azimuth filtering uses a single filter to remove the incoherent bands (Schwabisch & Geudtner, 1995). Following motion compensation, the master and slave Doppler spectra are shifted as shown in Equation 4.15. These shifts are a function of the reference geometry and the platform velocities in the actual orbit. Technically, the master and slave Doppler changes are different, but since we choose a reference orbit to approximate both orbits, and also since we process to the average Doppler centroid, we assume a common average shift. Letting $B_{a,p}$ define the processed azimuth bandwidth, we define the azimuth common band filter as

$$\begin{aligned} H_a(f) &= \text{rect}\left(\frac{f - f_a}{B_a}\right) \\ f_a &= \left(f_{d,1} + f_{d,2}\right)/2 \\ B_a &= B_{a,p} - \left|f'_{d,1} - f'_{d,2}\right|, \end{aligned} \tag{4.17}$$

## 4.5.2 Spatial-Domain Interpolation and Filtering

There are several interpolation steps that are often applied after motion compensation and before interferogram formation. For example, RCMC and coregistration are irregular interpolations implemented in the spatial-domain. In order to properly reconstruct the signal, the interpolation kernels must be shifted to account for either the range or azimuth carrier frequencies.

In the case of range, we can represent the carrier by the spatially-varying instantaneous frequency of $\phi_m(u)$. This can be computed numerically or directly from Equation 4.2

$$\Delta f_r(\rho) = \frac{\lambda f_0}{4\pi}\frac{d\phi_m(u)}{du} \approx f_0\left[\phi_1 + 2\phi_2\left(\rho - \rho_0\right)\right]. \tag{4.18}$$

Although the constant shift model in Equation 4.8 is accurate enough for spectral filtering of spaceborne data, it is straightforward to use a more precise, range-dependent carrier for spatial-domain interpolation. Given any spatial kernel $h(\nu)$, interpolating

a point at range $\rho$, we write the upconverted filter as

$$h_{r,m}(\nu) = h_r(\nu)\, e^{j4\pi\nu\Delta f_r(\rho)/(\lambda f_0)}. \tag{4.19}$$

In Equation 4.19, the filter is shifted to a locally constant carrier, defined by $\Delta f_r(\rho)$. For typical kernel lengths of eight or less range pixels, the locally constant assumption is valid, although the rate of the carrier change will scale with the bandwidth of the motion compensation phase correction function. Similar results apply to azimuth interpolation, where we use the Doppler centroid from Equation 4.12 to shift the kernel

$$h_{a,m}(s) = h_a(s)\, e^{j2\pi f_d s/v_s}. \tag{4.20}$$

## 4.6 Results

In order to test the effects of the motion compensation spectral shifts, we process an interferogram to both local and global average reference orbits and examine the coherence. The local reference track is defined by the average of the master and slave orbits, while the global reverence is the average over a set of orbits, used for time-series analysis. The global reference is representative of the processing in Chapters 6 and 7, where we want all interferograms produced in a common geometry. We find that the range spectral shift is substantially larger in the global orbit and that coherence is reduced across the entire scene. We also see that coherence is almost completely restored by using the techniques presented in the Section 4.5.

We choose fourteen ascending orbits from the ALOS PALSAR sensor, on track 287, frame 380, over Kilauea Volcano, Hawaii. These orbits span from May 5, 2006 to January 19, 2010 and are used in the vector time-series results of Chapter 7. Figure 4.4 shows the distribution of the mid-orbit locations, projected onto a local cartesian plane. The figure shows that the orbit positions drift over time, causing a large spread of the spatial baselines. JAXA periodically corrects the drift and adjusts the trajectory of ALOS, although this correct results in separate sets of clustered orbit positions. For example, orbits 1784 and 5139 are the oldest observations, occurring

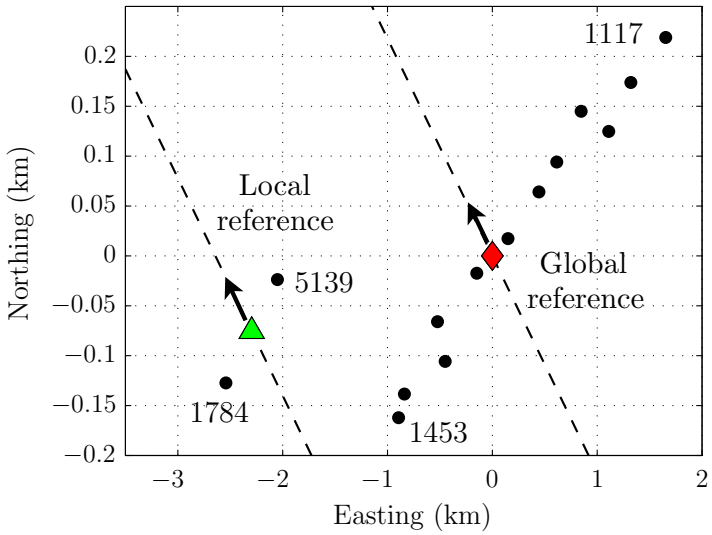


Figure 4.4: Black dots representing the ground projections of the center orbit positions for ascending ALOS data on track 287, frame 380, orbit numbers 1784, 5139, 5810, 9165, 0983, 1050, 1117, 1453, 1520, 1587, 1654, 1855, 2057, and 2124.

just before a correction, and their mid-orbit positions are clustered furthest from the other data.

To process orbits 1784 and 5139 to a common trajectory, we can minimize the motion compensation baseline and use their local average as the reference (Figure 4.4). Both SLCs will reside in a local coordinate frame, however, they will not be coregistered with the remaining data. If we use the global average as the common reference, all of the SLCs will be coregistered in the same coordinates, but since the positions of orbits 1784 and 5139 are outliers, they will be processed with larger motion compensation baselines that will introduce significant spectral shifts. This is also true for other orbits on the edges of the distribution. For example, orbits 1117 and 1453 will also have large spectral shifts.

Table 4.1 summarizes the geometric and spectral parameters that we compute for processing orbits 1784 and 5139 to both geometries. The local reference results in relatively small motion compensation baselines, on the order of 100 m, and spectral shifts of less than 1 MHz. Since these shifts are only one percent of the sampling frequency, the coherence loss from improper interpolation and filtering is minimal.

Table 4.1: Local and global motion compensation spectral shift parameters.

| | **Local Reference** | | **Global Reference** | |
|---|---|---|---|---|
| **Orbit #** | 1784 | 5139 | 1784 | 5139 |
| $\Delta\theta_0$ (deg) | -0.008 | -0.008 | -0.153 | -0.137 |
| $b_\perp$ (m) | -107 | 106 | -2023 | -1814 |
| $\Delta f_r$ (MHz) | 0.527 | -0.529 | 8.65 | 7.69 |
| $\Delta f_d$ (Hz) | 40 | 24 | 44 | 27 |

For the global reference, the baselines are an order of magnitude greater, which results in substantially larger spectral shifts. At shifts of one-quarter the sampling frequency, the interpolation and common band filters will retain incorrect portions of the spectra and reduce coherence. In both geometries, the Doppler centroid shifts were nearly identical and at only two percent of the pulse repetition frequency (PRF), and they will have little affect our our results. Small Doppler shifts are not guaranteed, but for this set of the orbits, the headings are all similar, so the cross-track velocities are minimal.

Figure 4.5 shows an example of the InSAR phase, where we processed the interferogram without accounting for the range spectral shift. Comparing figures from the local and global references, the global reference has higher phase noise and the fringes are less apparent. We also see the effects of increased noise in Figures 4.6a and 4.6b, where the scene-wide coherence is significantly less in the global reference interferogram. It is worth noting that in the local reference, there is a loss of coherence in the center of the image, which corresponds to a vegetated region. This loss is not a consequence of the spectral shifts, but it is due to decorrelation from the temporal baseline of 230 days. Furthermore, there is additional loss in coherence as the elevation rises towards the top of the image. This loss is a result of misalignment in the corgistration offset field, which we can corrected by using DEM-assisted registration (Nitti et al., 2011). These points aside, all of the highly coherent pixels are lost when using the global reference orbit, however, we would like to retain high-quality images, independent of the motion compensation baseline.

To restore coherence, we use the processor modifications presented in Section 4.5.

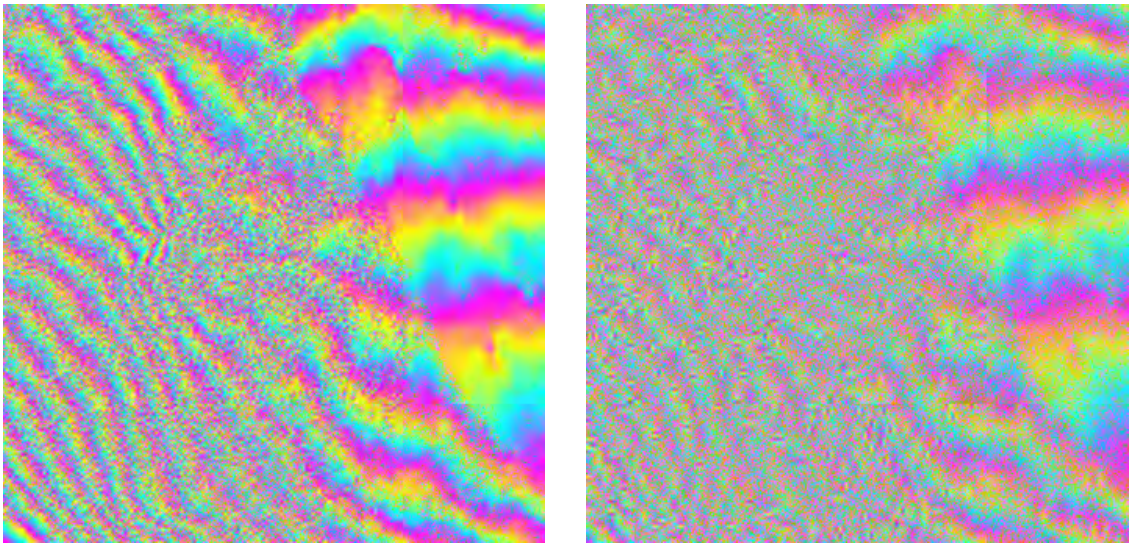

(a) (b)

Figure 4.5: Wrapped phase form interferograms processed to (a) local and (b) global reference orbits. Both examples ignore the motion compensation spectral shifts, leading to increased phase noise in the global image.

For common band filtering, we use a bandpass filter in range and azimuth to retain the aligned spectral components. These filters use the updated value of the Doppler centroid and the first-order range spectral shift from Equation 4.8. In addition, the slave SLC was originally sampled at half the range bandwidth ($f_s/2 = 16$ MHz), so we use the range shift to define bandpass filters for a Fourier domain upsampling by a factor of two. For RCMC, we use a one-dimensional sinc interpolation kernel in Equation 4.19 with the second-order shift in Equation 4.18. During coregistration, we shift a two-dimensional sinc kernel to the Doppler and range carriers, Equations 4.12 and 4.18, when we resample the slave to the master SLC. Both the RMCM and coregistration kernels use range-dependent carriers, which is possible since they are applied in the spatial domain.

Following these corrections, we find that coherence is almost completely restored to that of the local reference track. An example is shown in Figure 4.6c, where the coherence map is nearly identical to Figure 4.6a. There are some small unavoidable losses in using a global reference orbit, but these are due to approximations in the

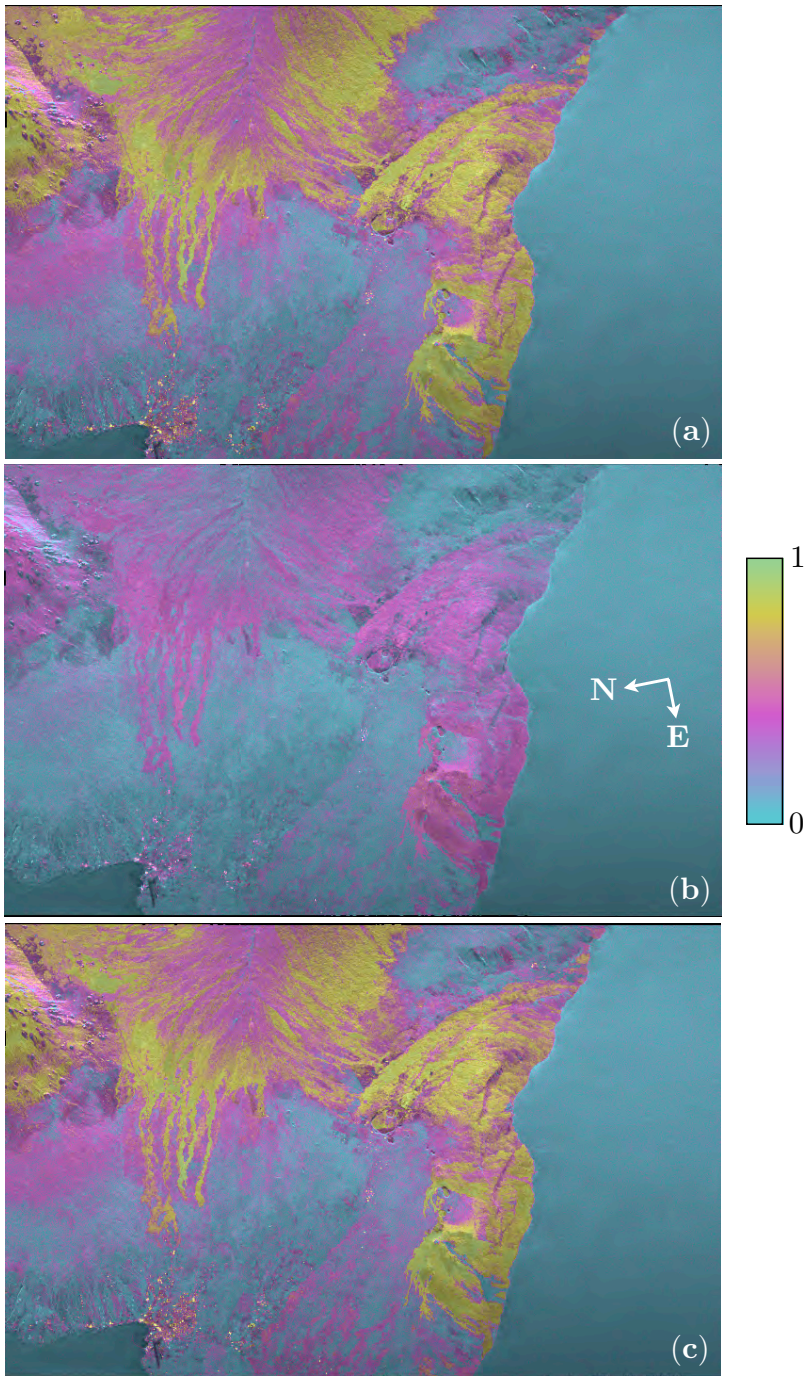


Figure 4.6: Coherence maps for an ALOS interferogram formed from orbits 1784 and 5139 on track 287 and frame 380. The interferogram was processed (a) to a local reference track, (b) to a global reference track, and (c) to a global reference track while taking into account the motion compensation range spectral shift.

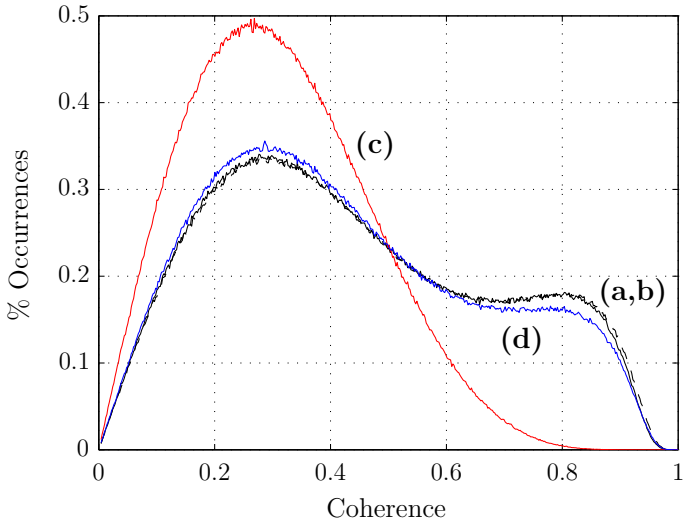


Figure 4.7: Coherence histograms of interferograms processed to local references (a) with and (b) without the spectral shifts and global references (d) with and (c) without the spectral shifts. (a) and (b) have almost identical coherence.

motion compensation processor that become less valid with increasing baseline. We further illustrate the improvements through the coherence histograms in Figure 4.7. The histograms show that since the spectral shifts were small in the local reference, their effects are negligible, and coherence was the same with and without accounting for the carriers in the processor. For the global reference, we initially lost all highly coherent pixels, but for the most part, these were restored after our proposed processor modifications. We attribute the slight losses to the truncated higher order terms in our expansion of the phase correction function and to approximations in the motion compensation processor that are less valid at large baselines.

## 4.7 Summary

Motion compensation of spaceborne radar images to non-local reference orbits induces shifts in the range and azimuth spectra. This phenomenon is similar to the SAR wavenumber shift, but has unique properties since motion compensation is applied after signal acquisition. The magnitudes of these shifts are directly related to the

degree of motion compensation and are typically negligible when processing to a local reference. For a global reference, such as those used in processing time-series data to a common orbit, the motion compensation baseline and resulting spectral shifts can be a large fraction of the sampling frequency. In this case, the interpolation and filtering kernels in an InSAR processor must be modified to account for range and azimuth carriers. Otherwise, motion compensation may result in a loss of coherence.

We developed the equations for the motion compensation spectral shifts and presented examples from data acquired by the ALOS PALSAR sensor. We processed an interferogram to both global and local reference orbits, and showed a loss in coherence when the motion compensation baseline was large and the spectral shifts were unaccounted for. Using modified equations for the common band filters and interpolation on a range-dependent carrier, we showed that image quality can be restored to that of a local reference orbit, even when the motion compensation baseline is large.

# Chapter 5

# Geolocation of Motion-Compensated Imagery

## 5.1 Introduction

Radar sensors acquire data in a slant-range imaging geometry, and as a result, there are inherent geometric distortions that must be corrected before observations can be combined with other geophysical measurements. Target locations are projected onto the radar's imaging plane, and topographic effects cause local geometric variations. We correct these distortions by geocoding, or resampling the InSAR imagery to an orthonormal map projection, which effectively rectifies the radar image. Once the measurements are geocoded, we can relate them to positions on the Earth's surface and incorporate them into other sets of geodetic data. Geolocation is particularly relevant to the vector time-series in Chapters 6 and 7, where we combine several radar geometries in a uniform WGS84 grid.

In this chapter, we present an efficient algorithm for the geolocation of InSAR imagery resulting from motion compensation processors. We outline the derivation using the spherical *sch* coordinate system from Chapter 3, although our approach may be readily applied to any processor in which the orbits are corrected and processed to a spherical reference track. Our algorithm calculates the transformation from DEM to radar coordinates, and uses the corresponding along-track and slant-range

position to interpolate the interferogram to the DEM. This approach has two primary benefits, in that number of computations is dictated solely by the desired resolution of the orthogonal map projection, and that the radar image is on a regular grid, which avoids the use of computationally intensive irregular interpolation algorithms. Furthermore, the simplicity of the resulting equations leads to a solution that is remarkably fast without sacrificing precision.

We develop our algorithm both for a constant Doppler centroid and for the more general case of range-varying Doppler. The constant Doppler formulation is representative of spaceborne geometries, and the range-varying case of airborne sensors, where the look angle changes significantly across the swath. We demonstrate spaceborne results from the ALOS PALSAR platform, validated against the corner reflectors at the Rosamond Calibration Array outside of Palmdale, California. Here we see ground projection errors with accuracy on the order of less than a radar pixel. For the varying Doppler centroid, the range-dependence has no simple functional form, so we replace the closed-form equations with an iterative solution. We illustrate these results using data collected by JPL's airborne UAVSAR sensor and validate our approach by registering the geolocated image to a DEM. We find convergence in no more than five iterations, with an accuracy that is similar to the closed-form solution.

## 5.2 Background

The general strategy for geolocation is to solve for the intersection of the radar look vector with the surface of the Earth. Typically, this is achieved by the simultaneous solution of the radar range equation, the Doppler equation, and the geometric position on some Earth model. Curlander et al. (1987) presented this approach using an ellipsoidal approximation to the Earth, where they start with the known orbital position of a radar pixel, and solve for the intersection with the ellipsoid. Wan et al. (2010) followed the same strategy, but with a more accurate extension that incorporated a DEM. In both approaches, the algorithms produce an image geodetic location map from radar coordinates to an arbitrary map projection. This mapping is then used to resample the InSAR image onto an orthonormal grid.

The intersection with the ellipsoid (or DEM) must be solved iteratively at each radar pixel, thus the transformation from radar to geodetic coordinates is computationally expensive. Furthermore, this transformation is not unique since multiple topographic points can lie at the same radar range. Since the mapping is not one-to-one, ambiguities can lead to residual geometric distortions. More importantly, the image geodetic location map is uniformly sampled in radar coordinates, but irregular in the geodetic domain. Therefore, resampling of the InSAR imagery to an orthonormal grid requires complicated irregular interpolation or some polynomial approximation to the inverse mapping from geodetic to radar coordinates (Curlander et al., 1987). The polynomial approximation reduces accuracy in regions with large topographic slopes and irregular interpolation produces artifacts in the geocoded image.

Meier et al. (1989) and Schreier et al. (1990) avoided several of these issues by solving directly for the unique inverse mapping, from a DEM pixel to radar coordinates. Starting from the orthonormal DEM grid avoids irregular interpolation, but is still slow as one needs to iteratively search the radar orbit to satisfy the range, Doppler, and ellipsoid equations. Arbitrary radar trajectories cannot be represented by a continuous mathematical functions, thus an iterative search is the only option to solve these equations.

Our approach is a new method for geolocation that exploits the well-known circular orbit of motion compensation processors, giving an exact set of equations relating the position in a DEM to the slant-range and along-track coordinates of the interferogram. Once we known the position in the radar image, we interpolate using standard two-dimensional kernels and produce an image on a uniform geodetic grid. Our approach is based on range-Doppler equations, similar to Meier et al. (1989), but in using a spherical coordinate system, we are able to develop exact expressions for the orbital position and slant-range. With a constant Doppler centroid, these equations have a simple closed-form solution. In the more general case of range-varying Doppler, the equations are solved iteratively, but convergence is rapid and does not depend on an exhaustive search of the orbit.

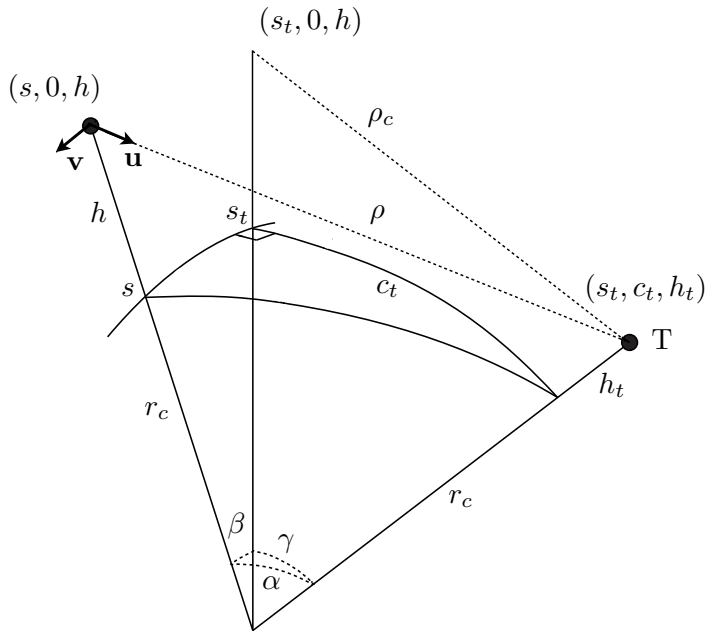


Figure 5.1: Motion compensation geometry relating platform and topographic positions to the *sch* sphere.

## 5.3 Geolocation in SCH Coordinates

The output of the InSAR processor from Chapter 3 is an interferogram with uniform $s$ and $\rho$ spacing, much like the along-track and slant-range coordinates of standard InSAR products. We start in the geodetic domain, traversing the orthonormal grid defined by the DEM, and solving for the inverse transformation to radar coordinates. Thus, we summarize the geolocation problem as: given the topographic position, solve for $s$ and $\rho$, and interpolate the corresponding amplitude and phase from the interferogram.

Shown in Figure 5.1, the *sch* position of the topographic point is $(s_t, c_t, h_t)$, which we calculate through affine transformations from the native DEM coordinates (Buckley, 2000). We also know the orbit height and radius of curvature, $h$ and $r_c$, which come from our definition of the reference track. Using the law of cosines, we write

$$\cos\beta\cos\gamma = \frac{(h+r_c)^2 + (h_t+r_c)^2 - \rho^2}{2(h+r_c)(h_t+r_c)}\,, \tag{5.1}$$

where we can calculate $\gamma = c_t/r_c$, but $\beta$ and $\rho$ are unknown. Our primary goal is to solve for $s$ and $\rho$, however, we choose to work with $\beta$ in the following derivation. This angle is easily related to the desired along-track position through

$$s = r_c \cdot \beta + s_t \, . \tag{5.2}$$

Establishing a second expression in $\rho$ and $\beta$, we refer to Equation 3.3 and write the Doppler centroid as

$$f_d(\rho) = -\frac{2}{\lambda}\dot{\rho} \, , \tag{5.3}$$

where $\dot{\rho}$ is the time derivative of range. From Equation 5.1, we write

$$\rho^2 = (h + r_c)^2 + (h_t + r_c)^2 - 2(h + r_c)(h_t + r_c)\cos\beta\cos\gamma \, , \tag{5.4}$$

and then taking the derivative,

$$\dot{\rho} = \frac{(h_t + r_c)(h + r_c) \cdot \dot{\beta}\sin\beta\cos\gamma}{\rho} \, . \tag{5.5}$$

Finally, noting the time-dependence on $\beta$, where $\beta = \frac{vt}{(h+r_c)}$ and $\dot{\beta} = \frac{v}{(h+r_c)}$, we express the range-dependent Doppler centroid as

$$f_d(\rho) = -\frac{2v}{\lambda\rho}(h_t + r_c)\cos\gamma\sin\beta \, . \tag{5.6}$$

From these equations, the position into the interferogram for deskewed or zero-Doppler geometries is trivial. Referring to Figure 5.1, in the absence of squint, $\beta = 0$, $\alpha = \gamma$, and $\rho = \rho_c$. Consequently,

$$\rho^2 = \rho_c^2 = (h + r_c)^2 + (h_t + r_c)^2 - 2(h + r_c)(h_t + r_c)\cos\gamma \tag{5.7}$$

and $s = s_t$. These quantities are all known, which allows us to interpolate the interferogram at $(s, \rho)$, giving the complex echo corresponding to the current position in the DEM.

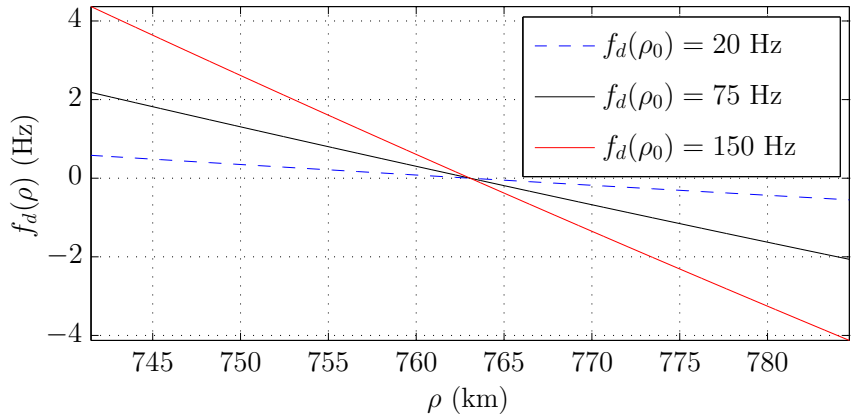


Figure 5.2: Doppler centroid variation relative to mid-range for a typical ALOS geometry with $\theta_0 = 21°$, $v = 7598$ m/s, $h = 696$ km, and $r_c = 6343$ km. Each curve represents a different Doppler centroid at the mid-range position $\rho_0$.

For squinted geometries, $f_d(\rho)$ is determined empirically from the data or theoretically from the sensor attitude parameters, however, its dependence on $\rho$ makes it difficult to solve Equations 5.1 and 5.6 simultaneously. Even if some functional form of $f_d(\rho)$ is assumed (i.e. linear or quadratic), no straightforward solution exists. In the subsequent sections we consider a closed-form solution, making a constant Doppler approximation, and an iterative solution, where Doppler varies arbitrarily with range.

### 5.3.1 Constant Doppler Centroid

Figure 5.2 shows example of the change in Doppler centroid for a typical ALOS geometry. We compute these curves using Equation 5.6 and normalize with respect to the mid-range value at $\rho_0$. For spaceborne sensors, there is a nearly linear relationship with range, where the change across the swath increases with the nominal Doppler centroid. Since the Doppler centroid is a measure of the squint angle, increasingly large squints result in a stronger dependence on range.

However, ALOS, like many other modern sensors, has an electronically steered beam that reduces the squint from broadside pointing. In these sensors, Doppler centroids of 150 Hz or more are considered large, so we expect the $f_d(\rho_0) = 150$ Hz

curve to be a limiting case. Furthermore, we see from Figure 5.2 that the range variation is only a few Hz, even at larger squints. This variation is well below the bounds of how accurately the Doppler centroid can be tracked, especially if derived from the data, so we assert that in many spaceborne applications, the Doppler centroid can be assumed constant.

Under the assumption that $f_d(\rho) \approx f_d$, we use Equation 5.6 and write

$$\rho \approx -\frac{2v}{\lambda f_d} \cdot (h_t + r_c) \cos\gamma \sin\beta \tag{5.8}$$

Substituting Equation 5.8 into Equation 5.4, we have a quadratic in $\cos\beta$ of the form

$$0 \approx a\cos^2\beta + b\cos\beta + c\,, \tag{5.9}$$

where $a$, $b$, and $c$ are known constants derived from the substitution

$$\begin{aligned} a &= \left(\frac{2v}{\lambda f_d}\right)^2 \frac{(h_t + r_c)\cos^2\gamma}{2(h + r_c)} \\ b &= -\cos\gamma \\ c &= \frac{(h + r_c)^2 + (h_t + r_c)^2}{2(h + r_c)(h_t + r_c)} - a\,. \end{aligned} \tag{5.10}$$

Equation 5.9 gives two solutions for $\cos\beta$, each of which is ambiguous in the sign of $\beta$. Therefore, there are a total of four candidate values of for the along-track angle. An example is shown in Figure 5.3, where the solutions to the quadratic equation, $\cos\beta_1$ and $\cos\beta_2$, corresponds to four possible values, $\pm\beta_1$ and $\pm\beta_2$. We must resolve the correct solution before calculating $\rho$.

We first discuss the selection of $\cos\beta_1$ versus $\cos\beta_2$. Given the coefficients in Equation 5.11, we can make some generalizations about their relative magnitudes based on plausible geometries for both spaceborne and airborne sensors. We note that $|b| \leq 1$ and $a \gg 1$, therefore $|b| \ll a$. Furthermore, the first term of $c$ is approximately equal to one, thus $c \approx -a$. With these observations, we approximate Equation 5.9 as

$$1 \approx \cos^2\beta\,, \tag{5.11}$$

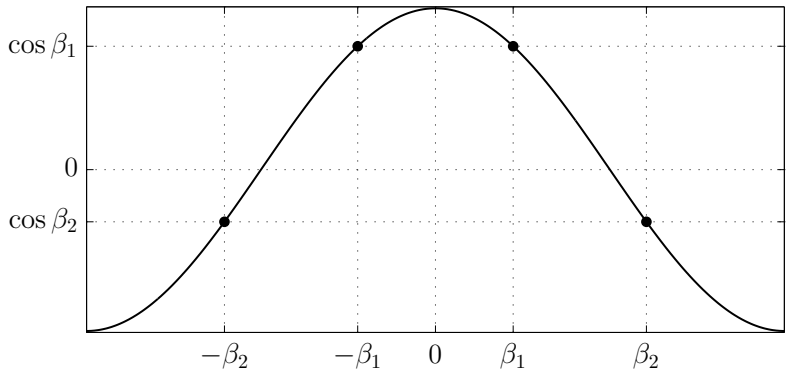


Figure 5.3: Example of the four possible solutions to a quadratic in $\cos\beta$.

which gives solutions of $\cos\beta \approx \pm 1$. Again from feasible imaging geometries, we know that $|\beta| \ll \pi/2$, thus we choose the single solution where $\cos\beta \geq 0$. Solving for the positive roots of the quadratic, we get

$$\cos\beta = \frac{-b + \sqrt{b^2 - 4ac}}{2a} \,. \tag{5.12}$$

After computing the inverse cosine in Equation 5.12, we can resolve the sign of $\beta$ through knowledge of the Doppler centroid. From Equation 5.2 and Figure 5.1, a backward squint corresponds to a positive along-track angle or $\beta \geq 0$. Therefore, the sign of $\beta$ is related to $f_d$ through

$$\mathrm{sgn}(f_d) = -\mathrm{sgn}(\beta) \,, \tag{5.13}$$

where sgn is the signum function. Finally, using Equations 5.12 and 5.13

$$\beta \approx -\mathrm{sgn}(f_d) \cdot \cos^{-1}\left(\frac{-b + \sqrt{b^2 - 4ac}}{2a}\right) \,. \tag{5.14}$$

Given the along-track angle, we calculate $(s, \rho)$ using Equations 5.2 and 5.4, and interpolate the interferogram for the echo corresponding to the current position in the DEM.

### 5.3.2 Range-Dependent Doppler Centroid

In many cases, particularly for airborne platforms, the assumption of constant Doppler is not valid. Figure 5.4a shows an example of Doppler variation derived from the attitude parameters of the airborne UAVSAR. Here we see changes in the Doppler centroid of up to 150 Hz, relative to mid-swath. In this case, using the approximation of $f_d(\rho) \approx f_d$ leads to large geolocation errors, especially in the near-range.

The difficulty in solving Equations 5.4 and 5.6 arises because the solution for $\rho$ depends on $f_d(\rho)$. The range-varying Doppler centroid is known empirically, but even if we approximate it by a polynomial, direct substitution into Equation 5.6 does not lead to a simple solution. We propose an iterative approach to simultaneously solve for $\beta$, $\rho$, and the corresponding $f_d(\rho)$, where the strategy is to update a constant $f_d$ on each iteration until the range-Doppler equations converge.

To initialize the algorithm, we let $\beta_0 = 0$ and evaluate Equation 5.7. This sets the initial range estimate to $\rho_0 = \rho_c$, which is the range of closest approach in Figure 5.1. This range is an underestimate of $\rho$, but it serves to select an initial guess for $f_d$. On the first iteration, we set $f_{d,1} = f_d(\rho_c)$, assume constant Doppler, and solve Equations 5.4 and 5.14. This yields an updated $(\beta_1, \rho_1)$ pair. On the second iteration, set $f_{d,2} = f_d(\rho_1)$ and repeat until convergence. In general, at the $i^{th}$ iteration

$$\begin{aligned} f_{d,i} &= f_d(\rho_{i-1}) \\ \beta_i &= -\mathrm{sgn}(f_{d,i}) \cdot \cos^{-1}\left(\frac{-b + \sqrt{b^2 - 4a_i c_i}}{2a_i}\right) \\ s_i &= \beta_i \cdot r_c + s_t \\ \rho_i^2 &= (h + r_c)^2 + (h_t + r_c)^2 \\ &\quad -2(h + r_c)(h_t + r_c)\cos\beta_i \cos\gamma \,. \end{aligned} \tag{5.15}$$

We also note that the coefficients, $a_i$ and $c_i$, are functions of $f_{d,i}$ as given in Equation 5.11. These equations are simple and therefore require very few resources to solve. We see in Section 5.4 that the initial estimate of Doppler is typically within a few Hz of the actual value, giving rapid convergence in only a few iterations.

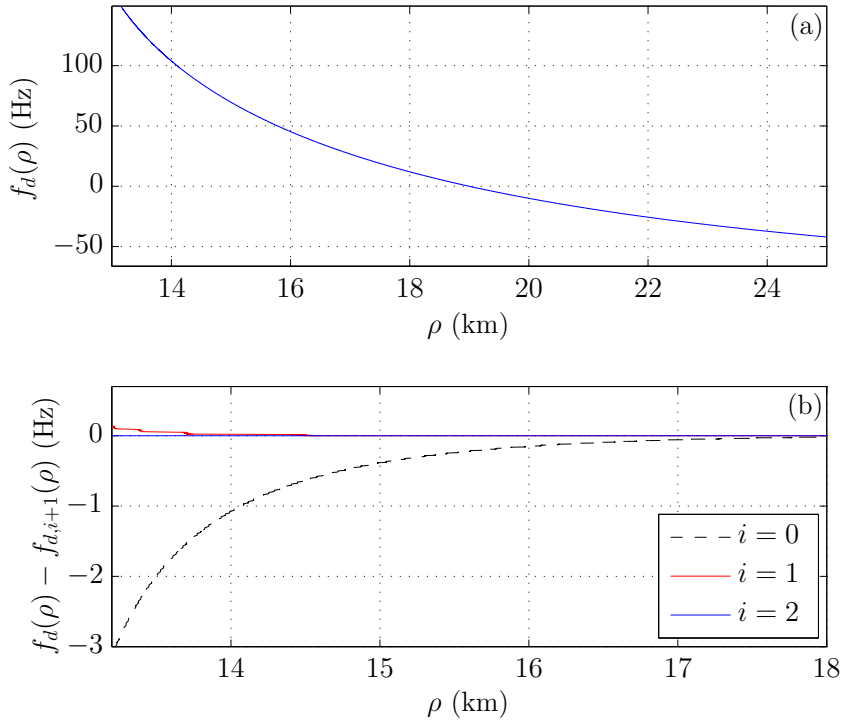


Figure 5.4: (a) Range-dependent Doppler centroid computed from UAVSAR sensor attitude angles. Values are normalized relative to mid-range. (b) Error for the first three iterations of the Doppler centroid estimate. Convergence is achieved on the third iteration, where $f_{d,3}(\rho) \approx f_d(\rho)$.

## 5.4 Experimental Results and Validation

We first assess the geodetic accuracy of our algorithm by processing a SAR image that contains known survey markers. Twenty-three corner reflectors were installed in the Rosamond dry lake bed outside of Palmdale, California by investigators at JPL, California Institute of Technology, Pasadena, California (Moller et al., 2001). Thirteen of these were aligned to return echoes in the direction of the ALOS satellite on its orbit track 216 in frame 680, which is an ascending orbit. We processed a SAR scene on this track from orbit 21081, acquired on January 8, 2010. The SAR image is shown in Figure 5.5, where the multilooked SLC is geocoded to a 15 m pixel spacing. The figure shows a close-up of the calibration array, where corner reflectors $\mathrm{CR}_0$ and

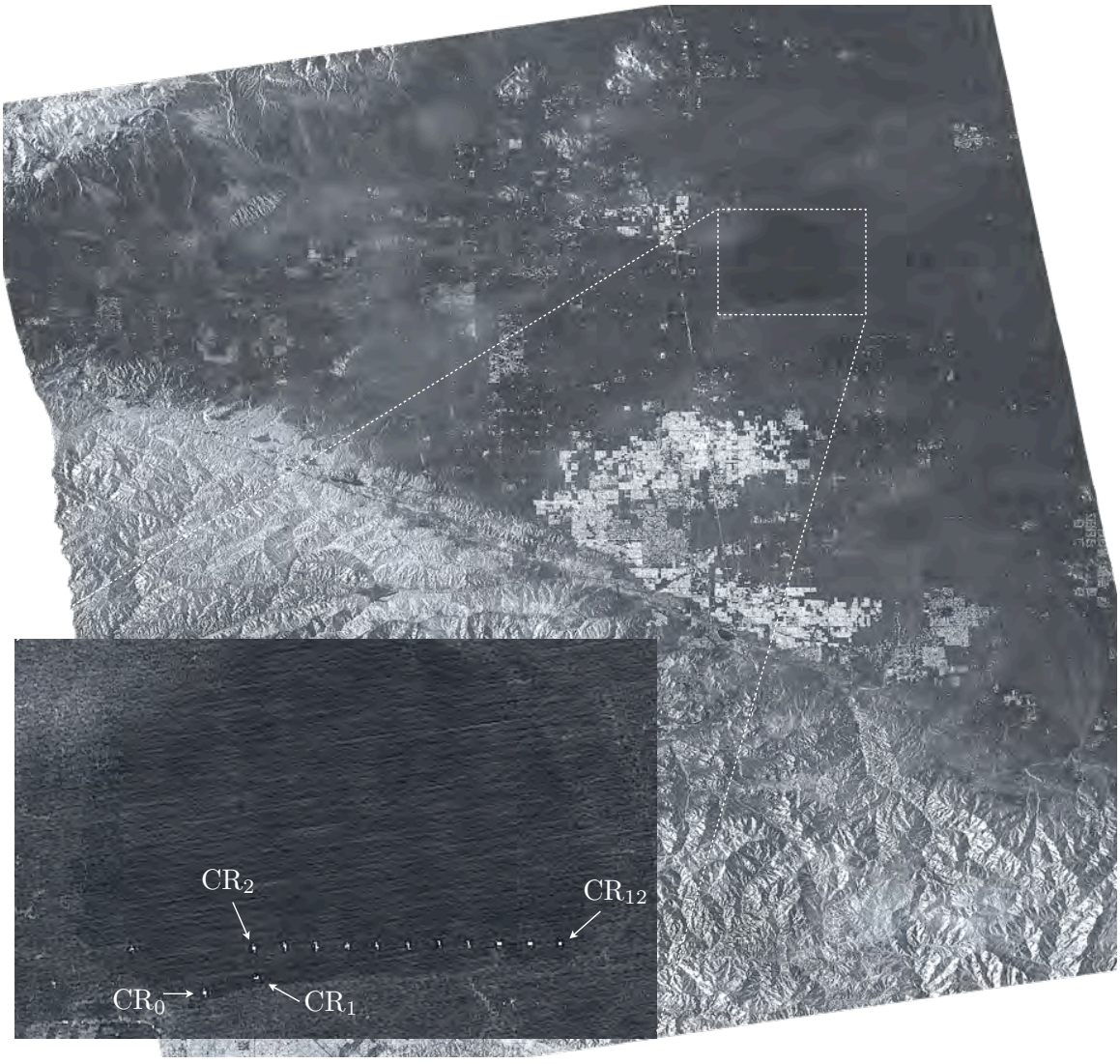


Figure 5.5: Geocoded ALOS SAR image from track 216, frame 680, orbit 21081, illustrating returns from the Rosamond Calibration Array outside of Palmdale, California. Corner reflectors $CR_0$ through $CR_{12}$ are oriented for ascending tracks.

Table 5.1: Geolocation results of an ALOS interferogram at the Rosamond Calibration Array.

| | GPS Position (deg) | | InSAR Position (deg) | | Ground Position Error (m) | |
|---|---|---|---|---|---|---|
| Corner Reflector | Latitude | Longitude | Latitude | Longitude | Latitude | Longitude |
| 0 | 34.79697 | -118.09653 | 34.79708 | -118.09639 | -12.83922 | -15.25182 |
| 1 | 34.79976 | -118.08705 | 34.79972 | -118.08694 | 4.47331 | -11.44963 |
| 2 | 34.80524 | -118.08746 | 34.80528 | -118.08750 | -4.59428 | 4.86487 |
| 3 | 34.80534 | -118.08191 | 34.80542 | -118.08181 | -8.35787 | -11.23689 |
| 4 | 34.80542 | -118.07637 | 34.80542 | -118.07625 | -0.16364 | -13.74776 |
| 5 | 34.80550 | -118.07074 | 34.80556 | -118.07069 | -6.23488 | -5.39384 |
| 6 | 34.80558 | -118.06522 | 34.80556 | -118.06514 | 3.17050 | -9.21830 |
| 7 | 34.80567 | -118.05966 | 34.80569 | -118.05958 | -2.85621 | -8.70127 |
| 8 | 34.80575 | -118.05407 | 34.80583 | -118.05403 | -9.16011 | -4.51071 |
| 9 | 34.80581 | -118.04891 | 34.80583 | -118.04889 | -2.18706 | -2.59477 |
| 10 | 34.80592 | -118.04336 | 34.80583 | -118.04333 | 10.18276 | -3.28000 |
| 11 | 34.80602 | -118.03769 | 34.80597 | -118.03764 | 5.70896 | -5.74511 |
| 12 | 34.80605 | -118.03228 | 34.80611 | -118.03222 | -7.20287 | -6.13102 |
| Mean Value | | | | | -2.31235 | -7.10740 |

$CR_1$ are at the edge of the lake bed, and $CR_2$ through $CR_{12}$ are positioned along a horizontal line, at a spacing of 500 m.

For all of these reflectors, we measured the inferred location from the SAR image and compared the results to a GPS ground survey done by scientists at JPL. In Table 5.1, we summarize our corner reflector location measurements from the ALOS data and from the JPL ground survey (`http://uavsar.jpl.nasa.gov/rosamond.html`). The maximum disagreement is on the order of 15 m, which is roughly the size of a multilooked ALOS pixel. Mean errors, however, are much lower, with magnitudes of 2 m in latitude and 7 m in longitude. These results use the constant $f_d$ assumption of Section 5.3.1, where this particular scene has a mid-swath Doppler centroid of $f_d(\rho_0) = 83$ Hz.

To validate the results of the iterative algorithm, we geocode an interferogram from the airborne UAVSAR sensor, which is expected to have significant Doppler centroid variation with range. The test interferogram was acquired over the Hayward Fault, near Oakland, California on the dates of November 17, 2009 and March 1, 2010. To motivate the use of our iterative algorithm, Figure 5.6a shows an example of the interferogram geolocated using a constant Doppler centroid that is fixed to

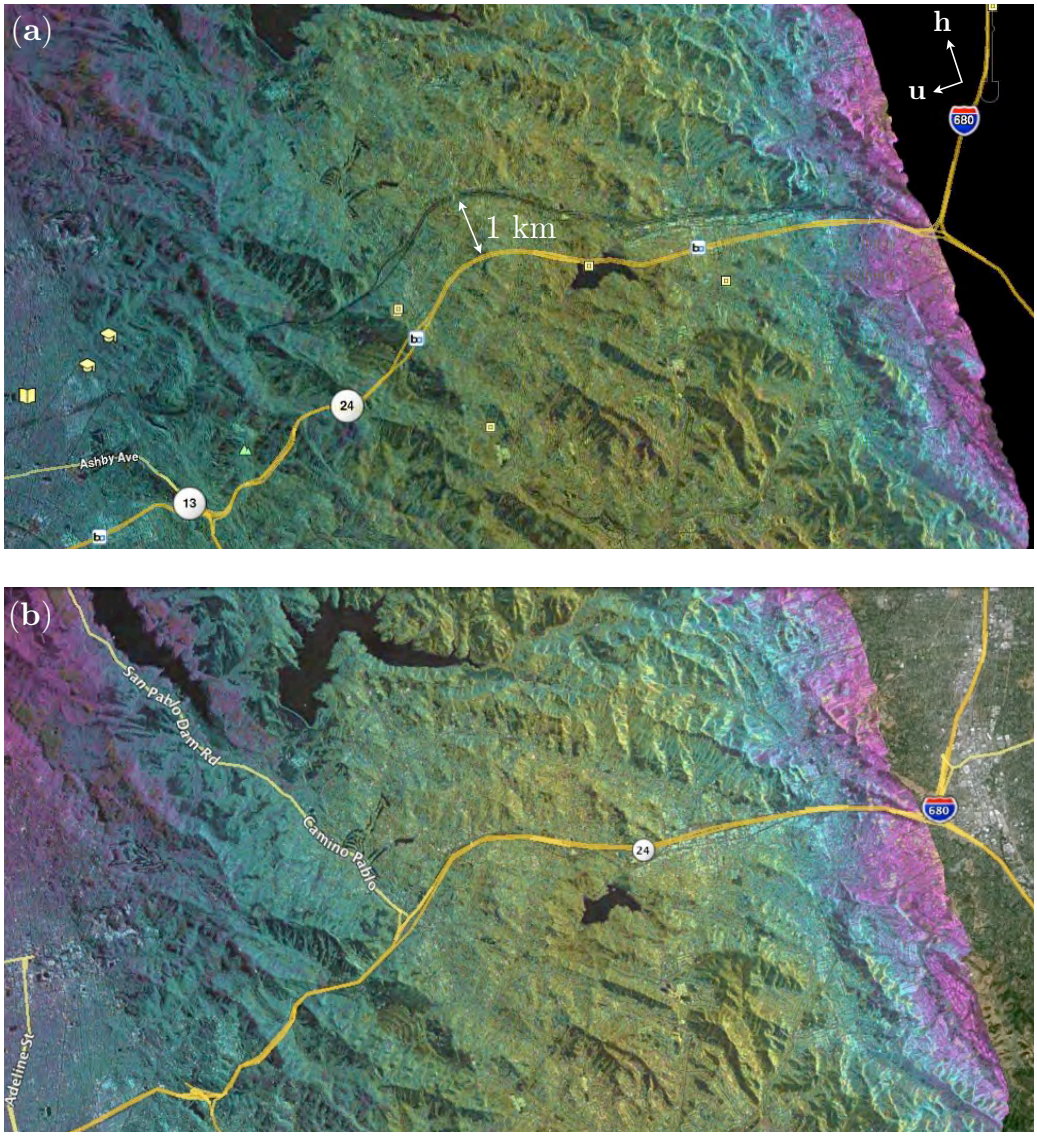


Figure 5.6: Geocode UAVSAR interferogram near Hayward, California, processed (a) with a constant Doppler centroid, fixed at the near-range value, and (b) with a range-varying Doppler centroid that converged in three iterations. Roads are overlaid to show geolocation accuracy. Heading and look vectors are denoted by **h** and **u**, respectively.

the near-range value. We show the range-Doppler curve in Figure 5.4a, and since it varies significantly across the swath, we see an increasing offset with range in the geocoded image. For example, using the overlaid features as a point of reference, the alignment is good in the near-range, but location errors increase to nearly 1 km at mid-range. For this airborne data, the constant Doppler centroid approximation in Equation 5.6 results in an incorrect along-track angle as the true Doppler deviates from the near-range value, therefore we must use the iterative approach for accurate results.

We only know the range-Doppler curve numerically, so the algorithm in Section 5.3.2 traverses the curve, updating estimates for $\rho$, $\beta$, and $f_d$, until the equations are mutually satisfied. When the pairs of $\rho$ and $f_d$ match the range-Doppler curve, the algorithm has converged. Figure 5.4b shows the error in the range-Doppler curve at each iteration. We use the range of closest approach to estimate an initial Doppler centroid, and this approximation selects the correct Doppler to within a few Hz. As seen in the figure, the initial estimate of the range-Doppler curve has the largest error in the near-range, however, it is only off by $\approx$ 3 Hz. The error will always be greatest in the near-range, where the rate of Doppler change is the greatest. On the first iteration, the max error is well below one hertz, and by the second we see convergence. The improved results are shown in Figure 5.6b, where the amplitude of the geocoded interferogram aligns well with the overlaid features.

For a more accurate assessment of the results, we examine the image registration shift needed to align the geocoded interferogram in Figure 5.6 with an SRTM DEM. In this example, the interferogram is geocoded to 6 m posting, and the one arcsecond DEM has a resolution of 30 m. Figure 5.7 shows the one-dimensional fits to the offsets in latitude and longitude, which are required to align the image with the DEM. We see mean offsets of 4.5 m in latitude and -3.7 in longitude, as well as an additional stretch, of magnitude less than 10 m in both dimensions. The offsets increase with longitude, which corresponds to near-range in the ascending, left-looking UAVSAR interferogram (Figure 5.6a). The Doppler centroid rate of change is highest in the near-range, so we expect this region to be the most sensitive to errors. In particular, we used the sensor attitudes to derive the range-Doppler curve, therefore errors in

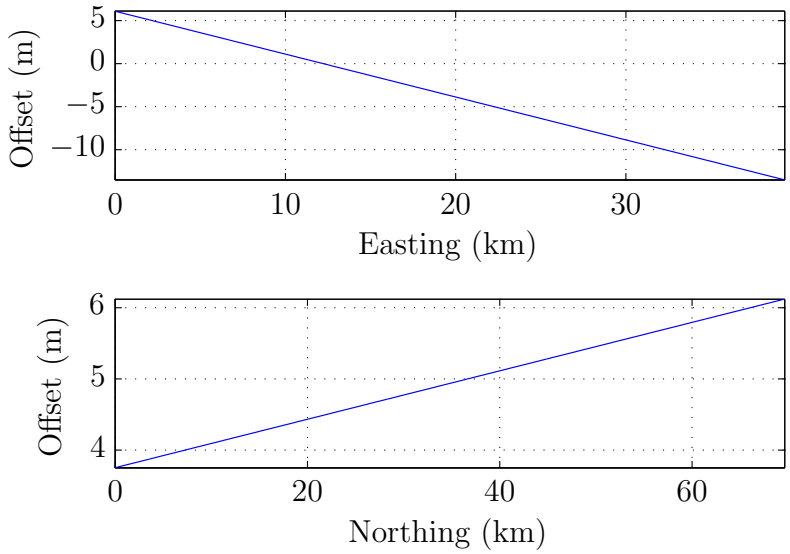


Figure 5.7: One-dimensional linear fits to the coregistration offsets between an SRTM DEM and a geolocated UAVSAR interferogram over the Hayward Fault near Oakland California. Longitude and latitude offsets are plotted in meters as easting and northing distances in a local ground plane.

the inertial measurement unit (IMU) angles could account for these near-range registration offsets. Furthermore, our approach does not account for atmospheric delays, which can contribute several meters of additional positioning error (Schubert et al., 2010).

## 5.5 Summary

Motion compensation processing is unique in that the orbits are corrected to lie on a well defined and circular reference track. Through this idealized orbit and use of the spherical *sch* coordinate system, many of the complications associated with past geolocation approaches are circumvented. We have developed an algorithm that exploits this geometry for simple and accurate geolocation.

We used the range-Doppler equations for a platform in a circular orbit to solve for the slant-range and along-track positions in the motion compensation interferogram. We do this by starting at the known *sch* location of a DEM pixel on an

orthonormal geodetic grid, and with knowledge of the Doppler centroid, we solve for the intersection of the look-vector with the orbit. Given the precise coordinates in the interferogram, we interpolate and place the complex echo on the geodetic grid. When the Doppler centroid is slowly varying, as is common in many satellite applications, this solution can be expressed by a simple set of close-form equations. If the Doppler centroid varies significantly with range, then the solution is iterative. However, the iterations are based on the same simple equations and convergence is very fast.

We have processed an example radar image from data acquired by the ALOS PALSAR radar satellite. We first assessed the geodetic accuracy by comparing the observed locations of a set of radar corner reflectors located in the Rosamond dry lake bed in California. Corner reflector positions were accurate at the 3 - 15 m level in our image, with typical errors closer to 5 m. We have also processed a UAVSAR interferogram from the Hayward Fault in California and calculated the image location error by coregistering the image with a DEM. Similarly, this image showed 10 m level errors in position, with average errors around 6 m. We also found that the images had to be stretched so that all points in the radar scene matched the locations in the elevation model data. We speculate that these offsets may be due to IMU attitude errors or unmodeled ionospheric and tropospheric effects. Nonetheless, the data products are sufficiently accurate for many geophysical surface studies.

As the accuracy of orbit trajectories improves, motion compensation processing is becoming more common for both spaceborne and airborne data sets. Our algorithm illustrates yet another advantage of motion compensation processing and has shown that the simplified geometry results in a fast and straightforward solution to the previously complicated problem of geolocation.

# Chapter 6

# Vector Deformation Time-Series

## 6.1 Introduction

The InSAR technique described in Chapter 3 is an effective means for the analysis of deformation at the surface of the Earth. InSAR exploits the phase difference between complex radar echoes, recording the slant-range change in the direction from the target to the sensor. These observations are sensitive only to motions in the direction towards the radar, therefore InSAR is inherently one-dimensional, measuring the surface change projected onto the radar's line of sight (LOS). Using observations before and after an event, InSAR resolves the displacement between two points in time, and has been widely used in the study of crustal deformation, ice motion and structure, hydrologic modeling, vegetation canopy characterization, and the generation of topographic data (Massonnet et al., 1993; Zebker & Rosen, 1994; Amelung et al., 2000; Weber & Zebker, 2000; Jónsson et al., 2002).

Because of the one-dimensional nature of LOS observations and the limited temporal resolution of a single interferometric pair, standard InSAR only measures a subset of the available data from deformation events. Chapter 2 outlined some extensions to InSAR that aim overcome these limitations: along-track interferometry, which increases dimensionality by measuring in a direction orthogonal to the radar LOS, and time-series analysis, which combines several InSAR measurements to improve the

temporal resolution. Although these approaches extend the utility of InSAR, the current research has yet to fully integrate these techniques to maximize the capabilities of InSAR sensors.

In this chapter we present a new approach that combines along-track interferometry and time-series analysis to estimate three-dimensional vector deformation time-series. Our approach extends an existing time-series technique, known as the Small Baseline Subset (SBAS) algorithm (Berardino et al., 2002), to incorporate measurements from multiple LOS-InSAR geometries, as well as along-track interferograms. Our algorithm is general, but we focus on multi-aperture interferometry (MAI) for along-track measurements (Bechor & Zebker, 2006), which we choose for its efficiency in computing large sets of interferograms. Our vector time-series resolve deformation in the east, north, and up (ENU) directions, and generally increases both the dimensionality and temporal resolution compared to methods using only a single imaging geometry.

The MAI data are relatively noisy, with low coherence and large measurement errors, so we also introduce the constraint of space-time separability to our time-series estimates. We show that this constraint is equivalent to the assumption of a constant direction of deformation, which we enforce by restricting the relative displacements between the ENU components. We present equations justifying the use of separability through a principal component analysis (PCA) of existing geodetic data and discuss methods of solving the resulting system of equations. We show that the constraints lead to nonlinearity in the equations, and further present a computationally efficient linear alternative that applies separability only to the northern component. MAI primarily defines this directional component, and due to its increased level of error, measurement of the north directional deformation benefits the most from additional constraints.

This chapter is organized as follows. Section 6.2 gives a background of SBAS and existing approaches to multidimensional InSAR. Section 6.3 describes the LOS and along-track measurements from a single interferometric pair and discusses the noise characteristics of MAI and InSAR. Section 6.4 reviews the traditional, SBAS equations and presents our vector algorithm, which we refer to as V-SBAS. Section

6.5 presents space-time separability and shows how it can be demonstrated through PCA. Finally, Section 6.6 describes the linear approach to re-estimate the northing time-series with separability constraints. Our algorithm is verified with results at Kilauea Volcano, Hawaii in Chapter 7.

## 6.2 Background

InSAR can be extended to time-series analysis by combining several repeat passes and estimating the relative displacement between each acquisition. We achieve this in the SBAS algorithm by forming a system of equations from a set of differential phases and solving for the best fit time-series through a least-squares minimization. The measurements come from a collection of SAR scenes, where we process all possible interferometric pairs that meet limits on the temporal and spatial baselines. We set baseline thresholds to reduce the effects of interferometric decorrelation, which results in subsets of all possible InSAR pairs. At pixels maintaining coherence across the temporal set of measurements, we use the differential phases to estimate a time-series that defines the relative displacement at each epoch. SBAS has become a common tool for monitoring deformation (Pepe et al., 2005; Agram et al., 2013; Baker & Amelung, 2012; Berardino et al., July; Reeves et al., 2011; Tizzani et al., 2007; Lanari et al., 2007), and in addition to providing multi-temporal analysis, it reduces the effects of measurement errors by exploiting redundancy in the observations (Aster et al., 2005).

SBAS provides spatially dense measurements at an increased temporal resolution, however, it suffers from the same LOS limitations as conventional InSAR. Specifically, SBAS time-series are one-dimensional and for current spaceborne satellite platforms, SBAS is also rather insensitive to northward deformation. We discuss the missing InSAR component in Section 2.5.1, which reveals that SBAS from any satellite geometry can only resolve deformation primarily in the east and up directions. This limitation is not only problematic for sources causing significant northward deformation, but also for constraining source parameter estimations in geophysical inverse problems. To better characterize the deformation field and ultimately the source, we need to combine SBAS with multidimensional techniques.

Multidimensional InSAR combines observations from several LOS geometries in an effort to increase the dimensionality of deformation measurements. Past studies have attempted to use InSAR from both ascending and descending headings to resolve three-dimensional vector fields (Wright et al., 2004; Ng et al., 2012, 2011). These findings indicate that InSAR alone is not sufficient to accurately constrain the northward component and that other geodetic measurements are necessary. A common approach to resolving the missing component is the use of along-track interferometry, which senses deformation in the heading direction of the sensor. For polar orbits, the heading is essentially in the north-south direction, and by including ascending and descending LOS observations, we can estimate three-dimensional deformation fields.

We discuss the techniques of azimuth offsets (AZO) and MAI in Section 2.5.2 as approaches for along-track interferometry. Several authors have used AZO, combined with ascending and descending LOS-InSAR, to estimate vector deformation fields (Sandwell et al., 2008; Fialko et al., 2005, 2001). These studies have been successful in resolving all three components, however, this approach is best suited for large deformation, as the accuracy is typically on the order of 15 cm (Casu et al., 2011). MAI is an newer alternative that offers faster processing and lower measurement errors, however, the MAI phase uncertainty is still on the order of 8-10 cm. Like AZO, multidimensional MAI studies typically focus on events with large deformation, and restrict analysis to highly correlated interferograms (Jung et al., 2011; Barbot et al., 2008; Sun et al., 2004; Erten et al., 2010; Gourmelen et al., 2011; Jónsson, 2012; Hu et al., 2012). Along-track techniques reveal the missing component of InSAR, but they are the limiting factor in the accuracy of multidimensional analysis.

In this chapter, we integrate multidimensional InSAR with time-series by combining multiple LOS geometries and MAI. Other efforts have been made to incorporate along-track techniques with SBAS, but none of these has simultaneously estimated the full three-dimensional and time-dependent deformation field. Casu et al. (2011) and Zhao et al. (2013) used AZO in conjunction with LOS observations to estimate two-dimensional time-series in the slant-range and along-track directions. McMillan et al. (2012) used MAI and LOS-InSAR to calculate two-dimensional velocity maps,

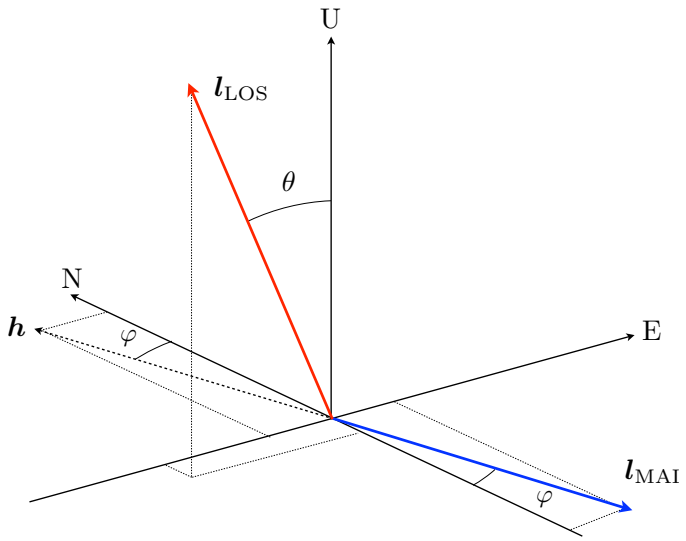


Figure 6.1: Look vectors in local coordinate frame for LOS-InSAR ($\boldsymbol{l}_{\mathrm{LOS}}$) and MAI ($\boldsymbol{l}_{\mathrm{MAI}}$). Heading is denoted by $\boldsymbol{h}$ and look direction is from the target to the sensor.

although their approach used stacking, rather than SBAS. While the current literature mainly focuses on vector deformation between two points in time or time-series in the LOS direction, we develop the equations to merge multi-temporal and multi-dimensional analysis. By incorporating observations from multiple geometries, our goal is to increase the dimensionality of the time-series and reduce the effects of noisy along-track data so that vector time-series can be estimated in regions with relatively low deformation signatures.

## 6.3 2D Measurements from a Single InSAR Pair

LOS and MAI interferograms are processed from the same set of SLCs, therefore a single pair of SAR scenes yields phase observations projected onto two distinct look vectors: one in the direction towards the radar and another along-track. Figure 6.1 illustrates these look vectors in a local cartesian frame, where we represent each as a

function of the look angle $\theta$ and the sensor heading $\varphi$

$$\boldsymbol{l}^T = \begin{cases} [-\sin\theta \cdot \cos\varphi, \sin\theta \cdot \sin\varphi, \cos\theta]^T & , \text{ LOS} \\ [-\sin\varphi, -\cos\varphi, 0]^T & , \text{ MAI} \end{cases} \tag{6.1}$$

The LOS and along-track measurements are both derived from interferometric techniques, with the former from traditional InSAR and the latter from MAI. For brevity, we exclude the distinctions of LOS or traditional, and refer to the these observations as simply InSAR and the along-track measurements as MAI.

The observed deformation is the projection of the three-dimensional displacement onto each of the look vectors. In a polar orbit, the heading angle is nearly due north and InSAR is primarily sensitive to deformation in the east-west and up-down directions. This is true of all polar InSAR geometries, even those with varying look angles. On the other hand, the MAI observations are nearly orthogonal to the LOS, so they are most sensitive to deformation in the north-south direction.

Although MAI and InSAR are both interferometric techniques, they are processed differently, such that the displacement-to-phase relationships are unique. From Equation 2.1, the InSAR phase along the vector $\boldsymbol{l}_{\text{LOS}}$ is proportional to the LOS change in range $\Delta\rho$ as

$$\phi_{\text{InSAR}} = -\frac{4\pi}{\lambda}\Delta\rho\,. \tag{6.2}$$

From Equation 2.5, the phase along $\boldsymbol{l}_{\text{MAI}}$ is proportional to the along-track displacement $\Delta x$ as

$$\phi_{\text{MAI}} = -\frac{4\pi}{l} n\ \Delta x\,. \tag{6.3}$$

Unlike InSAR, the MAI phase is a function of the antenna length $l$ and the normalized subaperture squint $n$ (Bechor, 2006). The parameter $n$ indicates the degree of aperture splitting and is the foundation for the tradeoff between MAI phase error and deformation sensitivity. Aperture splitting allows MAI to measure along-track deformation, but it is also the underlying reason why MAI measurements have higher phase errors than InSAR.

### 6.3.1 MAI Phase Errors and Sensitivity

To compare the MAI and InSAR phase statistics, we use the maximum-likelihood estimator from Rodriguez and Martin (1992) and write the InSAR phase uncertainty as

$$\sigma_{\phi,\mathrm{InSAR}} \approx \frac{1}{\sqrt{2N_L}} \frac{\sqrt{1-\gamma^2}}{\gamma} \,, \tag{6.4}$$

where $N_L$ represents the effective number of looks, and the total correlation $\gamma$ is defined by Zebker and Villasenor (1992) as

$$\gamma = \frac{\left|\gamma_{\mathrm{spatial,temporal}}\right|}{1 + \mathrm{SNR}^{-1}} \,. \tag{6.5}$$

For MAI, we can use the same relationships, but we must take into account the various stages of processing in Figure 2.13. Both the forward and backward interferograms have independent phase variances of

$$\sigma_\phi^2 = \frac{1}{2N_{L,\mathrm{MAI}}} \frac{1-\gamma_{\mathrm{MAI}}^2}{\gamma_{\mathrm{MAI}}^2} \tag{6.6}$$

and considering these as independent variables, the variances add when we compute the MAI interferogram (Jung et al., 2009). Therefore, since

$$\sigma_{\phi,\mathrm{MAI}} = \sqrt{\sigma_{\phi,\mathrm{forward}}^2 + \sigma_{\phi,\mathrm{backward}}^2} \,, \tag{6.7}$$

we write the MAI phase uncertainty as

$$\sigma_{\phi,\mathrm{MAI}} \approx \frac{\sqrt{2}}{\sqrt{2N_{L,\mathrm{MAI}}}} \frac{\sqrt{1-\gamma_{\mathrm{MAI}}^2}}{\gamma_{\mathrm{MAI}}} \,. \tag{6.8}$$

Equations 6.4 and 6.8 have similar forms, but there are additional losses included in the MAI variables. For example, aperture splitting reduces azimuth resolution, which decreases the effective number of looks by a factor of $(1-n)$. For a MAI interferogram, $N_{L,\mathrm{MAI}} = (1-n) \cdot N_L$. Beam splitting also decreases total correlation, where $\gamma_{\mathrm{MAI}}$ is related to Equation 6.5 by scaling SNR by $(1-n)$. SNR loss results

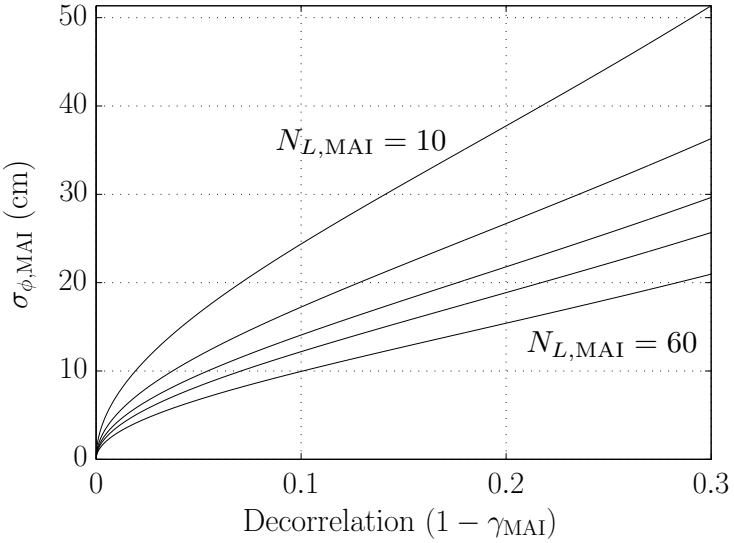


Figure 6.2: Theoretical MAI standard deviation versus decorrelation. Curves represent values of $N_{L,\mathrm{MAI}} = 10$, 20, 30, 40, and 60, with $n = 0.5$ and $l = 10$. Measurement uncertainty decreases monotonically with $N_{L,\mathrm{MAI}}$.

from a reduced antenna footprint, giving less along-track integration time (Jung et al., 2009). Both of these factors lead to an increase of MAI phase uncertainty, requiring higher coherence for low-noise interferograms. Figure 6.2 shows the measurement uncertainty as a function of decorrelation and number of effective looks. Compared to typical InSAR errors, which are on the order of 1 cm or less, MAI errors are much greater. Even for highly coherent pixels, the MAI error is around 10 cm, which illustrates why past studies have focused only on highly coherent interferograms.

Sensitivity is another implication of aperture splitting. At a wavelength $\lambda$, the phase in Equation 6.3 is a factor of $\frac{n\lambda}{l}$ (roughly 0.01 for ALOS) smaller than InSAR. This scaling causes significantly less phase for comparable deformation in a MAI interferogram. Phase sensitivity is improved by increasing $n$, but this also increases phase uncertainty (Bechor, 2006). For small deformation signals, this tradeoff can be problematic as the signal phase may be lower than the error terms.

Consider the MAI phase expanded to contain errors

$$\phi_{\mathrm{MAI}} = \phi_{\mathrm{defo}} + \sigma_{\phi,\mathrm{MAI}} + \phi_{\mathrm{proc}} \, . \tag{6.9}$$

The total phase is the sum of deformation, uncertainty, and processing artifacts. Some examples of artifacts could include interpolation errors, phase ramps, residual topography, atmospheric delays, or misregistration. Given the lack of sensitivity, relatively small processing errors can easily mask the observed deformation phase. To put this in perspective, let $\phi_{\text{proc}} = 0.1$ rad, $l = 10$ m, and $n = 0.5$. Using Equation 6.3, the deformation would have to be at least 15.9 cm for $\phi_{\text{defo}} > \phi_{\text{proc}}$. In contrast, InSAR is more sensitive to deformation, such that small processing errors are well below the signal level. For example, with L-Band InSAR ($\lambda = 0.23$ cm), deformation of only 1.8 mm would produce phase that is greater than the noise level of $\phi_{\text{proc}} = 0.1$ rad.

Phase sensitivity is one of the limiting factors in MAI, and small processing artifacts will lead to large errors in deformation estimates (Bechor, 2006). Case studies have found residual flat-Earth and topographic phase distortions from MAI processing, where resulting errors were in the range of 10 to 200 cm (Jung et al., 2009, 2011; Hu et al., 2012; McMillan et al., 2012). These levels are much greater than many deformation signals and without identifying and removing systematic errors, the accuracy of MAI interferograms is severely compromised.

## 6.4 Extension of SBAS to Vector Time-Series

The general concept behind our V-SBAS algorithm is that by combining InSAR measurements from several geometries and also including the corresponding MAI data, we can estimate three-dimensional vector time-series. The InSAR measurements give us diversity in the east and up directions, while MAI constrains the solution the in the north.

The V-SBAS algorithm is separated into two parts: an initial inversion to estimate ENU velocities (Section 6.4.2) and a secondary inversion that imposes spatial constraints in the re-estimation of the northward component (Section 6.6). Before detailing our approach, we use a single radar geometry to introduce notation and to review the existing SBAS techniques.

### 6.4.1 SBAS with a Single Radar Geometry

The SBAS algorithm was introduced in Berardino et al. (2002), as a method to monitor the temporal evolution of deformation by forming all possible small baseline interferograms within a set of SAR scenes. The authors impose a small baseline constraint to minimize spatial decorrelation, which gives subsets of interferometric pairs. After co-registration, they form a data vector $\boldsymbol{\delta\phi}$, from the differential phases at each pixel and related this to the unknown phase velocity vector $\mathbf{v}$, as

$$\boldsymbol{\delta\phi} = \mathbf{G}\mathbf{v} \,. \tag{6.10}$$

The system matrix $\mathbf{G}$ is known (Berardino et al., 2002), and the velocity at the $i^{th}$ epoch is defined as

$$v_i = \frac{\phi_i - \phi_{i-1}}{t_i - t_{i-1}} \,, \tag{6.11}$$

where $t$ is the time and $\phi$ is the unknown phase. Since only small baseline pairs are considered, the system of equations is overdetermined, but has possible rank deficiency (Berardino et al., 2002). In this event, they solve Equation 6.10 using a pseudoinverse, which is computed with a singular value decomposition (SVD) of $\mathbf{G}$ (Aster et al., 2005). This approach gives the minimum velocity norm solution, reducing the magnitude of outliers in the time-series estimates. Once $\mathbf{v}$ is known, they integrate the phase velocity with the known matrix $\mathbf{L}$, producing a phase time-series vector

$$\boldsymbol{\phi} = \mathbf{L}\mathbf{v} \,. \tag{6.12}$$

This time-series is derived from a single geometry, representing deformation projected onto the radar's LOS, and thus the SBAS estimate is one-dimensional.

### 6.4.2 V-SBAS Using Multiple Radar Geometries

The block diagram in Figure 6.3 gives an overview of the new multi-geometry algorithm. We start with sets of data from $K$ radar geometries. As in Equation 6.1,

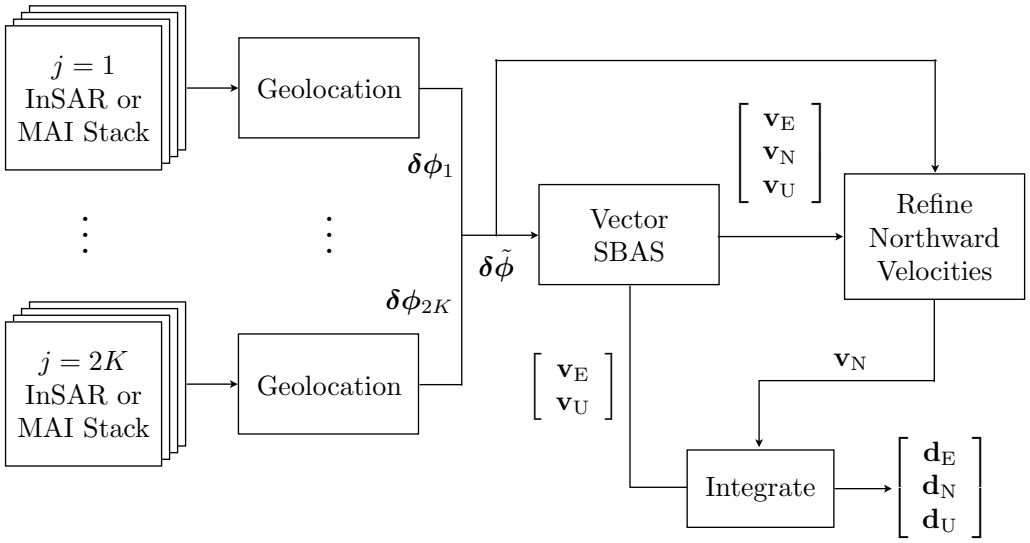


Figure 6.3: Block diagram of the V-SBAS algorithm, combining geocoded stacks of InSAR and MAI data in a joint inversion for the ENU velocity time-series. Following the initial V-SBAS estimate, a secondary inversion is used to refine the northing component. The velocity vectors are then integrated to produce a vector deformation time-series.

a geometry, defined by heading and look angle, has LOS and along-track measurements, giving $J = 2K$ total sets of data. The $j^{th}$ set is a stack of unwrapped MAI or InSAR interferograms from one of the $K$ geometries, which limits the set index to $j \leq J = 2K$. Similar to LOS-SBAS, we implement time-series estimation on a pixel-by-pixel basis, but since each stack exists in different radar coordinates, we first geolocate the data to to align measurements onto a common grid.

For the $j^{th}$ set of data, we have a measurement vector, $\boldsymbol{\delta\phi}_j \in \mathbb{R}^{M_j}$, where $M_j$ is the number of interferograms. Relating the measurements to the unknown phase velocity, we write

$$\boldsymbol{\delta\phi}_j = \left[-\boldsymbol{l}_j^T \otimes \mathbf{G}_j\right] \tilde{\mathbf{v}} \,, \tag{6.13}$$

where $\boldsymbol{l}_j \in \mathbb{R}^3$ is defined in Equation 6.1, $\mathbf{G}_j \in \mathbb{R}^{M_j \times N}$, and $\otimes$ represents the Kronecker product. $\tilde{\mathbf{v}}$ includes ENU velocities for each of the epochs in all $K$ geometries,

such that $\tilde{\mathbf{v}} \in \mathbb{R}^{3N}$ with

$$N = \sum_{k=1}^{K} N_k - 1 \, . \tag{6.14}$$

Compared to standard SBAS in Equation 6.10, $\mathbf{G}_j$ has a width of $N$, rather than $N_k - 1$, where $N_k$ represents the number of epochs in the $k^{th}$ geometry. We refer the reader to Berardino et al. (2002) for the formation of $\mathbf{G}_j$, and note that our system matrix is augmented by including the look vector $\boldsymbol{l}$. This modification is necessary to project the ENU velocities onto the appropriate geometry.

Expanding Equation 6.13 to include all sets of data, we form the V-SBAS system of equations by stacking the measurement vectors and system matrices

$$\mathbf{B} \begin{bmatrix} \boldsymbol{\delta\phi}_1 \\ \boldsymbol{\delta\phi}_2 \\ \vdots \\ \boldsymbol{\delta\phi}_{2K} \end{bmatrix} = \begin{bmatrix} \boldsymbol{l}_1^T \otimes \mathbf{G}_1 \\ \boldsymbol{l}_2^T \otimes \mathbf{G}_2 \\ \vdots \\ \boldsymbol{l}_{2K}^T \otimes \mathbf{G}_{2K} \end{bmatrix} \begin{bmatrix} \mathbf{v}_{\mathrm{E}} \\ \mathbf{v}_{\mathrm{N}} \\ \mathbf{v}_{\mathrm{U}} \end{bmatrix} , \tag{6.15}$$

where $\tilde{\mathbf{v}}^T = \left[\mathbf{v}_{\mathrm{E}}^T, \mathbf{v}_{\mathrm{N}}^T, \mathbf{v}_{\mathrm{U}}^T\right]^T$ and the differential phases are converted to displacement through $\mathbf{B} \in \mathbb{R}^{M \times M}$. This transformation is important to account for the unique phase relationships between InSAR and MAI. As a result, the velocity time-series will be in units of displacement rate, not phase rate. Defining

$$M = \sum_{j=1}^{2K} M_j \, , \tag{6.16}$$

the $m^{th}$ element of the diagonal matrix $\mathbf{B}$ is

$$B_m = \begin{cases} \frac{\lambda}{4\pi} & , \text{ InSAR} \\ \frac{l}{4\pi n} & , \text{ MAI} \end{cases} \tag{6.17}$$

which applies a different scaling depending on the source of the measurement. This scaling would also change if observations were combined from multiple platforms, for example, radars with different antenna sizes or wavelengths (Pepe et al., 2005).

Finally, for convenience we write Equation 6.15 in a form analogous to Equation 6.10 as

$$\mathbf{B}\boldsymbol{\delta}\tilde{\boldsymbol{\phi}} = \tilde{\mathbf{G}}\tilde{\mathbf{v}} \tag{6.18}$$

with $\boldsymbol{\delta}\tilde{\boldsymbol{\phi}} \in \mathbb{R}^M$ and $\tilde{\mathbf{G}} \in \mathbb{R}^{M \times 3N}$.

The small baseline criterion in SBAS leads to potential rank deficiency of Equation 6.10. Although the V-SBAS algorithm uses similar small baseline subsets, the system of equations in Equation 6.18 will always be rank deficient. For example, consider a single platform that can only make one observation at a time. At each epoch, we have at most two measurements, one from InSAR and another from MAI. Ideally we want three simultaneous and independent observations to properly constrain the problem, but this is not possible with current satellite sensors. Mismatched temporal sampling between each geometry causes the problem to be poorly constrained. This complication could be circumvented by combining multiple sensors or by using airborne platforms, but here, we consider only a single satellite-based radar. In addition, we may omit subsets of the data due to phase artifacts or low coherence. In this case, there are fewer than two observations, which further reduces the rank. We will see this effect in Chapter 7, where portions of the MAI data were omitted from our analysis.

We compute the solution to Equation 6.18 using a pseudoinverse, finding the minimum ENU velocity norm solution. As before, the motivation for this approach is to reduce spurious velocity spikes, which lead to outliers in the displacement time-series. In the context of V-SBAS, the missing samples, either from geometric limitations or excluded data, correspond to unconstrained epochs, where contributions from the null space may corrupt the solution. In using the minimum norm, we force the velocities at unconstrained samples to be small, resulting in smooth, approximately linear, periods to fill in the gaps. With $\tilde{\mathbf{v}}$ known, we integrate the velocities in each dimension to produce a vector time-series

$$\tilde{\mathbf{d}} = \begin{bmatrix} \mathbf{d}_{\mathrm{E}} \\ \mathbf{d}_{\mathrm{N}} \\ \mathbf{d}_{\mathrm{U}} \end{bmatrix} = \tilde{\mathbf{L}}\tilde{\mathbf{v}}\,, \tag{6.19}$$

where $\mathbf{d}_{\mathrm{E}}$, $\mathbf{d}_{\mathrm{N}}$ , and $\mathbf{d}_{\mathrm{U}} \in \mathbb{R}^{N+1}$ are the deformation time-series and $\tilde{\mathbf{L}} \in \mathbb{R}^{3(N+1)\times 3N}$ is the known integration matrix. Finally, letting $\tilde{\mathbf{G}}^{\dagger}$ represent the pseudo-inverse of $\tilde{\mathbf{G}}$, we write the V-SBAS time-series covariance as

$$\boldsymbol{\Sigma}_{\tilde{\mathbf{d}}} = \tilde{\mathbf{d}}\tilde{\mathbf{d}}^{T} = \tilde{\mathbf{L}}\tilde{\mathbf{G}}^{\dagger}\mathbf{B}\boldsymbol{\Sigma}_{\boldsymbol{\delta}\tilde{\boldsymbol{\phi}}}\mathbf{B}^{T}(\tilde{\mathbf{G}}^{\dagger})^{T}\tilde{\mathbf{L}}^{T}\,, \tag{6.20}$$

where $\boldsymbol{\Sigma}_{\boldsymbol{\delta}\tilde{\boldsymbol{\phi}}}$ is the covariance of the InSAR and MAI data. If the data covariance matrix is unknown, we can simplify the expression by defining a constant $\sigma^2$ and allowing $\mathbf{B}\boldsymbol{\Sigma}_{\boldsymbol{\delta}\tilde{\boldsymbol{\phi}}}\mathbf{B}^{T} = \sigma^2\mathbf{I}$. This simplified form incorrectly assumes a uniform variance across the data, however, it can be useful in illustrating how the structure of the $\tilde{\mathbf{G}}^{\dagger}$ influences the variance of our time-series estimate. Letting $\sigma^2 = 1$, we define the normalized time-series covariance matrix as

$$\boldsymbol{\Sigma}_{\tilde{\mathbf{d}}} = \tilde{\mathbf{d}}\tilde{\mathbf{d}}^{T} = \tilde{\mathbf{L}}\tilde{\mathbf{G}}^{\dagger}(\tilde{\mathbf{G}}^{\dagger})^{T}\tilde{\mathbf{L}}^{T}\,. \tag{6.21}$$

At this point, it is worth noting a few strengths and limitations of combining multiple data sets. In particular, one drawback is a loss of spatial coverage from the footprint overlap of each geometry. Our approach assumes multiple look directions, therefore, considering only their spatial intersection will restrict the available area of study. Furthermore, we rely on pixels retaining coherence across the stack, so areas are ignored that do not fit some specification of coherence over time (Berardino et al., 2002). Given the uncertainty of MAI, these data will limit the regions that are considered coherent with time and will further reduce the spatial coverage.

On the other hand, one benefit of combining data in a joint estimation is increased temporal sampling. This advantage comes from the fact that we estimate deformation at the complete set of $N$ epochs, rather than $N_k$ as in SBAS. With $N$ representing the total number of SAR scenes, the joint estimation approach can significantly increase the density of time-series points over that of a single geometry. Every epoch is not fully constrained by the data, however, the SVD solution minimizes the norm of the time-series velocities, such that the missing points are interpolated to keep the backward difference in Equation 6.11 low. Another benefit is reduced uncertainty in the time-series estimate. Since we form all small-baseline interferometric pairs, there

is redundancy in the observations and the effects of phase errors are lessened when we simultaneously fit the entire set of data. As a result, the time-series errors can be significantly lower than the InSAR and MAI uncertainties in Equations 6.4 and 6.8. As shown in Equation 6.20, the degree of noise suppression is dependent on the structure of $\tilde{\mathbf{G}}$, but in general, more observations will result in lower time-series errors.

## 6.5 Time-Series Constraints using Separability

SBAS analysis relies on the minimum velocity norm solution to control the effects of the null space. This is a constraint in time, and while one could impose spatial constraints through joint pixel solutions or by including a geophysical model, on a pixel-by-pixel basis, temporal smoothing is the best option generally available. In contrast to SBAS, our approach produces a multidimensional time-series. In many cases, it is reasonable to believe that some relationship exists between the various directional components, for example, restrictions on the direction of deformation or some concept of joint smoothness among the components. In this section we introduce the separability of deformation into space and time functions as a means to demonstrate a constant direction of deformation. If separability holds, then we can use this as an additional constraint in the V-SBAS inversion. We first present separability using a simple source model, and then give an approach to validate separability with a PCA on existing time-series data.

### 6.5.1 Constraints from a Simple Source Model

Consider a simple spherical magma chamber, widely known as the Mogi source (Mogi, 1958). An illustration is given in Figure 6.4, where the magma chamber lies at a depth $a$, with a radius $r$, within an elastic half-space. At time $t$, the volume changes by an amount $\Delta V(t)$, causing deformation at the surface of the Earth. This simple model is circularly symmetric about the center of the chamber, thus the deformation can be described by displacement in the radial (north or east) and upward directions. Using

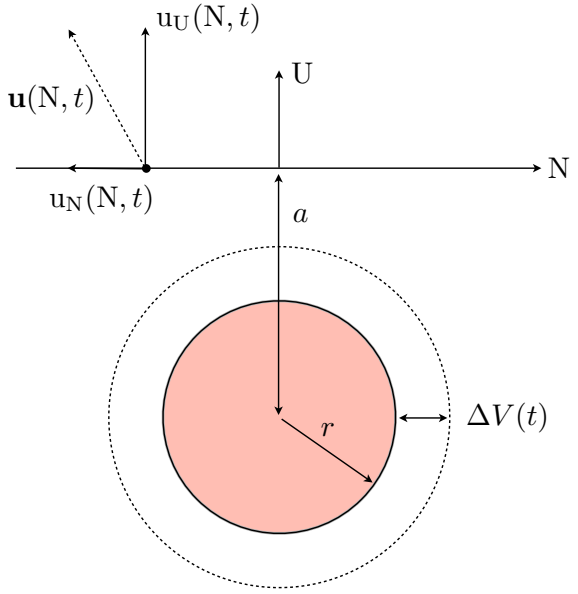


Figure 6.4: A spherical magma chamber at depth $a$, radius $r$, and time changing volume $\Delta V(t)$. Deformation is in the $\mathbf{u}(\mathrm{N},t)$ direction, with north and up components given by $u_N(N,t)$ and $u_U(N,t)$.

a generic spatial variable $\mathbf{x}$, the surface deforms in the $\mathbf{u}(\mathbf{x},t) = [u_N(\mathbf{x},t), u_U(\mathbf{x},t)]^T$ direction, radially away from the center of the sphere. Assuming that the source depth is unchanging as the cavity expands, we can write the displacement components as separable functions of space and time (Segall, 2010), with spatial functions $f_U(\mathbf{x},a)$ and $f_N(\mathbf{x},a)$ in the up and north directions.

$$\begin{aligned} u_U(\mathbf{x},t) &= f_U(\mathbf{x},a)\cdot\Delta V(t) \\ u_N(\mathbf{x},t) &= f_N(\mathbf{x},a)\cdot\Delta V(t)\,. \end{aligned} \tag{6.22}$$

Taking the ratio of the components,

$$\frac{u_N(\mathbf{x},t)}{u_U(\mathbf{x},t)} = \frac{f_N(\mathbf{x},a)}{f_U(\mathbf{x},a)} = \alpha_U\,, \tag{6.23}$$

the time function cancels, leaving a spatially varying, but temporally constant ratio of $\alpha_U$. This value defines the tangent of the angle between $\mathbf{u}(\mathbf{x},t)$ and the vertical.

If this angle does not change with time, then the direction is fixed. The length of the vector varies with $\Delta V(t)$, but the direction is constant until the source depth is altered.

In a discrete sense, $\mathbf{u}(\mathbf{x}, t)$ defines displacement from one time-step to another, where the chamber expands or contracts by some amount. The vectors in Equation 6.19 represent deformation relative to the first epoch. In terms of these variables, we rewrite Equation 6.23 as

$$\frac{d_{\mathrm{N},i} - d_{\mathrm{N},i-1}}{d_{\mathrm{U},i} - d_{\mathrm{U},i-1}} = \frac{v_{\mathrm{N},i}}{v_{\mathrm{U},i}} = \alpha_{\mathrm{U}} \,, \tag{6.24}$$

with subscripts denoting the $i^{th}$ element of the deformation and velocity times-series. Assuming this relationship holds for all time, we can expand Equation 6.24 to all dimensions as simple relationships of proportionality between the velocity vectors.

$$\begin{aligned} \mathbf{v}_{\mathrm{N}} &= \mathbf{v}_{\mathrm{E}}\, \alpha_{\mathrm{E}} \\ \mathbf{v}_{\mathrm{N}} &= \mathbf{v}_{\mathrm{U}}\, \alpha_{\mathrm{U}} \,. \end{aligned} \tag{6.25}$$

If separability holds, then Equation 6.25 is valid and we can use the expression to constrain the least-squares minimization of Equation 6.18. The solution is found by solving

$$\begin{aligned} \text{minimize} \quad & \|\mathbf{B}\boldsymbol{\delta}\tilde{\boldsymbol{\phi}} - \tilde{\mathbf{G}}\tilde{\mathbf{v}}\|_2 + \mu\|\tilde{\mathbf{v}}\|_2 \\ \text{subject to} \quad & \mathbf{v}_{\mathrm{N}} = \alpha_{\mathrm{E}}\mathbf{v}_{\mathrm{E}} \\ & \mathbf{v}_{\mathrm{N}} = \alpha_{\mathrm{U}}\mathbf{v}_{\mathrm{U}} \end{aligned} \tag{6.26}$$

where $\alpha_{\mathrm{E}}$, $\alpha_{\mathrm{U}}$, and $\tilde{\mathbf{v}}$ are unknown. The regularization parameter $\mu$ restricts the velocity norm and the constraints impose a constant direction of deformation. Letting

$$\tilde{\mathbf{G}} = [\mathbf{G}_{\mathrm{E}}\ \mathbf{G}_{\mathrm{N}}\ \mathbf{G}_{\mathrm{U}}] \,, \tag{6.27}$$

an equivalent problem can be formulated as the minimization of

$$\left\| \mathbf{B}\boldsymbol{\delta}\tilde{\boldsymbol{\phi}} - \mathbf{G}_{\mathrm{E}}\frac{\mathbf{v}_{\mathrm{N}}}{\alpha_{\mathbf{E}}} - \mathbf{G}_{\mathrm{N}}\mathbf{v}_{\mathrm{N}} - \mathbf{G}_{\mathrm{U}}\frac{\mathbf{v}_{\mathrm{N}}}{\alpha_{\mathbf{U}}} \right\|_2 + \mu \left\| \begin{array}{c} \frac{\mathbf{v}_{\mathrm{N}}}{\alpha_{\mathrm{E}}} \\ \mathbf{v}_{\mathrm{N}} \\ \frac{\mathbf{v}_{\mathrm{N}}}{\alpha_{\mathrm{U}}} \end{array} \right\|_2 , \tag{6.28}$$

with respect to $\mathbf{v}_{\mathrm{N}}$, $\alpha_{\mathrm{E}}$, and $\alpha_{\mathrm{U}}$, where the proportionality relationships have been substituted into the objective function. The solution to either Equation 6.26 or Equation 6.28 attempts to minimize outliers in each component of the final time-series, and through separability, ensures that one component does not accelerate with respect to the others. For a constant source geometry, separability allows us to relate all components of the time-series to produce a more realistic solution.

In general, this minimization problem is difficult to solve. The equations are non-convex and nonlinear, preventing the use of efficient solvers (Boyd & Vandenberghe, 2004). Approaches exist for nonlinear least-squares problems, but these are typically iterative and are very sensitive to initial conditions (Aster et al., 2005). Furthermore, the solution depends on an arbitrary regularization parameter that will greatly affect the results. There are automated methods to choose optimal regularization parameters, but since the noise characteristics vary spatially, we must search for the optimal parameter at each pixel.

In Section 6.6 we relax the problem and present a more practical linear solution to re-estimate only the noisy, MAI constrained, northward component. This approach loosely enforces the constant direction assumption and does not depend on nonlinear inversions or regularization parameters.

### 6.5.2 Verifying Separability Through PCA

The previous example demonstrated separability using a very simple source model. In reality, the underlying geophysical processes are most likely more complicated or include a combination of several sources. In this section, we show how applying PCA to an existing geodetic time-series can be used to validate the constant direction assumption for an unknown source. If the data are distributed across the area of

interest, then a constant direction of deformation at all points will justify the use of Equation 6.25 as V-SBAS constraints.

Consider GPS time-series at $P$ stations and $N$ identical epochs. We form a matrix $\mathbf{X} \in \mathbb{R}^{3P \times N}$ where each row corresponds to the time-series from one ENU component, with the row-by-row mean removed (Kositsky & Avouac, 2010; Lin et al., 2010). This configuration defines the matrix such that each column represents deformation across the scene, at a particular time. PCA follows from the eigendecomposition of the covariance matrix, therefore, we find the eigenvectors of the spatial and temporal covariance matrices, $\mathbf{X}\mathbf{X}^T$ and $\mathbf{X}^T\mathbf{X}$, by SVD of $\mathbf{X}$

$$\mathbf{X} = \mathbf{U}\mathbf{S}\mathbf{V}^T = \sum_{i=1}^{r} s_i \mathbf{u}_i \mathbf{v}_i^T \,, \tag{6.29}$$

where $r$ is the rank of $\mathbf{X}$, $\mathbf{u}_i \in \mathbb{R}^{3P}$ and $\mathbf{v}_i \in \mathbb{R}^N$ are the columns of $\mathbf{U}$ and $\mathbf{V}$, and $s_i$ are the diagonal entries of $\mathbf{S}$. In this decomposition, the $i^{th}$ column of $\mathbf{U}$ represents a three-dimensional deformation direction at each station. This direction varies in space, and the total signal is the weighted sum of all $r$ components. The $i^{th}$ column of $\mathbf{V}$ represents a time function that determines the temporal contribution of the $i^{th}$ spatial component, and the singular values give the relative weighting. We note that standard decomposition arranges the singular values in descending order, such that the first component explains the most variance in the data.

In the event that only the first singular value is non-zero, $\mathbf{X}$ reduces to

$$\mathbf{X} = s_1 \mathbf{u}_1 \mathbf{v}_1^T \tag{6.30}$$

where each station deforms in a direction defined by $\mathbf{u}_1$ and changes in time based on $\mathbf{v}_1$. This is similar to Equation 6.22, which gives the deformation components as separable functions of space and time. Following a similar analysis, we let $u_1$, $u_2$, and $u_3$ be the first three elements of $\mathbf{u}_1$, representing the ENU components at the first station and let $v_1$ and $v_2$ be the first two elements of $\mathbf{v}_1$, representing the first two epochs of the time function. Using the notation in Equation 6.24, where $v_{\mathrm{N},2}$ and $v_{\mathrm{U},2}$

are the velocities at the second epoch, we write

$$\frac{v_{\mathrm{N},2}}{v_{\mathrm{E},2}} = \frac{s_1 u_2 \cdot (v_2 - v_1)}{s_1 u_3 \cdot (v_2 - v_1)} = \frac{u_2}{u_3} = \alpha_{\mathrm{U}} \tag{6.31}$$

which is equivalent to Equation 6.24. This holds for all $P$ stations and for all $N$ times (with $\alpha_{\mathrm{U}}$ varying at each station), therefore, if the PCA over a network of geodetic time-series has only one non-zero singular value, then the deformation is separable, and the direction at each station is constant with time. Numerically, this condition may never hold exactly for real data, however, we can assume separability if the second singular value is significantly smaller than the first.

Given time-series sparsely covering the area of interest, a PCA can be used to infer if separability constraints are appropriate for the V-SBAS solution. Even if only V-SBAS time-series are available, a PCA applied to those data can reveal an approximately constant direction of deformation, and then be used to refine these estimates. On a final note, as in the previous section, this approach is only valid if the source geometry remains unchanged. Therefore, it may not be applicable to multiple sources with different temporal histories or sources that continually change in time. In the case of a known event, it would also be necessary to separately analyze each of the constant intervals. We present an example of disjoint analysis in Chapter 7 for periods before and after the Father's Day deformation event at Kilauea Volcano, Hawaii on June 17th, 2007.

## 6.6 Re-estimation of the North Time-Series Component

In Section 6.5.1, we showed that the optimal V-SBAS estimation problem with constant direction constraints is nonlinear. This problem can be solved, but often nonlinear techniques are computationally expensive and, for our purposes, will depend on a regularization parameter. Considering that time-series estimation could be required for up to a million points for a given scene, we present an alternative linear approach

that depends only on unregularized least-squares techniques.

Illustrated in Figure 6.3, a vector inversion (Section 6.4.2) is initially used to estimate the velocity time-series in all three-dimensions. We then use these results in a secondary inversion to re-estimate the northward component. By taking the east and up time-series as known quantities, we estimate the $\alpha$ constants separately from the time-series, removing the nonlinearity of the problem. Once the constants are known, a value of $\mathbf{v}_\mathrm{N}$ can then be found that is a best fit for the constraints in Equation 6.25.

This approach focuses on the north component being the noisiest of the initial time-series estimate, necessitating additional constraints. Our rationale is that the north component is almost entirely represented by the MAI data, which was shown in Section 6.3.1 to have higher uncertainty and to be more susceptible to processing artifacts than conventional InSAR. Compared to the east and up directions, which are derived predominantly using LOS observations, the north errors are expected to be much higher. There will be errors in the LOS data, but relatively speaking, these components will be higher quality and are assumed to be quite accurate in the initial solution. This assertion can be justified by noting several other examples of InSAR accurately estimating east and upward deformation, without further constraints (Sandwell et al., 2008; Fialko et al., 2005, 2001; Wright et al., 2004; Ng et al., 2012).

Using the results of the initial inversion, we form a north-only data vector by removing the east and up components

$$\mathbf{B}\boldsymbol{\delta}\tilde{\boldsymbol{\phi}}_\mathrm{N} = \mathbf{B}\boldsymbol{\delta}\tilde{\boldsymbol{\phi}} - \mathbf{G}_\mathrm{E}\mathbf{v}_\mathrm{E} - \mathbf{G}_\mathrm{U}\mathbf{v}_\mathrm{U} \tag{6.32}$$

such that

$$\mathbf{B}\boldsymbol{\delta}\tilde{\boldsymbol{\phi}}_\mathrm{N} = \mathbf{G}_\mathrm{N}\mathbf{v}_\mathrm{N} \tag{6.33}$$

The proportionality constants are then estimated by solving

$$\begin{bmatrix} \mathbf{B}\boldsymbol{\delta}\tilde{\boldsymbol{\phi}}_\mathrm{N} \\ \mathbf{B}\boldsymbol{\delta}\tilde{\boldsymbol{\phi}}_\mathrm{N} \end{bmatrix} = \begin{bmatrix} \mathbf{G}_\mathrm{N}\mathbf{v}_\mathrm{E} & \mathbf{0} \\ \mathbf{0} & \mathbf{G}_\mathrm{N}\mathbf{v}_\mathrm{U} \end{bmatrix} \begin{bmatrix} \alpha_\mathrm{E} \\ \alpha_\mathrm{U} \end{bmatrix} \tag{6.34}$$

where the $\alpha$ parameters represent a least-squares fit to the slope of $\mathbf{d}_{\mathrm{N}}$ versus $\mathbf{d}_{\mathrm{E}}$ or $\mathbf{d}_{\mathrm{U}}$. By estimating a single average slope parameter in each dimension, rather than a full time-series, we reduce the effects of large errors by fitting average trends in the MAI data. Letting $\mathbf{I}$ be the identity matrix, we re-estimate the north component as the least-squares fit to the separability constraints in Equation 6.25

$$\begin{bmatrix} \mathbf{v}_{\mathrm{E}}\,\alpha_{\mathrm{E}} \\ \mathbf{v}_{\mathrm{U}}\,\alpha_{\mathrm{U}} \end{bmatrix} = \begin{bmatrix} \mathbf{I} \\ \mathbf{I} \end{bmatrix} \mathbf{v}_{\mathrm{N}}\,, \tag{6.35}$$

giving a solution that deforms in an approximately constant direction.

The proportionality constraints are valid only if the ratio of the velocities stays constant throughout the entire span of the time-series. If the direction changes, say before and after an eruption, or if some event causes the components to instantaneously deform at different rates, then we should alter Equation 6.25 to reflect dissimilar ratios before and after the event. Letting $\boldsymbol{\alpha} = [\alpha_{\mathrm{E,b}}, \alpha_{\mathrm{E,a}}, \alpha_{\mathrm{U,b}}, \alpha_{\mathrm{U,a}}]^T$ represent a vector of constants in the east and north directions, with subscripts denoting periods before and after the event, Equation 6.34 can be re-written as

$$\begin{bmatrix} \mathbf{B}\boldsymbol{\delta}\tilde{\boldsymbol{\phi}}_{\mathrm{N}} \\ \mathbf{B}\boldsymbol{\delta}\tilde{\boldsymbol{\phi}}_{\mathrm{N}} \end{bmatrix} = [\mathbf{I} \otimes \mathbf{G}_{\mathrm{N}}] \begin{bmatrix} \mathbf{v}_{\mathrm{E,b}} & \mathbf{0} & \mathbf{0} & \mathbf{0} \\ \mathbf{0} & \mathbf{v}_{\mathrm{E,a}} & \mathbf{0} & \mathbf{0} \\ \mathbf{0} & \mathbf{0} & \mathbf{v}_{\mathrm{U,b}} & \mathbf{0} \\ \mathbf{0} & \mathbf{0} & \mathbf{0} & \mathbf{v}_{\mathrm{U,a}} \end{bmatrix} \boldsymbol{\alpha} \tag{6.36}$$

where the east and up velocity vectors are split into periods before and after the event as $\mathbf{v}_{\mathrm{E}} = \left[\mathbf{v}_{\mathrm{E,b}}^T \mathbf{v}_{\mathrm{E,a}}^T\right]^T$ and $\mathbf{v}_{\mathrm{U}} = \left[\mathbf{v}_{\mathrm{U,b}}^T \mathbf{v}_{\mathrm{U,a}}^T\right]^T$. Using the four constants to weight the pre- and post-event intervals, we re-estimate the northward component as

$$\begin{bmatrix} \mathbf{v}_{\mathrm{E,b}}\,\alpha_{\mathrm{E,b}} \\ \mathbf{v}_{\mathrm{E,a}}\,\alpha_{\mathrm{E,a}} \\ \mathbf{v}_{\mathrm{U,b}}\,\alpha_{\mathrm{U,b}} \\ \mathbf{v}_{\mathrm{U,a}}\,\alpha_{\mathrm{U,a}} \end{bmatrix} = \begin{bmatrix} \mathbf{I} \\ \mathbf{I} \end{bmatrix} \mathbf{v}_{\mathrm{N}}\,. \tag{6.37}$$

This modified approach assumes that the date of the event is known, but it allows

for different directions and disproportionate jumps in the velocity ratios.

The are many possible approaches to solving the relaxed problem of constraining only the northward component. For instance, after solving for the ratio parameters, we could have substituted these into Equation 6.28 to estimate $\mathbf{v}_{\mathrm{N}}$. This approach relies on the noisy MAI data to estimate the time-series, whereas our method uses the noisy data to estimate only average slope parameters, reducing the influence of errors. In addition, the east and up components are typically smooth from the SVD solution to Equation 6.15, therefore, in taking the north to be a linear combination of the east and up, the north component will also be smooth. In experiments, we found that even with a minimum norm solution, direct substitution into Equation 6.28 leads to outliers in the time-series. In either case, re-estimating the north by including directionality constraints provides another means to restrict the solution and estimate a more realistic model.

## 6.7 Summary

We present a new approach called V-SBAS to estimate the temporal evolution of the full vector deformation field, using observations from InSAR and MAI at multiple radar geometries. Our approach is an extension of the SBAS time-series technique and multidimensional InSAR. We develop the equations necessary to combine multiple LOS geometries and discuss approaches to solving the joint system of equations. Using a minimum norm solution, we estimate vector time-series at all epochs in the ENU directions. Compared to SBAS, our approach increases the dimensionality and temporal sampling of the time-series. Furthermore, by forming all small-baseline pairs, there is redundancy in the measurements, which results in time-series with errors below those of MAI or InSAR alone. This increase in precision will allow us to apply V-SBAS to regions with levels of deformation below the MAI noise floor.

We also present the concept of space-time separability in deformation time-series and show how this property implies a constant direction for deformation. We demonstrate separability using PCA on existing time-series data and show that for periods

dominated by a single principal component, separability and the assumption of constant direction hold. If the PCA verifies separability over the entire region of study, then we can use a constant direction as an additional constraint in the V-SBAS inversion. We show how directionality relates to the original time-series variables and give expressions for the constrained V-SBAS equations. These equations are nonlinear in the ratios of the unknown velocity vectors, which leads us to propose an alternate linear solution to re-estimate and constrain only the northward time-series component. We focus on constraining only the north, because it is estimated primarily from the MAI data, which has increased phase errors and sensitivity to processing artifacts.

Our presentation of the V-SBAS equations is general, but only considering spaceborne InSAR and MAI, the system of equations will always be rank deficient. This deficiency occurs because a given satellite geometry can only make LOS and along-track observations at a single point in time. Without including other types of geodetic measurements, we rely on the minimum norm solution and separability constraints to minimize contributions from the null space and reduce time-series outliers.

# Chapter 7

# Vector Time-Series at Kilauea Volcano, Hawaii

## 7.1 Introduction

In this chapter we demonstrate and verify the V-SBAS algorithm with a case study of the 2007 Fathers Day intrusion and eruption at the east rift zone (ERZ) of Kilauea Volcano, Hawaii. We use InSAR and MAI from six radar geometries to estimate ENU vector time-series near the Kilauea caldera and ERZ. For each radar geometry, we use the motion compensation algorithm in Chapter 3 and process all SAR scenes to a common global reference track, where we include the processor modifications from Chapter 4 to preserve coherence. For each geometry, we form all small-baseline interferometric pairs and geocode using the algorithm in Chapter 5. After geolocation, all measurements are aligned on a uniform WGS84 grid, and we then use the MAI and InSAR data to jointly estimate V-SBAS time-series as described in Chapter 6.

This chapter is organized as follows. Section 7.2 describes the test site at Kilauea Volcano and the 2007 Father's Day event. Section 7.3 introduces the MAI and InSAR data from the ALOS PALSAR sensor and discusses data processing. Section 7.4.1 verifies separability and the constant direction constraint with a PCA of GPS data at Kilauea. Sections 7.4.2 and 7.4.3 show vector time-series results from both the constrained and unconstrained solutions. Compared to GPS, the unconstrained

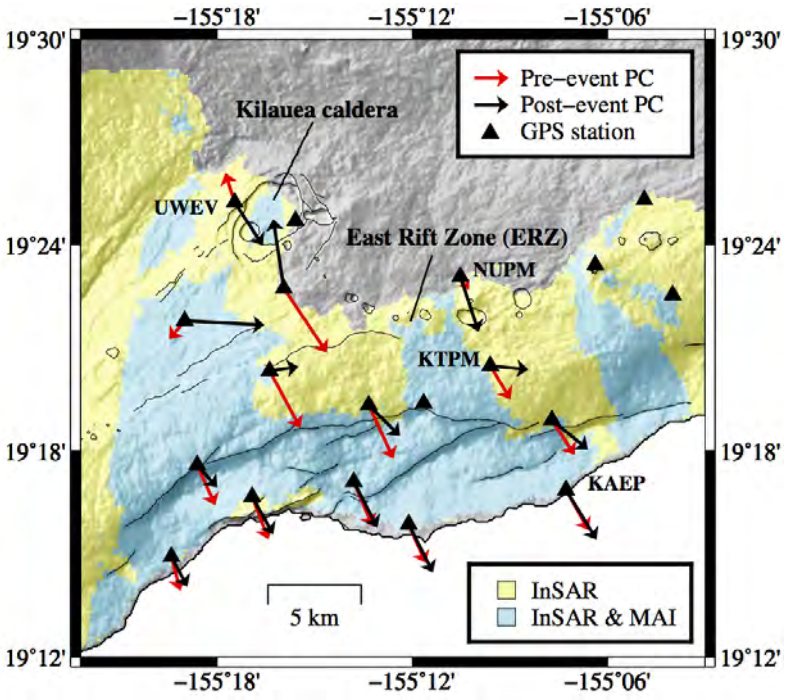


Figure 7.1: Shaded relief map for Kilauea Volcano and the East Rift Zone. Colors represent the SBAS coherent regions for InSAR and for the combined set of InSAR and MAI data in Table 7.1. The arrows represent the first principal component (PC) directions at GPS stations before and after the event. Stations not spanning the entire time-series are omitted from the PCA.

results show root mean square (RMS) errors on the order of 2 cm in the east and up directions, with much larger errors of 6.6 cm in the north. The separability constraints reduce the overall average north errors by 2 cm, although, in many instances, the gains from the constrained solution were much greater at individual stations. Our summary and discussion is presented in Section 7.5.

## 7.2 Test Site Description

Since 1983, Kilauea Volcano, on the island of Hawaii, has erupted almost continuously from the Pu'u 'Ō'ō and Kupaianaha vents on the east rift zone (Figure 7.1) (Heliker & Mattox, 2003). These vents are fed laterally by the shallow magma system of Kilauea, which consists of two reservoirs beneath the summit caldera (Cervelli &

Miklius, 2003). Throughout the Pu'u 'Ō'ō eruption history, the continuous activity has been interrupted on several occasions by episodic intrusions and eruptions in the region between the summit and Pu'u 'Ō'ō. As magma flows from the reservoirs to the ERZ, deformation during these events is typically characterized by rapid deflation of the summit and dilation of the ERZ (Larson et al., 2010).

In late 2003, the Kilauea summit began to slowly inflate, accumulating 0.55 m of extension and 0.25 m of uplift by mid-2007. Sulfur dioxide emissions also increased from the ERZ, which when coupled with the summit inflation, signaling an increase of magma in the volcanic system (Poland et al., 2008). Between June 17 (Father's Day) and June 20, 2007, an episode of volcanic activity at Kilauea Volcano resulted in rapid subsidence of the Kilauea caldera and a dike intrusion and eruption along the ERZ. The associated deformation was large, with an opening at the ERZ of more than 1.9 m (Sandwell et al., 2008) and deflation at Kilauea's summit of tens of cm. Following the event, the Kilauea caldera and ERZ both begin to subside at relatively slow rates of a few cm/yr.

The Father's Day event at Kilauea had three distinct periods of activity: the summit uplift preceding June 17, 2007, the eruption and intrusion between June 17 and June 20, and the long-term deflation that followed. The Father's Day deformation was large, therefore interferograms spanning the event will have significant deformation phase. On the other hand, the pre- and post-event periods were characterized by slow deformation rates, which means that InSAR pairs with small temporal baselines, or those that do not span the event, will have substantially less deformation signal. In many cases, especially for MAI, these measurements will be well below the phase noise floor. As a result, it will be more difficult to accurately estimate time-series for the pre- and post-event periods. We do include separability constraints to reduce the effects of the MAI phase noise, however, care must be taken to compute the constrained V-SBAS solution separately for each period. We note this requirement because the separability constraints assume a constant source geometry and, for the Father's Day event, the Kilauea volcanic system changed during course of the eruption and intrusion.

Table 7.1: Summary of ALOS PALSAR data at Kilauea Volcano, Hawaii.

| $k$ | Frame | Track | $\varphi_k$ | $\theta_k$ | Orbits ($N_k$) | Interferograms ($M_j$) | |
|---|---|---|---|---|---|---|---|
| | | | | | | InSAR | MAI |
| 1 | 380 | 287 | $-12°$ | 21° | 15 | 81 | 73 |
| 2 | 370 | 291 | $-12°$ | 34° | 12 | 54 | 45 |
| 3 | 360 | 299 | $-12°$ | 50° | 14 | 16 | 0 |
| 4 | 3220 | 605 | $-168°$ | 21° | 16 | 90 | 60 |
| 5 | 3230 | 601 | $-168°$ | 34° | 18 | 139 | 0 |
| 6 | 3240 | 593 | $-168°$ | 50° | 13 | 69 | 0 |
| | **Total** | - | - | - | 88 | 515 | 178 |

## 7.3 InSAR and MAI Data at Kilauea

We use observations from the ALOS PALSAR sensor at Kilauea Volcano from May 26, 2006 to February 08, 2010 to estimate V-SBAS time-series of the Father's day eruption and intrusion. Of the available satellite data (Figure 2.1), we use ALOS because it has numerous observations of Kilauea and also its L-band sensor will retain higher coherence in vegetated regions. During the period of study, ALOS made observations on ascending and descending headings, at several look angles, which yielded measurements from multiple radar geometries. Table 7.1 summarizes the ALOS PALSAR data. Each ascending ($\varphi_k = -12°$) and descending ($\varphi_k = -168°$) pass is acquired in three look angles, which defines a total of $K = 6$ geometries. Considering both the MAI and InSAR measurements from Section 6.3, there are a total of $J = 2K$ sets of data.

Interferometric pairs cannot be formed between different imaging geometries, therefore we process all sets of data independently. For the $j^{th}$ set, in the $k^{th}$ geometry, we can form $M_j = N_k(N_k - 1)/2$ interferograms, however, this number is typically reduced by the small-baseline requirements of SBAS. Specifically, we set a baseline threshold of 2 km and do not process interferograms if $B_\perp > 2$ km. The effects can be seen in Figure 7.2, where we give examples of time-baseline plots that show the space-time distribution of the processed InSAR pairs. Here the see that there are fewer observations before the event and that the baseline threshold results in clusters of small baseline pairs. The time-baseline plots also reflect interferograms that were excluded for low coherence or excessive phase artifacts. These omitted

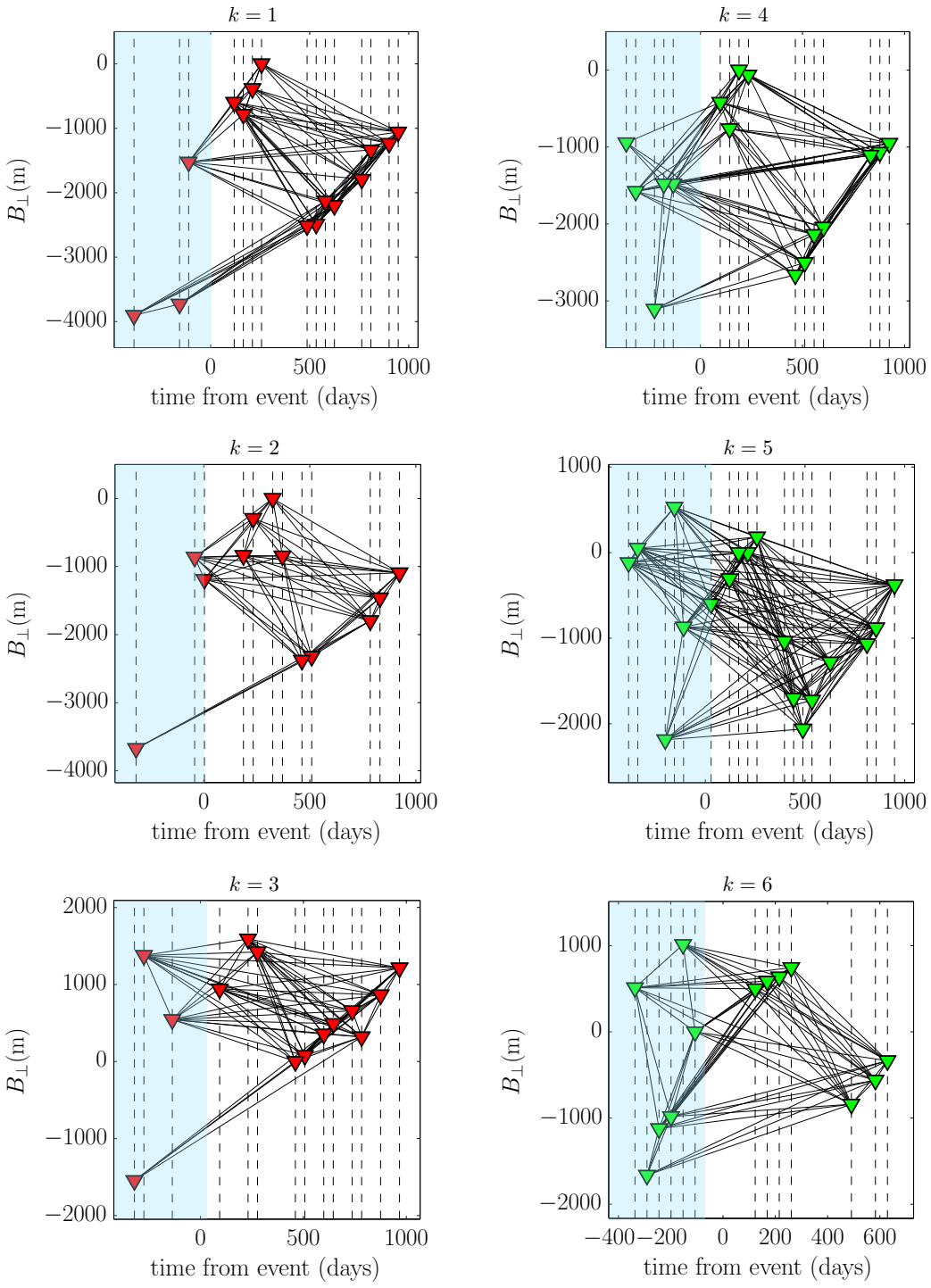


Figure 7.2: Time-baseline plots for the LOS ALOS data in Table 7.1.

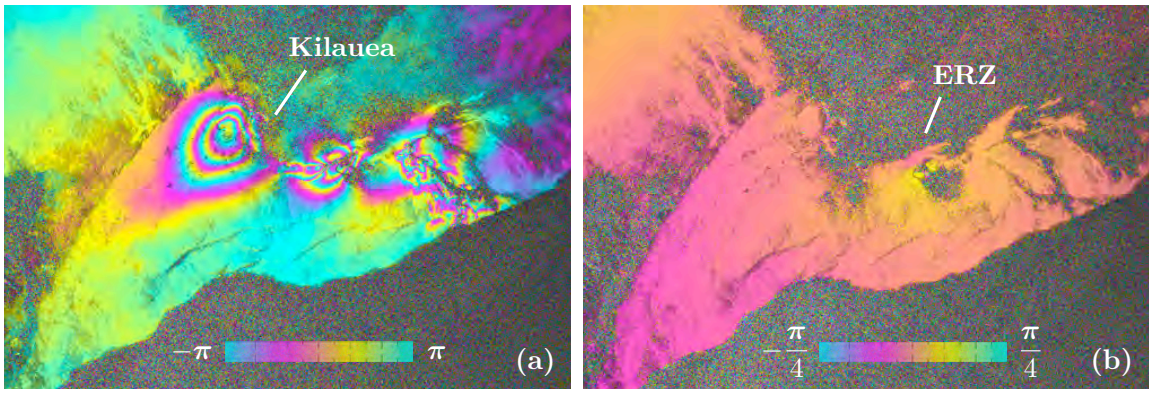


Figure 7.3: Geocoded ALOS interferograms on frame 380, track 287 from (a) InSAR, with phase wrapped from $\pm\pi$ and (b) MAI, with phase wrapped to $\pm\pi/4$. The MAI interferogram has lower sensitivity to deformation, with less phase change for the same observed deformation.

pairs typically had large temporal baselines that reduced the overall coherence or atmospheric phase screens that obscured the deformation phase. Thresholding reduces noise in our measurement vector, however, it also limits the connected SAR scenes, which will reduce the rank of the V-SBAS system matrix. The total number of valid interferograms for each set of data is represented by $M_j$ in Table 7.1.

We process interferograms according to the methods described in Chapters 3 and 4, for a total of 515 LOS measurements at each pixel. Each geometry is processed independently to its own common reference orbit, therefore we must first geocode each interferogram to align the measurements on a common geodetic grid. We use the efficient method in Chapter 5 to geocode all 515 interferograms. Before geolocation, we multilook each interferogram to reduce high spatial frequency noise and then process to a 90 m posting. This ground resolution is coarse compared to the SLC pixel spacing, but assuming that the deformation field is dominated by long spatial wavelengths, a higher number of looks is advantageous in reducing phase noise. An example interferogram is shown in Figure 7.3a, where deformation fringes are clearly visible at the Kilauea caldera and along the ERZ.

MAI interferograms were processed according to Section 2.5.2, where we formed the forward and backward interferograms using a normalized squint of $n = 0.5$ and

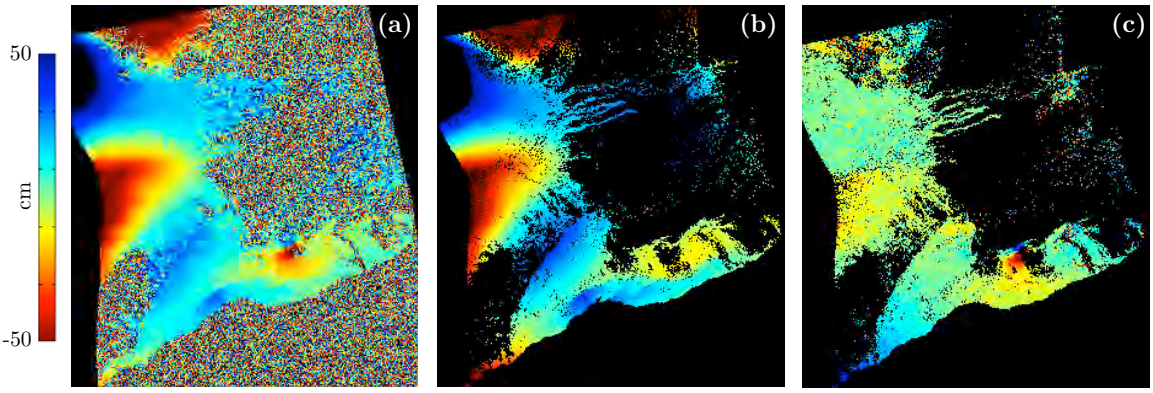


Figure 7.4: Example of MAI phase ramp removal where the (a) original interferogram was corrected by estimating a (b) phase distortion surface and subtracting it to form a (c) flattened MAI interferogram.

an effective antenna length of $l = 8.9$ m. An example MAI interferogram is shown in Figure 7.3b, where we see that even with half aperture splitting, the observed phase is much less than in a traditional interferogram. We could increase sensitivity by making $n$ larger, although this would reduce the SNR and raise the noise floor. The normalized squint of 0.5 represents half-aperture splitting, which gives a compromise between phase uncertainty and sensitivity (Bechor & Zebker, 2006). We also removed the MAI flat-Earth and topographic phase distortions with the estimation approach presented in Jung et al. (2009). These distortions were quite large, and over the set of MAI interferograms, estimated phase distortions were as high as 250 cm. An example of residual phase correction is shown in Figure 7.4, where the estimated and removed phase distortion surface is large, with peaks around 50 cm.

Removing ramps and residual topographic phase was critical in producing viable MAI interferograms, however, there were many instances where the approach in Jung et al. (2009) failed to completely flatten the image. Often the residual phase errors had magnitudes many times greater than that of the expected deformation. In these cases, we removed the noisy interferograms from the V-SBAS measurement vector. Hu et al. (2012) suggest that these residual errors may be due to ionospheric effects and they present an approach for additional corrections. In this study, we ignore atmospheric effects, and rather than handpick interferograms that appear to be valid,

we simply omit the MAI geometries that exhibited obvious large-scale errors in the majority of the data. These omissions are reflected in Table 7.1, where $M_j = 0$. In total, there were 178 valid MAI interferograms.

Another motivation for omitting certain MAI geometries is the spatial coverage of the time-series. In SBAS, we only consider pixels that are coherent across the stack, typically meeting some criterion of a minimum coherence maintained in some percentage of the interferograms (Berardino et al., 2002; Casu et al., 2011). Since the MAI data have inherently lower coherence, the valid SBAS region will be smaller, which limits the number of pixels at which time-series are estimated. Figure 7.1 shows the SBAS coherent regions for the InSAR data and also for the combined set of InSAR and MAI. It is clear that using MAI reduces the number of coherent SBAS pixels, and in an effort to minimize the loss of spatial coverage, we also omitted MAI geometries with small areas of sustained coherence. Our algorithm could be improved by letting the number of data sets vary at each pixel, but the missing data serve to illustrate the effectiveness of our approach when the epochs are poorly constrained.

## 7.4 V-SBAS Results and Validation

We validate results of the V-SBAS algorithm by comparison with the GPS network in Figure 7.1. These stations are maintained by the Hawaii Volcano Observatory and provide continuous measurements before and after the Father's Day event. In Section 7.4.1, we verify separability and the constant direction constraints with a PCA of the GPS data. In Sections 7.4.2 and 7.4.3, we compute the constrained and unconstrained time-series and evaluate errors relative to GPS. We see that the pre- and post-event periods at Kilauea do follow a constant direction of deformation, and that the constrained V-SBAS solution reduces errors in the northward time-series.

### 7.4.1 Separability from PCA of GPS Data

Our derivation of separability in Section 6.5.1 assumed a constant source geometry, with time-varying expansion and contraction of the magma chamber. The volcanic

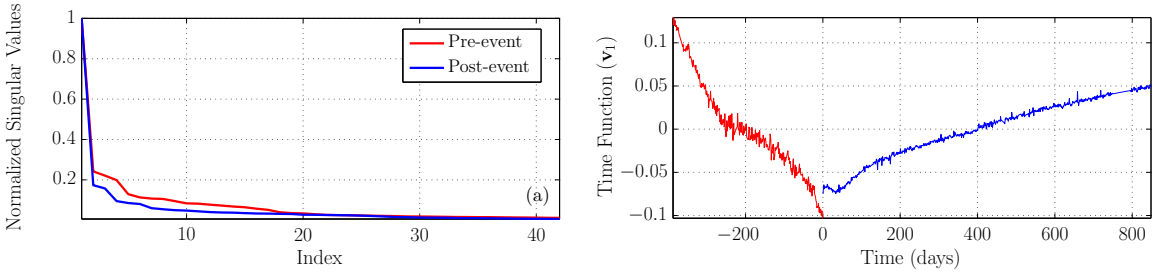


Figure 7.5: PCA decomposition of Kilauea GPS, showing (a) the normalized singular values, before and after the event, and (b) the principal time function that governs the displacement of each station.

system at Kilauea is much more complex than this simple source model, however, from Section 6.5.2, we can use a PCA of the GPS data to test if separability does apply, even when the source is unknown. For our analysis, we assume that the source geometry changed during the Father's Day eruption and intrusion, but stayed relatively constant during the slowly deforming, pre- and post-event periods. Therefore, we test for separability by analyzing the GPS data with separate PCAs, which we compute by splitting Equation 6.29 column-wise into matrices representing the time-series before and after the event. This approach is necessary because it decouples the pre- and post-event periods and allows for independent directions of deformation.

Figure 7.5a shows the singular values for each PCA and Figure 7.5b shows the time functions for the principal directions. In Equation 6.29, these values are denoted by $s_i$ and $\mathbf{v}_1$, respectively. During each of the pre- and post-event periods, the PCA was dominated by a single principal component. The second singular value is larger for the pre-event period, but this is due in part to a shorter interval of analysis, which caused the data to be more clustered. In both cases, however, the singular value spectrum drops off rapidly, indicating that Equation 6.30 is a reasonable approximation to the data. This is further seen in Figure 7.6a, where scatter plots of the GPS show regions of high correlation that are well approximated by the first principal component. From Equation 6.24, a constant derivative or linear relationship in the plots is equivalent to a constant velocity ratio, which signifies a sustained direction of deformation.

Figure 7.6a also illustrates the importance of analyzing the pre- and post-event

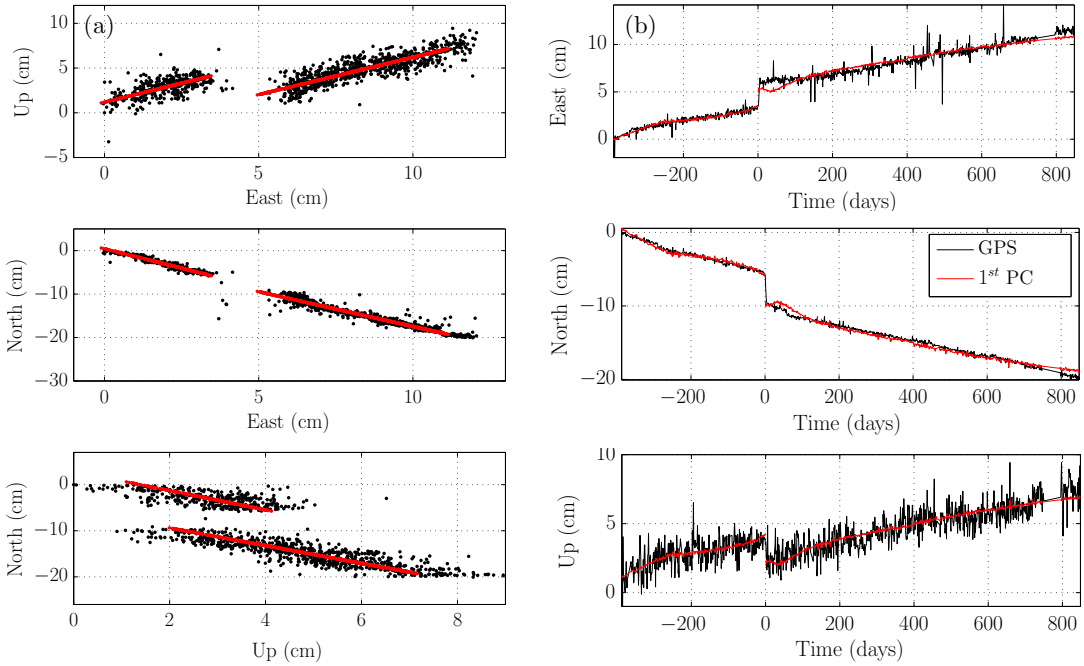


Figure 7.6: (a) Scatter plots of GPS and the first principal component at the KAEP station. (b) GPS time-series at KAEP compared to the reconstruction from only the first principal component.

periods separately. In particular, the large displacements at the time of the event cause offsets in the scatter plots. When the direction changes during the event, the two regions are no longer linearly related and if we approximate with a single principal component, it will be a poor fit individually to the two disjoint regions. This can be seen clearly in the north-up scatter plot, where the components deform disproportionately during the event and then resume in a similar direction.

Another motivation for a separate analysis is the potential for the direction to permanently change after the event. This would be reflected by a slope difference between the two correlated regions, and again, a single component would be a bad approximation. Figure 7.1 shows the principal component directions at each station, which are represented by $\mathbf{u}_1$ in Equation 6.29. The directions remain constant near the coast, but at Kilauea and the ERZ, they change after the Father's Day event. This behavior would not have been captured without using separate PCAs.

To further verify separability, we reconstruct the time-series using Equation 6.30 and re-add the previously subtracted row-by-row means. Note that in this reconstruction, the direction is fixed by $\mathbf{u}_1$, but the temporal variation is controlled by $\mathbf{v}_1$ (Figure 7.5b). As a result, even though the individual components are linearly related, there are no linear restrictions on the temporal evolution of the time-series. An example is given in Figure 7.6b, where the reconstruction agrees closely with the original GPS signal. Overall, the single component reconstruction had an RMS error of 7 mm, computed across all stations. The dominant singular value and the low error in the time-series approximations make a strong argument in support of separability. Furthermore, since the GPS network covers the majority of the region of study (Figure 7.1), we assume that this condition holds for all pixels, justifying the use of constant direction constraints to refine the V-SBAS solution.

### 7.4.2 Unconstrained V-SBAS Time-Series

For the initial unconstrained solution, we use Equation 6.18 to estimate vector time-series at all coherent pixels in Figure 7.1. The system of equations was overdetermined with $\tilde{\mathbf{G}} \in \mathbb{R}^{693\times261}$, but rank deficient as $\text{rank}(\tilde{\mathbf{G}}) = 107$. In order to view the effects

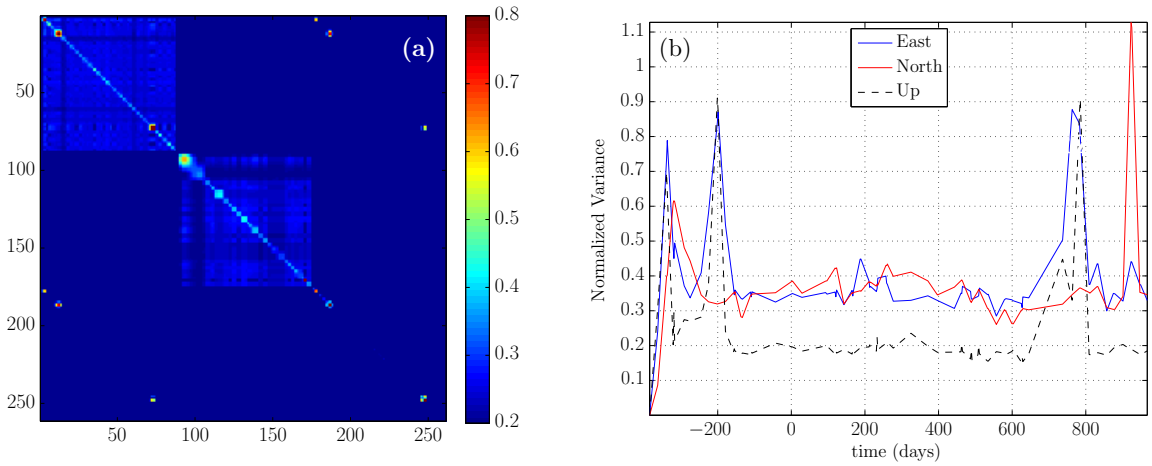


Figure 7.7: (a) Normalized V-SBAS covariance matrix and the (b) diagonal vector split into normalized ENU time-series variances.

of the pseudoinverse solution, we compute the normalized time-series covariance from Equation 6.21. Figure 7.7a shows the normalized model covariance matrix and Figure 7.7b shows the diagonal, split into ENU vectors. The vectors illustrate how unit variance errors are scaled from the input data vector to the output time-series. We see that most values are well below one, which indicates that errors will be reduced in our V-SBAS solution. The expected east and north variances appear to be equivalent, however seeing that these curves are normalized, they do not take into account the the different levels of error in each data set. Since the MAI data primarily constrain the northward component, we anticipate errors less than the theoretical 10-12 cm, but greater than those of the InSAR-constrained east and up components.

Figure 7.8 shows examples of the V-SBAS time-series at two stations, one on the northern side of the ERZ (Figure 7.8a) and another near the Kilauea caldera (Figure 7.8b). The results of the initial inversion show good agreement with GPS in the east and up directions, where the RMS error, computed across all stations, was on the order of 2 cm (see Table 7.2). Additional results are given in Figure 7.9, which show deformation fields from the east and up time-series for six epochs spanning the post-event period. As supported by GPS, we see a subsidence bowl at the Kilauea caldera that indicates deflation of the summit reservoirs.

The north time-series, which came primarily from MAI, was much noisier with

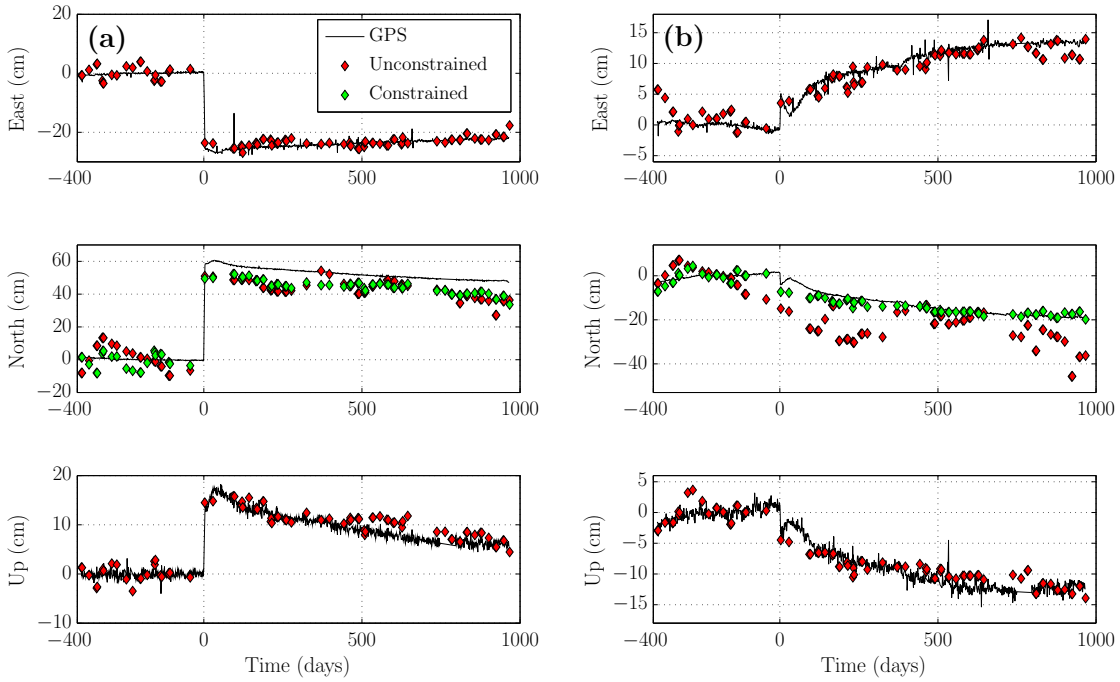


Figure 7.8: GPS and V-SBAS ENU time-series at the (a) NUPM station, on the northern side of the ERZ, and at the (b) UWEV station, located near the Kilauea caldera. Exact GPS locations are shown in Figure 7.1. Errors were reduced at both stations using the constrained inversion. RMS errors were improved by a factor of 1.4 at NUMP and 5.3 at UWEV.

Table 7.2: V-SBAS errors calculated across all GPS stations.

| **Deformation Period** | **RMS Error (cm)** | | | |
|---|---|---|---|---|
| | East | North | North (Constrained) | Up |
| Pre-event | 1.76 | 4.62 | 3.79 | 1.77 |
| Co-event | 1.33 | 3.8 | 3.65 | 1.28 |
| Post-event | 1.94 | 7.3 | 4.69 | 1.4 |
| **Complete Event** | 1.9 | 6.6 | 4.4 | 1.5 |

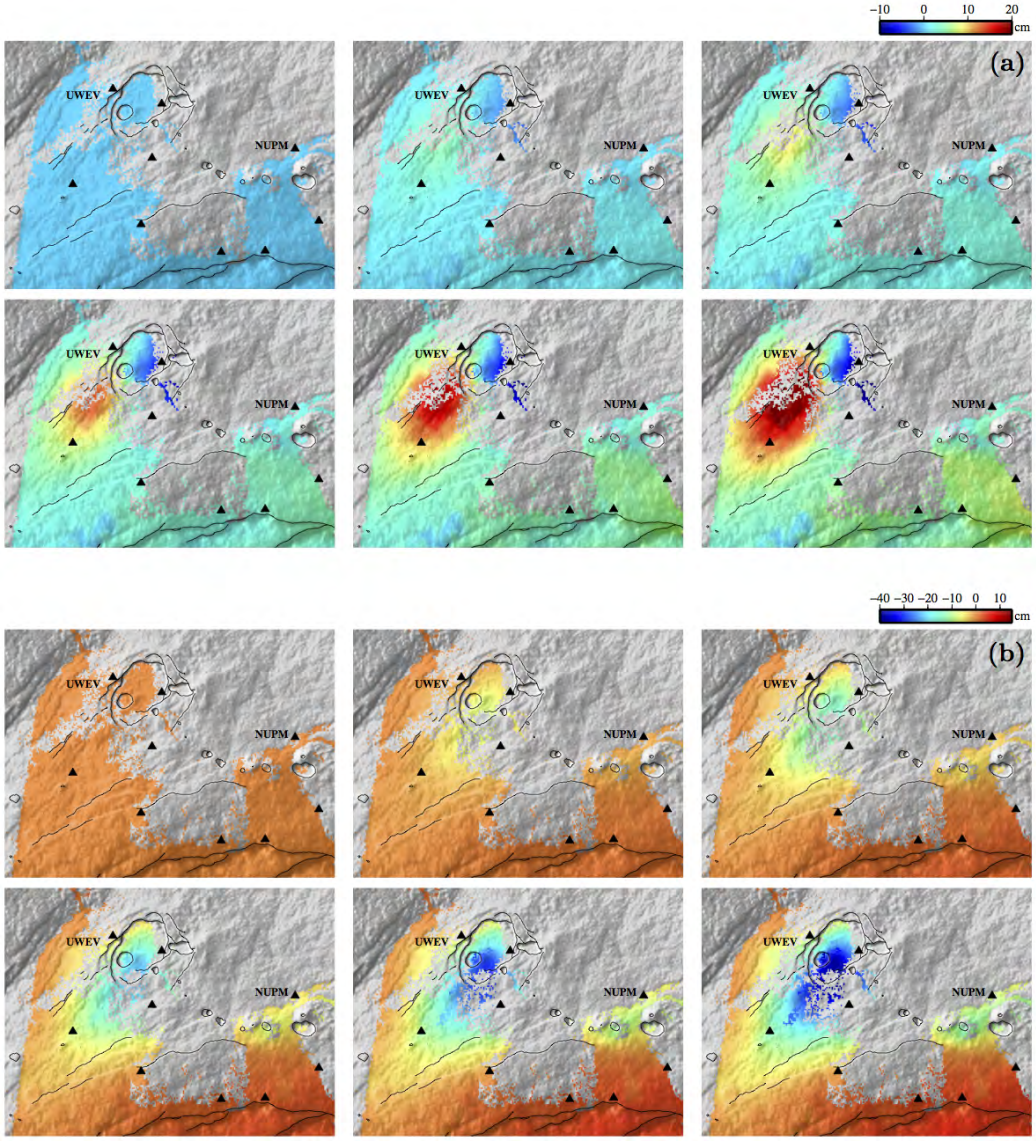


Figure 7.9: V-SBAS time-series, near the Kilauea caldera, representing the period after the Father's day event. Time-series are shown in the (a) East and (b) Up directions. Time progresses from left-to-right and spans from June 20, 2007 to January 21, 2010. Each epoch is spaced approximately 190 days apart.

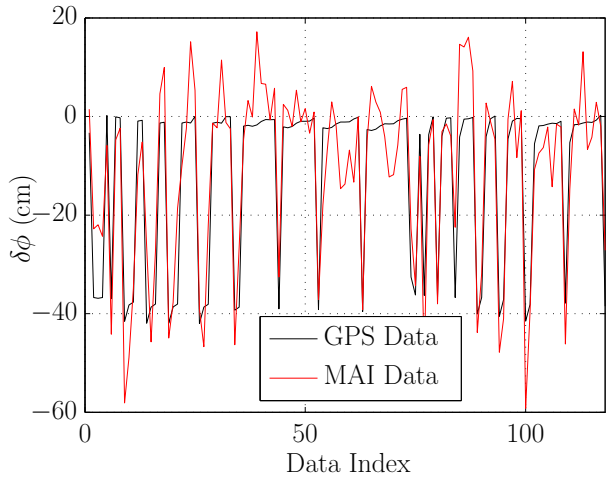


Figure 7.10: Comparison of MAI a measurement vector $\boldsymbol{\delta\phi}_j$ and measured displacements from GPS.

an overall RMS error of 6.6 cm. This result was expected and it reflects the limited accuracy of the MAI technique. An example data vector is shown in Figure 7.10, where the GPS measurements, projected onto the along-track look vector, disagree with MAI by up to 20 cm. From these errors, we expect the MAI-constrained north to be relatively noisy, but still track the GPS time-series. This was generally the case (Figure 7.8a), but in some instances, the unconstrained solution was an overall poor fit. An example of a inaccurate estimate is shown in Figure 7.8b, where the RMS error in the north component was 11.3 cm. Additional northward results are shown in Figure 7.11a, where we see signs of the subsidence bowl, but also large artifacts to the southwest of the Kilauea caldera and at the ERZ. The results are partially due to the increased MAI phase error, however, since the artifacts are spatially correlated, it is likely that they are also related to the residual MAI phase distortions, discussed in Section 7.3.

### 7.4.3 Constrained V-SBAS Time-Series

The PCA in Section 7.4.1 suggests that the deformation before and after the Father's Day event exhibits space-time separability, which validates the use of the secondary

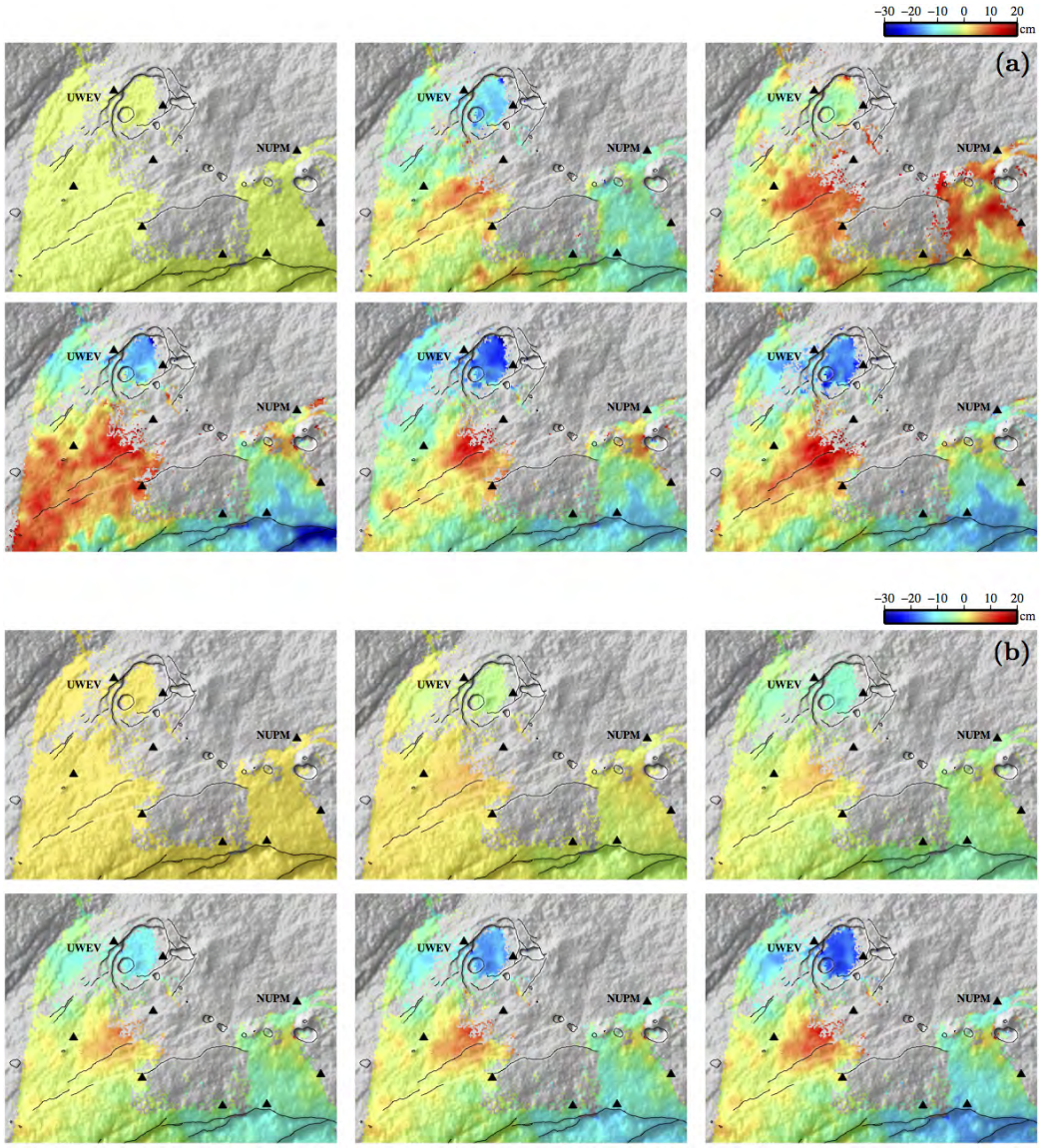


Figure 7.11: V-SBAS time-series, near the Kilauea caldera, representing the period after the Father's day event. Time-series are shown for Northern component using the (a) unconstrained and (b) constrained solutions. Time progresses from left-to-right and spans from June 20, 2007 to January 21, 2010. Each epoch is spaced approximately 190 days apart.

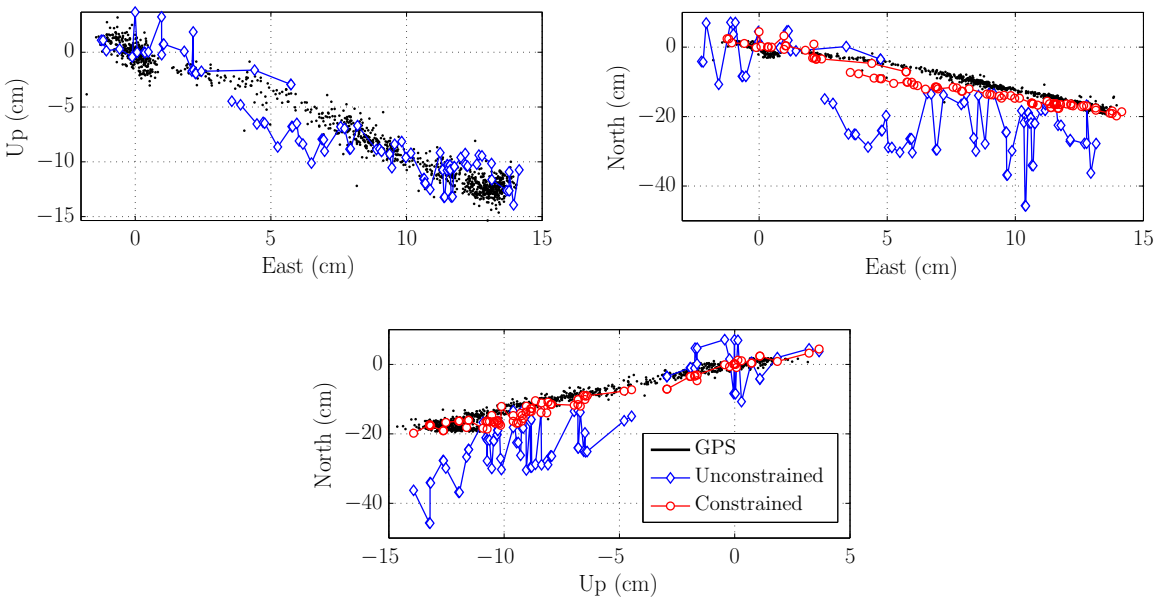


Figure 7.12: Scatter plots of GPS and V-SBAS at the UWEV station. Constrained and unconstrained V-SBAS results are given to evaluate the effectiveness of the linear approximation to the fully constrained nonlinear V-SBAS solution.

inversion in Section 6.6. From the unconstrained V-SBAS time-series, we use Equation 6.36 to solve for the pre- and post-event proportionality constants and then re-estimate the north component using Equation 6.37. The components of the new solution are constrained to be approximately linearly related, thus the V-SBAS scatter plots should exhibit the same trends as GPS.

Figure 7.12 shows example of GPS and V-SBAS scatter plots at the UWEV station. Like the plots in Figure 7.6, the GPS components are highly correlated, indicating a constant direction of deformation. The unconstrained V-SBAS solution shows a similar relationship in the east and up, however, the northward component is erratic and does not match GPS. The effects of these errors are evident in the time-series shown in Figure 7.8b, where the UWEV time-series tracks GPS in the east and up directions, but is a poor fit in the north. In order to agree with the GPS time-series in all dimensions, the V-SBAS solution must demonstrate the same linear dependence between each of the components.

The proportionality constants from Equation 6.36 define the slopes of the correlated regions in the scatter plots. These differ at each pixel, and are independent for pre- and post-event periods. By constraining the ratio of the V-SBAS velocities to approximate these slopes, we are fixing the direction of deformation, which reduces the influence of noisy data. As in Section 6.6, we assume that the east and up time-series are accurate from the unconstrained inversion and we use these components to estimate the proportionality constants. We justify this assumption by referring to Figure 7.12, where east and up components approximate the linear GPS scatter plots, and Table 7.2, where the overall east and up station errors are low.

Constrained results are given in Figure 7.12, which shows higher correlation between the V-SBAS components and a nearly constant slope that matches GPS. The effects of the constrained solution are also illustrated in the north component of the time-series in Figure 7.8b, where V-SBAS now tracks GPS. We also note that although the individual components are linearly related, the separability constraints do not impose limitations of linear deformation or constant velocities. The ratio of the velocities are constant, but the time-series evolves arbitrarily with the time function $\mathbf{v}_1$.

Table 7.2 gives the updated error statistics for the constrained northward time-series. Globally, the constrained solution reduced errors with a overall drop of 2 cm RMS, however, a single overall value underplays the achieved accuracy gains. At some stations, the benefits of the constrained inversion were substantially higher. For example, Figure 7.8a was improved by 3.8 cm, but Figure 7.8b saw a much larger reduction in error from 11.3 to 2.1 cm. This is also illustrated Figure 7.13, where we compare the GPS and V-SBAS time-series for each epoch, across all stations. Considering to the northward component, the cluster of points for the constrained inversion is tighter and several points with errors as large as 20 cm have been drastically reduced. Another example is shown in Figure 7.11b, which gives the constrained deformation fields at six epochs during the post-event period. Compared to the unconstrained results, the subsidence bowl is more clear and the artifacts to the southwest of the Kilauea calder and at the ERZ are less apparent. Visually, we see more errors in the unconstrained solution, however, since many of these pixels are not covered by GPS,

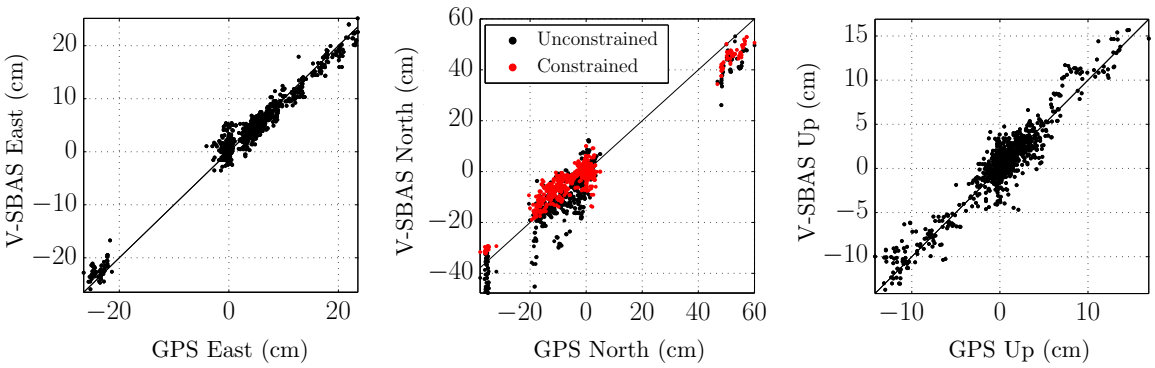


Figure 7.13: Comparison of V-SBAS and GPS deformation at all epochs for stations corresponding to coherent pixels.

our estimate of the total error reduction is biased.

In order to estimate the co-event errors, we define the displacement as the offset between quadratic fits to the pre- and post-event periods. These fits are less sensitive to the time-series noise, thus the constrained solution gives only a marginal improvement over the initial estimate (Table 7.2). Figure 7.14 shows the co-event displacement fields, where we see clear signs of dilation at the ERZ and deflation at the Kilauea caldera. The northward deformation is dominant at the ERZ, where our results show a maximum opening of 1.75 m in the northwest direction. This is less than the AZO measurements of 1.9 m reported by Sandwell et al. (2008), but these results are not too surprising, as we are missing coherent coverage in the region of maximal deformation, located approximately between the NUPM and KTPM GPS stations.

## 7.5 Summary

We applied our technique to data acquired over the Father's Day intrusion and eruption at the ERZ of Kilauea Volcano, using ALOS PALSAR data from six radar geometries. We estimated vector time-series at all epochs, which increased the temporal resolution and dimensionality over that of a single SBAS geometry. We found that excessive phase errors limited the number of useable MAI interferograms, which

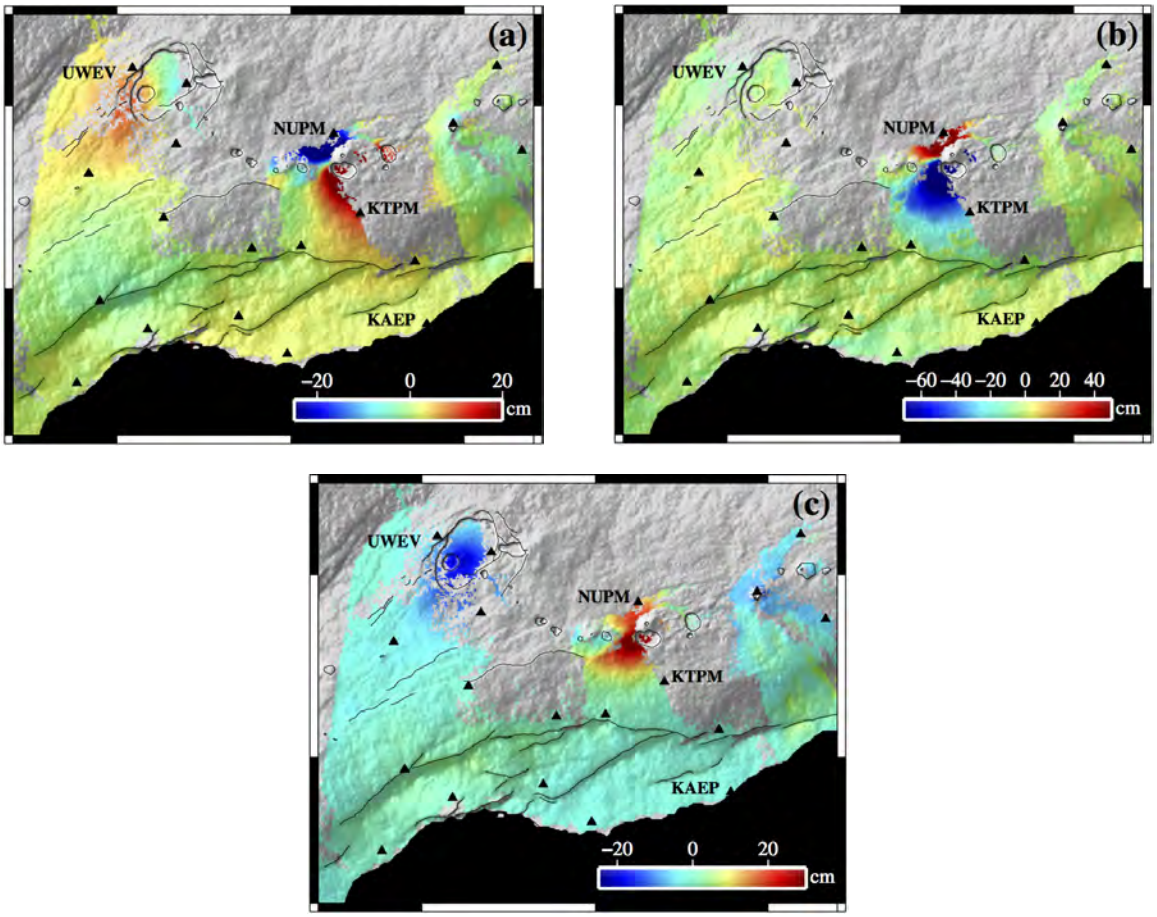


Figure 7.14: Co-event displacement fields from the constrained V-SBAS algorithm in the (a) east, (b) north, and (c) upward directions.

further reduced the rank of the V-SBAS system of equations. We also found that the higher phase noise of MAI limited the coherent spatial coverage of the time-series.

The initial unconstrained solution produced the most accurate results in the east and up directions, with RMS errors on the order of 2 cm. The northward component was noisier, with RMS errors of 6.6 cm. Following a PCA on existing GPS data, we showed that the Kilauea data set does exhibit a constant direction of deformation, but that this direction can change before and after the event. The constant direction was identified as high correlation between the time-series components, indicating a constant ratio of velocities. We showed that the V-SBAS time-series not following

this trend were a poor fit to the GPS. After applying separability, we found that solutions were effectively constrained to have an approximately constant direction of deformation and that the overall time-series accuracy was improved. Average errors across all GPS stations were reduced to 4.4 cm, but in some instances, individual station errors were reduced by as much as a factor of 5. In addition, spatial trends in the deformation field also matched the expected patterns of the Father's Day event, further validating our results.

Our approach is presented in its most simplistic form to illustrate the effectiveness of V-SBAS without excessive post-processing. The results are given with no spatial or temporal filtering. Additional considerations could be taking into account to mitigate atmospheric or topographic errors (Berardino et al., 2002). These advanced applications of SBAS would improve results and are easily incorporated into the proposed algorithm. Additional efforts could be made to reduce the residual MAI phase distortions and increase the amount of along-track measurements. The existing literature on removing these trends has been paramount in producing accurate time-series, but in dealing with hundreds of interferograms, it is inevitable that these approaches would at times fail. In this research, the lack of full MAI data sets serves to demonstrate the effectiveness of V-SBAS even with limited measurements. Finally, we remark that the equations are general, in that they can be used to combine data from multiple sensors or even use AZO along with or in place of MAI. Combining measurements would increase temporal coverage and potentially reduce rank deficiency. However, in spite of these directions for future improvements, the new algorithm provides an accurate, efficient, and flexible means to estimate vector deformation time-series.

# Chapter 8

# Summary and Conclusions

## 8.1 Summary

The traditional InSAR technique provides spatially dense observations of large areas, but it is limited in its sparse temporal sampling and by one-dimensional measurements in the LOS direction. Since crustal deformation is dynamic, with surface displacements occurring in all directions and evolving in time, these limitations reduce the effectiveness of InSAR to fully characterize the sources of deformation. The SBAS technique aims to increase the temporal resolution by combining several observations to estimate a time-series over an extended period, however, as the measurements are in the LOS, the SBAS time-series are also limited to this direction. Mutlidimensional approaches combine InSAR from several LOS geometries and also use along-track interferometry to estimate the full three-dimensional vector deformation field, although these approaches still only measure displacements between two points in time. The current literature reflects some efforts to combine multidimensional and multitemporal approaches, but these studies are limited to two-dimensional time-series in areas with large deformation signatures. A full three-dimensional vector InSAR time-series solution would increase our knowledge of the deformation environment and would lead to less ambiguity in the estimate of source parameters.

This thesis bridges the gap between multitemporal and multidimensional techniques by extending SBAS to a vector formulation that we referred to as V-SBAS.

Our approach estimates the full three-dimensional time-series and by exploiting redundancy in the interferometric measurements, we can apply V-SBAS to areas with relatively small deformation. By combining LOS observations from several geometries, we effectively increase the temporal resolution over that of a single geometry and broaden the time-series to observe the evolution of the full ENU deformation field. We divided this thesis into two main areas: motion compensation data processing and vector time-series estimation. Our discussion of motion-compensated processing is motivated by the need for high quality measurements, efficient processing of large stacks of interferograms, and geodetic accuracy to combine the measurements on a common grid. The principal contributions of this work are summarized below:

- Development of a geodetically accurate motion compensation radar processor that improves computational efficiency over traditional range-Doppler processors and produces interferograms in a common, well-known coordinate system.
- Identification of processor-induced spectral shifts that reduce coherence for large motion compensation baselines and formulation of processor modifications to preserve coherence at arbitrary imaging geometries.
- Development of a new approach to geolocation that utilizes the simplified spherical geometry of our motion compensation processor to efficiently and accurately resample radar images to an orthonormal map projection.
- Extension of existing one-dimensional time-series techniques to incorporate measurements from multiple radar geometries to estimate three-dimensional vector deformation time-series.
- Formulation of the concept of space-time separability to constrain the relative motion of orthogonal components in vector time-series. Our approach outlines a new method to verify separability through a PCA of GPS data and presents an efficient linear approach to approximately enforce these constraints.
- Application of our vector time-series algorithm to the 2007 Father's Day eruption and intrusion at the Kilauea Volcano, Hawaii, where results show errors on the order of 2-4 cm.

Chapters 3-5 described our new approach to motion compensation processing of spaceborne InSAR data. Chapter 6 detailed the geometries of LOS and MAI measurements, describe the V-SBAS algorithm, and introduced a new approach reduce the influence of noise by constraining the vector direction of deformation. Finally, Chapter 7 gave results of a case study of the 2007 Father's Day eruption and intrusion at the Kilauea Volcano, Hawaii, where we saw overall errors on the order of 2 cm in the east and up directions and 4 cm in the north.

## 8.2 Future Work and Improvements

Just as this thesis represents a step forward, the field of radar interferometry will continue to evolve. In the course of this work, we have identified several areas of further research that build on our results and that may improve our approach. On the topic of data processing, our main limitation was measurement quality, therefore we highlight the following as areas of future work.

- DEM assisted coregistration: During coregistration, we ignore topography and resample the slave SLC with a two-dimensional offset field. In areas of steep relief, this surface may not accurately capture the local offsets, which will reduce coherence. DEM assisted coregistration (Nitti et al., 2011) overcomes this limitation, however, most processors do not incorporate this approach due to computational complexity. Given the simplified motion compensation geometry, it is feasible that some efficient form of this approach could be incorporated into our processor to further improve interferometric coherence.

- Baseline variation over a patch: In Section 3.4.3, we note that the motion compensation baseline is assumed to be constant in both azimuth and range on a patch-by-patch basis. This assumption is sufficient to produce well focused interferograms, however, it is an approximation that can lead to defocus. We choose this approach because of the frequency domain implementation, although a spatially varying calculation of the motion compensation baseline may improve image quality.

- MAI detrending: Phase trends were the largest source of error in the MAI interferograms. MAI is a relatively new technique, and the exact sources of these phase distortions are just now being understood (Jung et al., 2009; Hu et al., 2012). More research is needed into the exact phase relationships between the forward and backward MAI beams in order to fully understand and remove the existing phase distortions.

On the topic of vector time-series, we highlight the following as areas of future work.

- Data fusion: The V-SBAS approach is more accurate as the number of interferograms increases. In this work, we only use observations for ALOS PALSAR, however, several other sensors were operational during 2007 (Figure 2.1). A straight forward extension would combine data from multiple sensors to increase the spatial and temporal coverage of our time-series.

- Atmospheric filtering: Delays from the ionosphere and troposphere appear as high frequency noise in the time-series estimates. Current solutions incorporate low-pass filters into the time-series processor to remove these effects, however, these approaches are ad-hoc and little information exists on the appropriate characteristics of these filters. Our results contain atmospheric noise, which should be removed to further improve accuracy.

- Separability constraints: In Section 6.6 we discuss a linear approximation to the nonlinear separability constraints. There are several existing methods to solve the nonlinear problem (Aster et al., 2005), but these approaches are computationally expensive and are undesirable for the millions of pixels in an InSAR image. Efficient methods to impose the exact separability constraints could prove to be helpful and may lead to further constraints that are unique to the vector time-series problem.

- Further case studies: We successfully applied V-SBAS at the Kilauea Volcano, Hawaii. However, we should fully test our approach by applying it to different sources of deformation. For example, a study at the SAF would verify V-SBAS applied to a seismic source and would further assess its ability to measure small

deformation with a large northward component. In addition, results of a source parameters estimation should be compared between one-dimensional approaches and V-SBAS to fully understand the benefits of vector time-series.

## 8.3 Conclusions

In Chapter 3 we demonstrated our motion compensation technique for spaceborne data and showed that processing in the motion compensation geometry is greatly simplified. This technique depends on the accuracy of orbit information, but given the advances of modern sensors, we have shown that motion compensation processing is a viable approach to produce high quality interferometric products. Chapter 4 described spectral shifts in motion compensation processing and demonstrated how these will lead to a loss in coherence for large motion compensation baselines. We developed processor modifications that restored coherence, allowing motion compensation to be applied to acquisitions in arbitrary geometries. These corrections are important when processing large sets of time-series data to a common reference orbit, and our V-SBAS results would have been compromised without them.

Chapters 6 and 7 outlined the V-SBAS approach and demonstrated results of a case study at the Kilauea Volcano, Hawaii. Initial results showed good results of 2 cm error in the east and up directions, with larger errors of 6 cm in the north. We developed theoretical expressions for the MAI phase uncertainty, illustrating that the expected MAI phase noise will be significantly worse than InSAR. These findings were verified by comparison of MAI measurements with those expected from GPS. We also found that large residual phase distortions corrupted some of the MAI interferograms, which lead to us omit large portions of the available data. In order to reduce the effects of MAI phase noise, we derived a new method of constraining the vector time-series that was based on separability of the spatial and temporal components of the time-series. These constraints assumed a constant direction of deformation, which we verified through a PCA on existing GPS time-series at Kilauea. Since the MAI data primarily defined deformation in the north, we re-estimated the northward time-series using the separability constraints. The refined solution reduced the overall average

errors to 4 cm, but at some stations, the gains were much larger, reducing errors by 10-20 cm. Our results show that the MAI data is the limiting factor in vector time-series, but with our separability constraints, we can estimate time-series with errors that are much less than those expected from a single interferometric pair.

# Appendix A

# Motion Compensation Phase Expansion

In Chapter 4, we discuss how the range variation of the motion compensation phase introduces a shift and smearing of the range spectrum, and how the exact dependence on $\rho$ is difficult to see from 3.30. In this appendix, we use a Taylor series expansion to reveal the first and second order terms of the function, so that the results can be used to derive the approximate bandwidth and center frequency of the motion compensation phase correction function.

Starting with the expression for the motion compensation correction phase

$$\phi_m(\rho) = \frac{4\pi}{\lambda}\left(\rho'(\rho) - \rho\right) , \tag{A.1}$$

we write the Taylor series expansion about the mid-swath range $\rho_0$

$$\phi_m(\rho) \approx \frac{4\pi}{\lambda}\left(\phi_0 + \phi_1\left(\rho - \rho_0\right) + \phi_2\left(\rho - \rho_0\right)^2\right) , \tag{A.2}$$

where

$$\phi_0 = \phi_m(\rho)\Big|_{\rho=\rho_0} \tag{A.3}$$

$$\phi_1 = \frac{d\phi_m(\rho)}{d\rho}\Big|_{\rho=\rho_0} \tag{A.4}$$

$$\phi_2 = \frac{1}{2}\frac{d^2\phi_m(\rho)}{d\rho^2}\Big|_{\rho=\rho_0} . \tag{A.5}$$

To be consistent with our formulation of the reference geometry, we should compute the derivatives based on the curved-Earth model in Chapter 3, however, the equations in the spherical geometry are complicated and even the first derivative will do little to simplify our expression. Instead, we use the flat-Earth approximation in Figure 4.1 and note that Prati and Rocca (1993) and Gatelli et al. (1994) use this same approximation in their study of the SAR wavenumber shift. From the flat-Earth model, we use the following equations in our derivation of the Taylor series coefficients

$$\rho'(\rho) = \sqrt{(y-d)^2 + (h')^2} \tag{A.6}$$

$$y = \sqrt{\rho^2 - h^2} \tag{A.7}$$

For the zeroth order coefficient, we evaluate A.3 at $\rho_0$ and write

$$\phi_0 = \rho'_0 - \rho_0 \, , \tag{A.8}$$

where $\rho'_0$ is the actual range at the mid-swath position of the reference orbit,

$$\rho'_0 = \sqrt{(y_0-d)^2 + (h')^2} \, , \tag{A.9}$$

and $y_0$ is the mid-swath distance in the ground plane. For the first order coefficient,

$$\phi_1 = \frac{d\phi_m(\rho)}{d\rho}\Big|_{\rho=\rho_0} = \frac{\rho_0 \ (y_0-d)}{y_0\sqrt{(d-y_0)^2 + (h)'^2}} - 1 \, , \tag{A.10}$$

which we can simplify as

$$\begin{aligned} \phi_1 &= \frac{\rho_0\ (y_0 - d)}{y_0\,\rho_0'} - 1 \\ &= \frac{\sin\theta_0'}{\sin\theta_0} - 1 \\ &= \frac{\sin\theta_0' - \sin\theta_0}{\sin\theta_0}\,, \end{aligned} \tag{A.11}$$

where $\theta_0$ and $\theta_0'$ are the look angles at the mid-swath position. Next, defining

$$\Delta\theta_0 = \theta_0 - \theta_0' \tag{A.12}$$

and using the approximation from Prati and Rocca (1993)

$$\frac{\theta_0 + \theta_0'}{2} \approx \theta_0 \approx \theta_0'\,, \tag{A.13}$$

we write

$$\begin{aligned} \sin\theta_0' - \sin\theta_0 &= 2\cos\left(\frac{\theta_0 + \theta_0'}{2}\right)\sin\left(\frac{\theta_0 - \theta_0'}{2}\right) \\ &\approx -\Delta\theta_0\cos\theta_0 \end{aligned} \tag{A.14}$$

and simplify $\phi_1$ as

$$\phi_1 \approx -\frac{\Delta\theta_0\cos\theta_0}{\sin\theta_0} = -\frac{\Delta\theta_0}{\tan\theta_0}\,. \tag{A.15}$$

Finally, noting that

$$\frac{b_{\perp,0}}{\rho_0'} = \sin(\theta_0 - \theta_0') \approx \Delta\theta_0\,, \tag{A.16}$$

we write the first order coefficient in terms of the perpendicular motion compensation baseline as

$$\phi_1 \approx -\frac{b_{\perp,0}}{\rho_0'\tan\theta_0}\,. \tag{A.17}$$

For the quadratic term, we evaluate the second derivative at $\rho_0$

$$\begin{aligned}
\left.\frac{d^2\phi_m(\rho)}{d\rho^2}\right|_{\rho=\rho_0} &= \frac{{\rho_0}^2\left(d-\sqrt{{\rho_0}^2-h^2}\right)}{({\rho_0}^2-h^2)^{\frac{3}{2}}\sqrt{\left(d-\sqrt{{\rho_0}^2-h^2}\right)^2+h'^2}} \\
&- \frac{d-\sqrt{{\rho_0}^2-h^2}}{\sqrt{{\rho_0}^2-h^2}\sqrt{\left(d-\sqrt{{\rho_0}^2-h^2}\right)^2+h'^2}} \\
&- \frac{{\rho_0}^2}{(h^2-{\rho_0}^2)\sqrt{\left(d-\sqrt{{\rho_0}^2-h^2}\right)^2+h'^2}} \\
&+ \frac{{\rho_0}^2\left(d-\sqrt{{\rho_0}^2-h^2}\right)^2}{(h^2-{\rho_0}^2)\left(\left(d-\sqrt{{\rho_0}^2-h^2}\right)^2+h'^2\right)^{\frac{3}{2}}} \\
&= -\frac{1}{y_0}\frac{\sin\theta_0'}{\sin^2\theta_0}+\frac{\sin\theta_0'}{y_0}+\frac{1}{\rho_0'\sin^2\theta_0}-\frac{1}{\rho_0'}\frac{\sin^2\theta_0'}{\sin^2\theta_0} \\
&= \frac{1}{\rho_0'}\frac{\cos^2\theta_0'}{\sin^2\theta_0}-\frac{1}{y_0}\frac{\sin\theta_0'}{\tan^2\theta_0}\,,
\end{aligned} \tag{A.18}$$

which leads to

$$\phi_2 = \frac{1}{2}\left(\frac{1}{\rho_0'}\frac{\cos^2\theta_0'}{\sin^2\theta_0}-\frac{1}{y_0}\frac{\sin\theta_0'}{\tan^2\theta_0}\right)\,. \tag{A.19}$$

Combining, the results, we have the constant, first, and second order coefficients that approximate the motion compensation phase correction function

$$\begin{aligned}
\phi_0 &= (\rho_0'-\rho_0) \\
\phi_1 &= \frac{\sin\theta_0'-\sin\theta_0}{\sin\theta_0} \approx -\frac{\Delta\theta_0}{\tan\theta_0} \approx -\frac{b_{\perp,0}}{\rho_0'\tan\theta_0} \\
\phi_2 &= \frac{1}{2}\left(\frac{1}{\rho_0'}\frac{\cos^2\theta_0'}{\sin^2\theta_0}-\frac{1}{y_0}\frac{\sin\theta_0'}{\tan^2\theta_0}\right)\,.
\end{aligned} \tag{A.20}$$

# References


Agram, P. S., Jolivet, R., Riel, B., Lin, Y. N., Simons, M., Hetland, E., ... Lasserre, C. (2013). New radar interferometric time series analysis toolbox released. *Eos, Transactions American Geophysical Union*, *94*(7), 69–70.

Amelung, F., Jónsson, S., Zebker, H., & Segall, P. (2000). Widespread uplift and trapdoorfaulting on galapagos volcanoes observed with radar interferometry. *Nature*, *407*(6807), 993–996.

Aster, R. C., Borchers, B., & Thurber, C. (2005). *Parameter estimation and inverse problems*. Burlington, MA: Elsevier.

Baker, S., & Amelung, F. (2012). Top-down inflation and deflation at the summit of kilauea volcano, hawaii observed with insar. *J. Geophys. Res.*, *117*(B12).

Bamler, R. (1991). Doppler frequency estimation and the cramer-rao bound. *Geoscience and Remote Sensing, IEEE Transactions on*, *29*(3), 385–390.

Barbot, S., Hamiel, Y., & Fialko, Y. (2008). Space geodetic investigation of the coseismic and postseismic deformation due to the 2003 mw7. 2 altai earthquake: Implications for the local lithospheric rheology. *Journal of Geophysical research*, *113*(B3), B03403.

Bechor, N. (2006). *Extending interferometric synthetic aperture radar measurements from one to two dimensions*. Unpublished doctoral dissertation, Stanford University.

Bechor, N., & Zebker, H. (2006). Measuring two-dimensional movements using a single insar pair. *Geophys. Res. Lett.*, *33*(16), L16311.

Berardino, P., Bonano, M., Calo, F., Casu, F., Elefante, S., Manunta, M., ... Lanari, R. (July). Long term deformation time series: 10 years of earth observation

through envisat multi-mode asar sensor. In *Geoscience and remote sensing symposium (igarss), 2012 ieee international* (p. 1840-1843).

Berardino, P., Fornaro, G., Lanari, R., & Sansosti, E. (2002). A new algorithm for surface deformation monitoring based on small baseline differential sar interferograms. *IEEE Trans. Geosci. Remote Sens.*, *40*(11), 2375 - 2383.

Bills, B. G., & Ferrari, A. J. (1977). A harmonic analysis of lunar topography. *Icarus*, *31*(2), 244–259.

Boyd, S., & Vandenberghe, L. (2004). *Convex optimization*. New York, NY, USA: Cambridge University Press.

Bracewell, R. N. (2003). *Fourier analysis and imaging*. Springer.

Buckley, S. M. (2000). *Radar interferometry measurement of land subsidence*. Unpublished doctoral dissertation, Univ. Texas, Austin, Texas.

Bürgmann, R., Hilley, G., Ferretti, A., & Novali, F. (2006). Resolving vertical tectonics in the san francisco bay area from permanent scatterer insar and gps analysis. *Geology*, *34*(3), 221–224.

Bürgmann, R., Rosen, P. A., & Fielding, E. J. (2000). Synthetic aperture radar interferometry to measure earth's surface topography and its deformation. *Annual Review of Earth and Planetary Sciences*, *28*(1), 169–209.

Casu, F., Manconi, A., Pepe, A., & Lanari, R. (2011). Deformation time-series generation in areas characterized by large displacement dynamics: The sar amplitude pixel-offset sbas technique. *IEEE Trans. on Geosci. Remote Sensing*, *49*(7), 2752 -2763.

Cervelli, P. F., & Miklius, A. (2003). The shallow magmatic system of kilauea volcano. *US Geological Survey professional paper*, *1676*, 149-163.

Chen, C. W., & Zebker, H. A. (2002). Phase unwrapping for large sar interferograms: statistical segmentation and generalized network models. *IEEE Trans. on Geosci. Remote Sensing*, *40*(8), 1709–1719.

Costantini, M. (1998). A novel phase unwrapping method based on network programming. *IEEE Trans. on Geosci. Remote Sensing*, *36*(3), 813–821.

Cumming, I. G., & Wong, F. H. (2004). *Digital signal processing of synthetic aperture radar data: Algorithms and implementation*. Boston, MA: Artech House.

Curlander, J. C., Kwok, R., & Pang, S. S. (1987). A post-processing system for automated rectification and registration of spaceborne sar imagery. *International Journal of Remote Sensing*, *8*(4), 621–638.

Curlander, J. C., & McDonough, R. N. (1991). Synthetic aperture radar- systems and signal processing(book). *New York: John Wiley & Sons, Inc, 1991*.

Eineder, M., Balss, U., Gisinger, C., Cong, X. Y., Brcic, R., & Steigenberger, P. (2013). Recent advances in highly accurate range measurements with terrasar-x. In *Egu general assembly conference abstracts* (Vol. 15, p. 4560).

Erten, E., Reigber, A., & Hellwich, O. (2010). Generation of three-dimensional deformation maps from insar data using spectral diversity techniques. *ISPRS Journal of Photogrammetry and Remote Sensing*, *65*(4), 388-394.

Farr, T. G., Rosen, P. A., Caro, E., Crippen, R., Duren, R., Hensley, S., ... Roth, L. (2007). The shuttle radar topography mission. *Reviews of Geophysics*, *45*(2), RG2004.

Ferretti, A., Prati, C., & Rocca, F. (2001). Permanent scatterers in sar interferometry. *IEEE Trans. on Geosci. Remote Sensing*, *39*(1), 8–20.

Fialko, Y. (2004). Probing the mechanical properties of seismically active crust with space geodesy: Study of the coseismic deformation due to the 1992 m w 7.3 landers (southern california) earthquake. *Journal of geophysical research*, *109*(B3), B03307.

Fialko, Y., Sandwell, D. T., Simons, M., & Rosen, P. (2005). Three-dimensional deformation caused by the bam, iran, earthquake and the origin of shallow slip deficit. *Nature*, *435*(22), 295-299.

Fialko, Y., Simons, M., & Agnew, D. (2001). The complete (3-d) surface displacement field in the epicentral area of the 1999 mw 7.1 hector mine earthquake, california, from space geodetic observations. *Geophys. Res. Lett*, *28*(16), 3063–3066.

Fielding, E. J., Talebian, M., Rosen, P. A., Nazari, H., Jackson, J. A., Ghorashi, M., & Walker, R. (2005). Surface ruptures and building damage of the 2003 bam, iran, earthquake mapped by satellite synthetic aperture radar interferometric correlation. *Journal of geophysical research*, *110*(B3), B03302.

Fujiwara, S., Nishimura, T., Murakami, M., Nakagawa, H., Tobita, M., & Rosen, P. A.

(2000). 2.5-d surface deformation of m6. 1 earthquake near mt iwate detected by sar interferometry. *Geophysical research letters*, *27*(14), 2049–2052.

Galloway, D., Hudnut, K., Ingebritsen, S., Phillips, S., Peltzer, G., Rogez, F., & Rosen, P. (1998). Detection of aquifer system compaction and land subsidence using interferometric synthetic aperture radar, antelope valley, mojave desert, california. *Water Resources Research*, *34*(10), 2573–2585.

Gatelli, F., Guamieri, A., Parizzi, F., Pasquali, P., Prati, C., & Rocca, F. (1994). The wavenumber shift in sar interferometry. *IEEE Trans. Geosci. Remote Sens.*, *32*(4), 855 -865.

Goldstein, R. M., Barnett, T. P., & Zebker, H. A. (1989). Remote sensing of ocean currents. *Science*, *246*, 1282–1285.

Gourmelen, N., Kim, S., Shepherd, A., Park, J., Sundal, A., Bjrnsson, H., & Plsson, F. (2011). Ice velocity determined using conventional and multiple-aperture insar. *Earth and Planetary Science Letters*, *307*(12), 156 - 160.

Guillaso, S., Reigber, A., Ferro-Famil, L., & Pottier, E. (2006). Range resolution improvement of airborne sar images. *IEEE Geosci. Remote Sens. Lett.*, *3*(1), 135 - 139.

Hanssen, R. F. (2001). *Radar interferometry: Data interpretation and error analysis*. New York, NY: Springer.

Heliker, C., & Mattox, T. (2003). The first two decades of the puu oo-kupaianaha eruption: chronology and selected bibliography. *US Geol Surv Prof Pap*, *1676*, 1–28.

Hensley, S., Chapin, E., & Michel, T. (2002). Improved processing of airsar data based on the geosar processor. In *Airsar earth science and applications workshop, march.*

Hensley, S., Rosen, P., & Gurrola, E. (2000a). The srtm topographic mapping processor. In *Geoscience and remote sensing symposium, 2000. proceedings. igarss 2000. ieee 2000 international* (Vol. 3, p. 1168-1170 vol.3).

Hensley, S., Rosen, P., & Gurrola, E. (2000b). Topographic map generation from the shuttle radar topography mission c-band scansar interferometry. In *Second international asian pacific symposium on remote sensing of the atmosphere,*

*environment, and space.*

Hetland, E. A., Mus, P., Simons, M., Lin, Y. N., Agram, P. S., & DiCaprio, C. J. (2012). Multiscale insar time series (mints) analysis of surface deformation. *J. Geophys. Res.*, *117*(B2), n/a–n/a.

Hu, J., Li, Z. W., Ding, X. L., Zhu, J. J., Zhang, L., & Sun, Q. (2012). 3d coseismic displacement of 2010 darfield, new zealand earthquake estimated from multi-aperture insar and d-insar measurements. *Journal of Geodesy*, *86*(11), 1029-1041.

Jakowatz, C. V., Wahl, D., Eichel, P., Ghiglia, D., & Thompson, P. (1996). *Synthetic aperture radar: A proc. app.* Boston, MA: Kluwer.

Jónsson, S. (2012). Tensile rock mass strength estimated using insar. *Geophys. Res. Lett.*, *39*(21).

Jónsson, S., Zebker, H., Segall, P., & Amelung, F. (2002). Fault slip distribution of the 1999 mw 7.1 hector mine, california, earthquake, estimated from satellite radar and gps measurements. *Bulletin of the Seismological Society of America*, *92*(4), 1377–1389.

Joughin, I. R., Winebrenner, D. P., & Fahnestock, M. A. (1995). Observations of ice-sheet motion in greenland using satellite radar interferometry. *Geophys. Res. Lett.*, *22*(5), 571–574.

Jung, H., Lu, Z., Won, J., Poland, M., & Miklius, A. (2011). Mapping three-dimensional surface deformation by combining multiple-aperture interferometry and conventional interferometry: Application to the june 2007 eruption of kilauea volcano, hawaii. *Geoscience and Remote Sensing Letters, IEEE*, *8*(1), 34 -38.

Jung, H., Lu, Z., & Zhang, L. (2013). Feasibility of along-track displacement measurement from sentinel-1 interferometric wide-swath mode. *IEEE Trans. Geosci. Remote Sens.*.

Jung, H., Won, J.-S., & Kim, S.-W. (2009). An improvement of the performance of multiple-aperture sar interferometry (mai). *IEEE Trans. on Geosci. Remote Sensing*, *47*(8), 2859 -2869.

Kampes, B., & Usai, S. (1999). Doris: The delft object-oriented radar interferometric software. In *2nd international symposium on operationalization of remote sensing, enschede, the netherlands* (Vol. 16, p. 20).

Kong, Y.-K., Cho, B.-L., & Kim, Y.-S. (2005, April). Ambiguity-free doppler centroid estimation technique for airborne sar using the radon transform. *Geoscience and Remote Sensing, IEEE Transactions on*, *43*(4), 715-721.

Kositsky, A. P., & Avouac, J. P. (2010). Inverting geodetic time series with a principal component analysis-based inversion method. *J. Geophys. Res.*, *115*, B03401.

Krieger, G., Moreira, A., Fiedler, H., Hajnsek, I., Werner, M., Younis, M., & Zink, M. (2007). Tandem-x: A satellite formation for high-resolution sar interferometry. *IEEE Trans. on Geosci. Remote Sensing*, *45*(11), 3317–3341.

Lanari, R., Casu, F., Manzo, M., Zeni, G., Berardino, P., Manunta, M., & Pepe, A. (2007). An overview of the small baseline subset algorithm: A dinsar technique for surface deformation analysis. *Pure and Applied Geophysics*, *164*(4), 637–661.

Larson, K. M., Poland, M., & Miklius, A. (2010). Volcano monitoring using gps: Developing data analysis strategies based on the june 2007 kilauea volcano intrusion and eruption. *Journal of Geophysical Research: Solid Earth (1978–2012)*, *115*(B7).

Li, Z., & Bethel, J. (2008). Image coregistration in sar interferometry. *Proc. Int. Arch. Photogramm., Remote Sens. Spatial Inf. Sci*, 433–438.

Lin, Y. N., Kositsky, A. P., & Avouac, J. P. (2010). Pcaim joint inversion of insar and ground-based geodetic time series: Application to monitoring magmatic inflation beneath the long valley caldera. *Geophys. Res. Lett.*, *37*, L23301.

López, J. L., & Temme, N. M. (1999). Approximations of orthogonal polynomials in terms of hermite polynomials. *Methods and Applications of Analysis*, *6*, 131–146.

Lu, L., Liao, M., & Wang, T. (2005). Registration of insar complex images based on integrating correlation- registration and least square-registration. In *Proc. spie* (Vol. 6043).

Madsen, S. N. (1989). Estimating the doppler centroid of sar data. *Aerospace and*

*Electronic Systems, IEEE Transactions on*, *25*(2), 134–140.

Massonnet, D., Briole, P., & Arnaud, A. (1995). Deflation of mount etna monitored by spaceborne radar interferometry. *Nature*, *375*(6532), 567–570.

Massonnet, D., Rossi, M., Carmona, C., Adragna, F., Peltzer, G., Feigl, K., & Rabaute, T. (1993). The displacement field of the landers earthquake mapped by radar interferometry. *Nature*, *364*(6433), 138–142.

McMillan, M., Shepherd, A., Gourmelen, N., Park, J., Nienow, P., Rinne, E., & Leeson, A. (2012). Mapping ice-shelf flow with interferometric synthetic aperture radar stacking. *Journal of Glaciology*, *58*(208), 265-277.

McNairn, H., Shang, J., Jiao, X., & Champagne, C. (2009). The contribution of alos palsar multipolarization and polarimetric data to crop classification. *Geoscience and Remote Sensing, IEEE Transactions on*, *47*(12), 3981–3992.

Meier, E., Graf, C., & Nuesch, D. (1989). Generation of geocoded spaceborne sar image products. In *Geoscience and remote sensing symposium, 1989. igarss'89. 12th canadian symposium on remote sensing., 1989 international* (Vol. 4, pp. 2473–2477).

Mogi, K. (1958). Relations between the eruptions of various volcanoes and the deformations of the ground surfaces around them. *Bulletin of the Earthquake Research Institute of the University of Tokyo*.

Moller, D., Chu, A., Lou, Y., Miller, T., & O'Leary, E. (2001). Pacrim ii: A review of airsar operations and system performance. In *Geoscience and remote sensing symposium, 2001. igarss'01. ieee 2001 international* (Vol. 3, pp. 1389–1391).

Murray, J., Segall, P., Cervelli, P., Prescott, W., & Svarc, J. (2001). Inversion of gps data for spatially variable slip-rate on the san andreas fault near parkfield, ca. *Geophysical research letters*, *28*(2), 359–362.

Ng, A. H.-M., Ge, L., Zhang, K., Chang, H.-C., Li, X., Rizos, C., & Omura, M. (2011). Deformation mapping in three dimensions for underground mining using insar–southern highland coalfield in new south wales, australia. *International Journal of Remote Sensing*, *32*(22), 7227–7256.

Ng, A. H.-M., Ge, L., Zhang, K., & Li, X. (2012). Estimating horizontal and vertical movements due to underground mining using alos palsar. *Engineering Geology*,

*143144*(0), 18 - 27.

Nitti, D. O., Hanssen, R. F., Refice, A., Bovenga, F., & Nutricato, R. (2011). Impact of dem-assisted coregistration on high-resolution sar interferometry. *Geoscience and Remote Sensing, IEEE Transactions on*, *49*(3), 1127–1143.

Peltzer, G., Crampé, F., Hensley, S., & Rosen, P. (2001). Transient strain accumulation and fault interaction in the eastern california shear zone. *Geology*, *29*(11), 975–978.

Pepe, A., Sansosti, E., Berardino, P., & Lanari, R. (2005). On the generation of ers/envisat dinsar time-series via the sbas technique. *Geoscience and Remote Sensing Letters, IEEE*, *2*(3), 265 - 269.

Poland, M., Miklius, A., Orr, T., Sutton, J., Thornber, C., & Wilson, D. (2008). New episodes of volcanism at kilauea volcano, hawaii. *Eos, Transactions American Geophysical Union*, *89*(5), 37–38.

Pottier, E., & Ferro-Famil, L. (2008). Advances in sar polarimetry applications exploiting polarimetric spaceborne sensors. In *Radar conference, 2008. radar'08. ieee* (pp. 1–6).

Prati, C., Ferretti, A., & Perissin, D. (2010). Recent advances on surface ground deformation measurement by means of repeated space-borne sar observations. *Journal of Geodynamics*, *49*(3), 161–170.

Prati, C., & Rocca, F. (1993). Improving slant-range resolution with multiple sar surveys. *Aerospace and Electronic Systems, IEEE Transactions on*, *29*(1), 135 -143.

Reeves, J. A., Knight, R., Zebker, H. A., Schreüder, W. A., Agram, P. S., & Lauknes, T. R. (2011). High quality insar data linked to seasonal change in hydraulic head for an agricultural area in the san luis valley, colorado. *Water Resources Research*, *47*, Art–No.

Reigber, A. (1999). Range dependent spectral filtering to minimize the baseline decorrelation in airborne sar interferometry. In *Proc. ieee igarss'99* (Vol. 3, p. 1721 -1723 vol.3).

Rodriguez, E., & Martin, J. (1992). Theory and design of interferometric synthetic aperture radars. *Radar and Signal Processing, IEE Proceedings F*, *139*(2), 147

-159.

Rosen, P. A., Hensley, S., Peltzer, G., & Simons, M. (2004). Updated repeat orbit interferometry package released. *Eos, Transactions American Geophysical Union*, *85*(5), 47–47.

Rott, H. (2009). Advances in interferometric synthetic aperture radar (insar) in earth system science. *Progress in Physical Geography*, *33*(6), 769–791.

Rufino, G., Moccia, A., & Esposito, S. (1998). Dem generation by means of ers tandem data. *IEEE Trans. on Geosci. Remote Sensing*, *36*(6), 1905–1912.

Sandwell, D. T., Mellors, R., Tong, X., Wei, M., & Wessel, P. (2011). Gmtsar: An insar processing system based on generic mapping tools.

Sandwell, D. T., Myer, D., Mellors, R., Shimada, M., Brooks, B., & Foster, J. (2008). Accuracy and resolution of alos interferometry: Vector deformation maps of the father's day intrusion at kilauea. *IEEE Trans. Geosci. Remote Sens.*, *46*(11), 3524 -3534.

Sandwell, D. T., & Price, E. (1998). Phase gradient approach to stacking interferograms. *Journal of Geophysical Research*, *103*, 30–30.

Sandwell, D. T., Sichoix, L., & Smith, B. (2002). The 1999 hector mine earthquake, southern california: Vector near-field displacements from ers insar. *Bulletin of the Seismological Society of America*, *92*(4), 1341–1354.

Sansosti, E., Berardino, P., Manunta, M., Serafino, F., & Fornaro, G. (2006). Geometrical sar image registration. *IEEE Trans. on Geosci. Remote Sensing*, *44*(10), 2861–2870.

Scharroo, R., & Visser, P. (1998). Precise orbit determination and gravity field improvement for the ers satellites. *Journal of Geophysical Research: Oceans (1978–2012)*, *103*(C4), 8113–8127.

Schreier, G., Kosmann, D., & Roth, A. (1990). Design aspects and implementation of a system for geocoding satellite sar-images. *ISPRS Journal of Photogrammetry and Remote Sensing*, *45*(1), 1–16.

Schubert, A., Jehle, M., Small, D., & Meier, E. (2010). Influence of atmospheric path delay on the absolute geolocation accuracy of terrasar-x high-resolution

products. *Geoscience and Remote Sensing, IEEE Transactions on*, *48*(2), 751–758.

Schwabisch, M., & Geudtner, D. (1995). Improvement of phase and coherence map quality using azimuth prefiltering: examples from ers-1 and x-sar. In *Proc. ieee igarss'95* (Vol. 1, p. 205 -207 vol.1).

Schwerdt, M., Hounam, D., Alvarez-Pères, J.-L., & Molkenthin, T. (2005). The calibration concept of terrasar-x: a multiple-mode, high-resolution sar. *Canadian Journal of Remote Sensing*, *31*(1), 30–36.

Segall, P. (2010). *Earth and volcano defomation*. Princeton, N.J.: Princeton University Press.

Skolnik, M. I. (1990). Radar handbook. *McGraw-Hill Book Co*.

Soumekh, M. (1999). *Synthetic aperture radar signal processing*. New York: Wiley New York.

Stacy, N. (1997). Synthetic aperture radar out of slant plane motion compensation. In *Proc. ieee igarss'97* (Vol. 2, p. 728 -730 vol.2).

Stevens, D., Cumming, I., & Gray, A. (1995). Options for airborne interferometric sar motion compensation. *IEEE Trans. Geosci. Remote Sens.*, *33*(2), 409 -420.

Sudhaus, H., & Jónsson, S. (2009). Improved source modelling through combined use of insar and gps under consideration of correlated data errors: application to the june 2000 kleifarvatn earthquake, iceland. *Geophysical Journal International*, *176*(2), 389–404.

Sun, J., Shen, Z., Xu, X., & Brgmann, R. (2004). Synthetic normal faulting of the 9 january 2008 nima (tibet) earthquake from conventional and along-track sar interferometry. *Geophys. Res. Lett.*, *35*, L22308.

Tapley, B. D., Ries, J., Davis, G., Eanes, R., Schutz, B., Shum, C., ... Putney, B. (1994). Precision orbit determination for topex/poseidon. *Journal of Geophysical Research: Oceans (1978–2012)*, *99*(C12), 24383–24404.

Tizzani, P., Berardino, P., Casu, F., Euillades, P., Manzo, M., Ricciardi, G., ... Lanari, R. (2007). Surface deformation of long valley caldera and mono basin, california, investigated with the sbas-insar approach. *Remote Sensing of Environment*, *108*(3), 277 - 289.

Ulander, L., & Frolind, P.-O. (1998). Ultra-wideband sar interferometry. *IEEE Trans. Geosci. Remote Sens.*, *36*(5), 1540 -1550.

Wan, Z., Shao, Y., Xie, C., & Zhang, F. (2010). Ortho-rectification of high-resolution sar image in mountain area by dem. In *Geoinformatics, 2010 18th international conference on* (pp. 1–6).

Weber, H. E., & Zebker, H. A. (2000). Penetration depths inferred from interferometric volume decorrelation observed over the greenland ice sheet. *IEEE Trans. on Geosci. Remote Sensing*, *38*(6), 2571–2583.

Werner, C., Wegmüller, U., Strozzi, T., & Wiesmann, A. (2000). Gamma sar and interferometric processing software. In *Proceedings of the ers-envisat symposium, gothenburg, sweden* (pp. 16–20).

Wright, T. J., Myer, D., Parsons, B. E., & Lu, Z. (2004). Toward mapping surface deformation in three dimensions using insar. *Geophys. Res. Lett.*, *31*(1), L01607.

Yamamoto, V. S. K. V. Y. (2008). Technology of precise orbit determination. *Fujitsu Sci. Tech. J*, *44*(4), 401–409.

Zebker, H. A., & Goldstein, R. M. (1986). Topographic mapping from interferometric synthetic aperture radar observations. *J. Geophys. Res*, *91*(B5), 4993–4999.

Zebker, H. A., Hensley, S., Shanker, P., & Wortham, C. (2010). Geodetically accurate insar data processor. *IEEE Trans. Geosci. Remote Sens.*, *48*(12), 4309 -4321.

Zebker, H. A., & Rosen, P. (1994). On the derivation of coseismic displacement fields using differential radar interferometry: The landers earthquake. In *Geoscience and remote sensing symposium, 1994. igarss'94. surface and atmospheric remote sensing: Technologies, data analysis and interpretation., international* (Vol. 1, pp. 286–288).

Zebker, H. A., Rosen, P. A., Goldstein, R. M., Gabriel, A., & Werner, C. L. (1994). On the derivation of coseismic displacement fields using differential radar interferometry: The landers earthquake. *J. Geophys. Res.*, *99*(B10), 19617–19634.

Zebker, H. A., & Villasenor, J. (1992). Decorrelation in interferometric radar echoes. *IEEE Trans. on Geosci. Remote Sensing*, *30*(5), 950 -959.

Zhao, C., Lu, Z., & Zhang, Q. (2013). Time-series deformation monitoring over

mining regions with sar intensity-based offset measurements. *Remote Sensing Letters*, *4*(5), 436–445.

Zisk, S. (1972). Lunar topography- first radar-interferometer measurements of the alphonsus-ptolemaeus-arzachel region. *Science*, *178*(4064), 977.